Topological Properties of Some Quantum Systems

A thesis submitted to the Jadavpur University
for the degree of Doctor of Philosophy

in Science

2025

by

Arghya Sil

Department of Physics
Jadavpur University

যাদবপুর বিশ্ববিদ্যালয়
কলকাতা - ৭০০ ০৩২, ভারত

Jadavpur University
Kolkata – 700 032, India

CERTIFICATE FROM THE SUPERVISOR

This is to certify that the thesis entitled "Topological Properties of some Quantum Systems" submitted by Mr. Arghya Sil, who got his name registered on 14/11/2019 for the award of Ph.D. (Science) degree of Jadavpur University, is absolutely based upon his own work under the supervision of Prof. Asim Kumar Ghosh and that neither this thesis nor any part of it has been submitted for either any degree/diploma or any other academic award anywhere before.

Dr. Asim Kumar Ghosh
Professor
Department of Physics
Jadavpur University

Asimkumar Ghosh
24/02/2025

Dr. Asim Kumar Ghosh
Professor
Department of Physics
Jadavpur University

STATEMENT OF ORIGINALITY

I, Arghya Sil, registered on 14 / 11 / 2019, do hereby declare that this thesis entitled "Topological Properties of some Quantum Systems" contains literature survey and original research work done by the undersigned candidate as part of his Doctoral studies. All information in this thesis have been obtained and presented in accordance with existing academic rules and ethical conduct. I declare that, as required by these rules and conduct, I have fully cited and referred all materials and results that are not original to this work. Also, it has not been submitted for any degree or examination in any other university. I further declare that all the resources I have used or quoted have been indicated and acknowledged by complete references.

Arghya Sil
24/02/2025

Mr. Arghya Sil

(The Doctoral Candidate)

Dedication

This thesis is dedicated to my parents and my wife.

Acknowledgment

I am grateful to my supervisor Professor Asim Kumar Ghosh, Department of Physics, Jadavpur University for his supervision throughout my research work. This thesis would not be possible without his constant support and guidance. His enthusiasm and deep insight into physical problems are the sources of inspiration during this period. Apart from Physics, we had long discussions on variety of topics under the sun which enriched me a lot.

I would like to thank the Department of Physics, Jadavpur University for providing me wonderful infrastructure and work environment. I am also thankful to the faculty members of the department.

I am also thankful to my lab mates Dr. Moumita Deb, Dr. Susobhan Paul, Mr. Prasun Das and Rakesh Kumar Malakar. Finally, I am deeply indebted to my parents and my wife for their unconditional love, support and, encouragement.

List of Published Papers

1. Nontrivial topological phases on the stuffed honeycomb lattice;
   Arghya Sil and Asim Kumar Ghosh,
   J. Phys.: Condens. Matter **32** 025601 (2019).

2. Emergence of photo-induced multiple topological phases on square-octagon lattice;
   Arghya Sil and Asim Kumar Ghosh,
   J. Phys.: Condens. Matter **31** 245601 (2019).

3. First and second order topological phases on ferromagnetic breathing kagome lattice;
   Arghya Sil and Asim Kumar Ghosh,
   J. Phys.: Condens. Matter **32** 205601 (2020).

4. Topological phases of monolayer and bilayer depleted Lieb lattices;
   Arghya Sil and Asim Kumar Ghosh,
   J. Phys.: Condens. Matter **36** 125401 (2024).

Contents

Chapter 1

Introduction

1.1 Topology and Condensed Matter Physics

Topological states of matter, especially the topological insulators (TI) and its variants have been one of the principal areas of attraction among the condensed matter physicists in the twenty-first century. The story started with the discovery of integer quantum Hall effect (IQHE) [1], took a turn with the exposition of Haldane model [2] followed by its experimental realization [3]. The intriguing journey continues through the manifestation of quantum spin Hall effect (QSHE) [4], fractional quantum Hall effect (FQHE) [5], higher order topological insulators (HOTI) [6] and various other additions to the large family of TIs.

Mathematically, topology is a geometric property that is invariant under any continuous deformation. The objects are classified by the value of genus, which is basically the number of holes in the object. For example, the surfaces of a coffee cup and a doughnut are considered equivalent in topology since both have equal number of holes. In other words, coffee cup can be converted into a doughnut with continuous deformation, like stretching, twisting, bending etc. This leads to the idea of a topological invariant which remains same as the

object is continuously deformed and changes when there is a topological phase transition (TPT).

Similarly, in condensed matter physics, there are systems which are robust under continuous deformation and can be associated with a definite topological invariant. Here the system is described by its Hamiltonian and deformation of the system is accomplished by changing the values of the parameters in the Hamiltonian. Generally, these systems are bulk insulators [7], known as TI, but these can be metals [8] and superconductors [9] also. For insulators, the electronic band structure consists of a direct or indirect gap between the conduction and valence bands. Robustness ensures that the topological invariant remains unchanged in continuous deformation of the Hamiltonian without closing the gap. Whenever the gap is closed, TPT occurs and the system undergoes transition to a new topological phase with a different value of topological invariant. The behaviour of the bulk topological invariants governs the nature of the gapless surface states. In case of topological metals, the topology is manifested through the existence of exotic surface states or Fermi arcs, whereas topological superconductors show the emergence of Majorana quasi-particles.

Topology is closely associated with symmetry breaking. Based on the three principal symmetries namely charge conjugation, parity and time-reversal, TIs are classified into ten classes [10]. Throughout our work, we have focused especially on the class A, namely the Chern insulators (CIs). In this case, the topological invariant is termed as the Chern number. Through our effort, we have tried to find out the mysterious link between the Hamiltonian and the Chern number, by formulating fermionic and bosonic models on various two-dimensional (2D) lattice systems. Before jumping onto that, we are going to delve into the brief history of TIs, especially the Chern insulators.

1.2 Hall Effect and Discovery of Topological Insulator

In 1879, Hall discovered that charge carriers are deflected and accumulated near the boundary of a conducting material placed in an external electric and magnetic field normal to each other [11]. This gives rise to Hall voltage, measurement of which identifies the sign of charge carriers. This is known as Hall effect. In 1980, the IQHE was discovered by Von Klitzing [1]. In a Si/SiO_2 field effect transistor, if the two-dimensional electron gas (inversion layer) is subjected to a strong magnetic field, the longitudinal conductance vanishes and the Hall conductance, σ becomes quantized in the units of e^2/h. The magnetic field splits the energy levels of electrons into Landau levels and the filling factor of these discrete Landau levels determine the quantization. While the bulk electrons remain localized, the electrons near the edge form chiral edge channels. The application of IQHE was limited because of the necessity of strong magnetic fields.

To describe this quantization of Hall conductivity, in 1982, Thouless et. al. [12] investigated the phenomena by adding uniform magnetic field and a periodic potential to the IQHE system of 2D electron gas. Whenever the Fermi energy lies in a band-gap, the Hall conductivity gets quantized. Starting from the Kubo formula of Hall conductivity, they proved that the quantum number cannot get changed until the band-gap closes. Thus, the Thouless-Kohmoto-Nightingale-den Nijs (TKNN) formula (Eq. (1.16)) proves that the Hall conductivity indeed is the topological invariant of the system.

In 1988, Haldane [2] discovered quantum anomalous Hall effect (QAHE), which eventually paved the way for experimental realization of TIs. He considered a 2D honeycomb lattice structure of graphene and formulated a tight-

binding Hamiltonian of spinless fermions on this lattice system. The Hamiltonian was constituted such that each of the time-reversal, particle-hole and chiral symmetries were broken. Most crucially, a magnetic flux was added in such a way that net magnetic flux through each unit cell was zero. He established that the QHE phases are indeed quantized in the units of ± 1 which originates from the electronic band structure instead of the discrete Landau levels since the net magnetic field is zero. This is termed as QAHE. The topological invariant is termed as "Chern number", which will be described later. Subsequently it was shown that the spin-orbit coupling (SOC) can play the role of periodic magnetic flux in generating topological nontriviality, which made the experimental realization of QAHE possible [13].

In 2005, Kane and Mele proposed QSHE [4]. They considered a system of spin-1/2 electrons on honeycomb lattice with strong SOC. As a result, the model consists of two pairs of QAHE, one for spin-up electrons and other for spin-down electrons with opposite chirality. Overall, the model has spin-Hall conductance but no charge Hall conductance since both the spins cancel out. The contributions of spin-up and spin-down electrons $\sigma^{\uparrow}$ and $\sigma^{\downarrow}$ will be opposite and equal. Hence the total Hall conductance, $\sigma = \sigma^{\uparrow} + \sigma^{\downarrow} = 0$. In this case, spin-hall conductivity is defined as $\sigma_{spin} = \hbar/2e(\sigma^{\uparrow} - \sigma^{\downarrow})$, which may assume the values $(0, 1)$ whenever the chemical potential lies within the energy gap between the two degenerate pairs of bands. The electrons form a pair of helical edge states with different spins moving in opposite directions. The system does not break time-reversal symmetry and the topological invariant is called Z_2 index. Since SOC in graphene is very small, experimental realization was not possible.

In 2006, Bernevig, Hughes and Zhang proposed QSHE in HgTe/CdTe semiconductor quantum wells [7]. Varying the thickness of the quantum well, electronic band inversion occurs and simultaneously TPT occurs between an in-

sulating phase and a QSHE phase. This can be termed as the first 2D TI with insulating bulk state and conducting surface state. In the following year, same system was realized experimentally by Konig et. al [14]. Later, three-dimensional (3D) TI was predicted by the Fu-Kane model [15] and observed in $Bi_{1-x}Sb_x$ [16]. In these 3D TIs, the edge states are protected in all the three directions. However, the concept of 2D TI cannot be generalized to 3D manifold but the Chern number can be defined in some certain 2D planes of 3D Brillouin zone (BZ), containing time reversal invariant momentum (TRIM) points.

1.3 Chern Insulator (CI)

Since our work is mainly focused on Chern insulators, we want to emphasize on the properties of CIs in this section. In these insulators, each energy band is characterized by integer Chern numbers. At least, two of the bands carry non-zero Chern number and the sum of Chern numbers over all the bands is zero. Whenever, the energy bands overlap, the Chern number of those energy bands become undefined. As per ten-fold symmetry classification of TIs [10], these belong to class A, where all the three symmetries are broken. The TPT occurs through gap-closing and gap-reopening so that the Chern number makes transition between two different integer values. The TPT can be induced by changing the parameters of the Hamiltonian. If a strip geometry of the system is obtained by reducing one of the dimensions, edge states appear which connect the insulating bulk bands. It follows the bulk-boundary correspondence rule [17, 18, 19] which states that the number of edge states in an energy gap is equal to the summation of Chern numbers of the bands below that gap. Besides graphene, CI phase has been theoretically observed in various 2D lattices, e.g α-$\mathcal{T}_3$ [20], dice [21, 22], Lieb [23], kagome [24, 25], stuffed honeycomb [26], bilayer

honeycomb [27], checkerboard [28], star [29, 30], square-octagon [31, 24] lattices etc. CI phases are sometimes associated with Chern semi-metallic (CSM) phases, where indirect gap exists between the bulk bands.

1.4 Bulk-boundary Correspondence

The principle of bulk-boundary correspondence (BBC) was established mathematically by Kellendonk, Richter, and Schulz-Baldes [32, 17, 18]. Later, mathematical proof for bulk-boundary correspondence for all ten-fold symmetry classes was established. According to this theory, the characteristics of the edge states or surface states in open geometry are essentially guided by the bulk topological invariant. In case of IQHE or CI, as stated before, the Chern number N suggests the presence of N pairs of chiral edge states, while in case of spin or mirror chern number N, it ensures the emergence of $2N$ pairs of chiral edge states. For the systems where time-reversal symmetry is preserved, e.g. in Kane-Mele model, the edge states also appear in pairs, as each edge state must be accompanied by their time reversal symmetric partners. Anomaly in BBC can be found in some systems like HOTI [33], one-dimensional (1D) trimerized model [34] etc.

1.5 Other Members of TI Family

Besides the CIs and TRS protected TIs as described above, there have been many extensions to TI family, which are briefly summarized below:

Topological Magnon Insulator: TIs have been formulated on ferromagnetic (FM) materials considering Heisenberg model on different 2D lattices. These are termed as topological magnon insulator (TMI) [35, 36], since the quasiparticle excitation is called a magnon (boson). These materials show thermal

magnon Hall effect, in which temperature gradient transports a dissipation-less heat current. In these systems, Dzyaloshinskii-Moriya interaction (DMI) is incorporated to trigger non-zero Berry curvature or Chern number. So DMI plays the role of SOC or periodic flux in this case. This system has great potential for applications in spin-transport systems because the non-interacting topological magnons, being uncharged particles, can propagate without dissipation for a longer time than the electrons.

Topological Crystalline Insulator: Another class of topological materials are topological crystalline insulators (TCI) [37, 38] which have metallic surface states with quadratic band degeneracy on high symmetry crystal surfaces. The nontrivial topology is protected by crystalline symmetries such as mirror symmetry or rotational symmetry etc. These materials can be characterized by mirror Chern number or Wilson loop [39], depending on the specific symmetry.

Higher Order Topological Insulator: Rephrasing the usual TIs as first order TIs, HOTI have been discovered where d dimensional nth order TI shows $(d-n)$ dimensional boundary states [40, 41, 42, 43]. The $(d-1)$ dimensional boundaries generally do not conduct via gapless states. For example, in two-dimensional HOTIs, the conducting boundary states are obtained in zero dimension and those are termed as corner states. These states are characterized by different topological invariants like polarization, Z_Q Berry phase [44] etc depending on their symmetry. This concept of HOTIs can be extended to other classes also, e.g. higher order topological magnon insulator (HOTMI) etc.

Floquet Topological Insulator: Another class of topological materials have also been emerged, where nontrivial topology is induced by periodic photo-irradiations. These are known as Floquet topological insulator (FTI) [45]. The external time-periodic driving induces time-periodic modulation to the Hamiltonian and the effective Hamiltonian manifests divergent topological properties.

Effective time-independent Hamiltonian is formulated using Floquet-Bloch theory and conventional topological invariants are used to identify the topological phases. Existence of FTI phase was first predicted on graphene [46].

Fractional Chern Insulator: Recently, in some tight-binding topological models, it has been observed that flat bands are carrying non-zero Chern number [28, 47]. These are called topological flat bands which can host fractional Chern insulating phase (FCI) [48]. These systems exhibit FQHE [49] within lattice systems, arising from intricate interplays among strong electron-electron interactions, magnetic fields, and lattice potentials. These interactions lead to fractionalized excitations, featuring fractional charges and statistics. In FQHE, all the electrons are confined in the lowest Landau level, regarded as a completely flat topological band. Since this is partially filled, electron-electron interactions produce non-perturbative correlation effects. In the same way, fractional filling at a flat Chern band is investigated to generate FCI. To describe this phenomena, specific electron-electron interactions e.g, Hubbard terms are introduced onto the parent Hamiltonian describing non-interacting electrons. The energy bands become characterized by fractional Chern numbers.

Topological Superconductor: Topological Superconductors have also been predicted which host Majorana zero modes (MZM) [9, 50, 51]. By constructing Bogoliubov-de Gennes (BdG) Hamiltonian on spin-triplet superconductors, gapless chiral edge modes are found to exist. Topological phases can be characterized by the conventional topological invariants depending on the dimension and symmetries of the Hamiltonian. Majorana bound states are zero-energy quasiparticle excitations that are their own antiparticles. These states are predicted to exhibit non-Abelian braiding statistics, making them potential building blocks for fault-tolerant quantum computation.

Topological Dirac and Weyl Semimetal: Topological Dirac [52] and Weyl

semimetallic [53] phases have been investigated in which the conduction and the valence bands touch at finite number of points. However, the systems can still be characterized by different topological invariants. Within topological Dirac and Weyl semimetals, Dirac and Weyl fermions materialize as quasiparticle excitations due to specific symmetries and topology of the band structure. Dirac fermions possess linear energy dispersion, while Weyl fermions display a point-like dispersion. In Dirac and Weyl semimetals, the Dirac monopoles of different spin species occur in momentum space in separated and coincidental points respectively. Graphene is the 2D version of Dirac semimetal, Weyl semimetals are realized from 3D TI by breaking TRS or inversion symmetry. Weyl semimetal has a distinctive surface state property which is known as Fermi arc. These Dirac and Weyl semimetals showcase distinctive transport phenomena stemming from the chiral anomaly.

Topological Metal: Fascinatingly, investigation is also going on about topological metals [8], which are conducting materials with nontrivial band crossings near Fermi energy and shows edge-localized resonances. In these materials, the surface states typically manifest as metallic surface Fermi arcs or surface Dirac cones, which arise due to the non-trivial topology of the bulk electronic bands. Some topological metals host unconventional bulk fermions such as Weyl fermions or nodal lines in their bulk band structure.

1.6 Berry Phase, Chern Number and Hall Conductivity

Now, let us look into the mathematical concept connecting all the dots- topology, Chern number and Hall conductivity.

When a system is subjected to a cyclic adiabatic process, the wave-function

acquires a phase difference γ over the course of a cycle. This is known as geometric phase or Pancharatnam-Berry phase or simply Berry phase [54, 55]. We assume a system described by the Hamiltonian $H(\mathbf{R}(t))$, which depends on a set of time-dependent parameters, $\mathbf{R}(t) \equiv (\mathbf{R}_1(t), \mathbf{R}_2(t), \mathbf{R}_3(t), \cdots)$. The eigenstate of the system $|\psi_n(\mathbf{R}(t))\rangle$ follows time dependent Schrödinger's equation. Given that the variation of the Hamiltonian is adiabatic (very slow with respect to time), if the system starts out in the n-th eigenstate $|\psi_n(\mathbf{R})\rangle$, at time $t = 0$, it remains in the n-th eigenstate by picking a couple of additional phase-factors which essentially depend on the time elapsed [56]. In case the eigenstate $|\psi_n(\mathbf{R})\rangle$ is non-degenerate, it can be shown that the general solution of the Schrödinger equation leads to

$$|\Psi(t)\rangle = e^{i\gamma_n(t)} e^{-i/\hbar \int_0^t E_n(\mathbf{R}(t'))dt'} |\psi_n(\mathbf{R}(t))\rangle ,$$

where, $H(t)\,|\psi_n(t)\rangle = E_n(t)\,|\psi_n(t)\rangle$, and

$$\begin{aligned} \gamma_n(t) &= i \int_0^t \langle \psi_n(\mathbf{R}(t'))|\, \partial_{t'}\, |\psi_n(\mathbf{R}(t'))\rangle \, dt', \\ &= i \int_{\mathbf{R}(0)}^{\mathbf{R}(t)} \langle \psi_n(\mathbf{R})|\, \boldsymbol{\nabla}_{\mathbf{R}}\, |\psi_n(\mathbf{R})\rangle \cdot d\mathbf{R}. \end{aligned}$$

$\gamma_n(t)$ is called the Berry phase. This phase cannot always be eliminated by gauge transformation, so, sometimes it generates physically observable consequences. In case of a cyclic evolution around a closed path, $\mathcal{C}$, over a time period, T, such that $\mathbf{R}(T) = \mathbf{R}(0)$, the close path Berry phase is

$$\gamma_n(T) = i \oint_{\mathcal{C}} \langle \psi_n(\mathbf{R})|\, \boldsymbol{\nabla}_{\mathbf{R}}\, |\psi_n(\mathbf{R})\rangle \cdot d\mathbf{R}.$$

Let us apply this formulation on condensed matter systems described by the Bloch Hamiltonian $H(\mathbf{k})$, $\mathbf{k}$ being the momentum in the first Brillouin zone.

$H(\mathbf{k})$ is periodic in the reciprocal space. The Berry phase can be written in this case as [57]

$$\gamma_n = i \int_{k \in 1\mathrm{BZ}} \langle n(\mathbf{k}) | \boldsymbol{\nabla}_k | n(\mathbf{k}) \rangle \cdot d\mathbf{k} = \oint d\mathbf{k} \cdot \mathbf{A}(\mathbf{k}), \tag{1.1}$$

where $n(\mathbf{k})$ is the eigenstate of the system, $\mathbf{A}(\mathbf{k}) = i \langle n(\mathbf{k}) | \boldsymbol{\nabla}_k | n(\mathbf{k}) \rangle$ is known as the Berry connection, and 1BZ means first Brillouin zone.

Line integral in Eq. (1.1) has been converted into a surface integral:

$$\gamma_n = \int (\boldsymbol{\nabla}_{\mathbf{k}} \times \mathbf{A}) \cdot d^2\mathbf{k} = \int \epsilon^{ijk} (\partial_j A_k) d^2 k_i, \tag{1.2}$$

where $\partial_j \equiv \partial / \partial \mathrm{k}_j$. Simplifying further

$$\gamma_n = -\mathbf{Im} \int_S d^2 k_i \epsilon^{ijk} \langle \partial_j n(\mathbf{k}) | \partial_k n(\mathbf{k}) \rangle. \tag{1.3}$$

Now introducing the identities $1 = \sum_m |m(\mathbf{k})\rangle\langle m(\mathbf{k})|$, and

$$\langle m | \partial_{\mathbf{k}} n \rangle = \frac{\langle m | (\partial_{\mathbf{k}} H) | n \rangle}{E_n - E_m}, \tag{1.4}$$

the Berry phase can be expressed as:

$$\gamma_n = \int_{1\mathrm{BZ}} d^2\mathbf{k} \cdot \mathbf{R}_n,$$

where

$$\mathbf{R}_n = -Im \sum_{m \neq n} \frac{\langle n(\mathbf{k}) | \boldsymbol{\nabla}_k H | m(\mathbf{k}) \rangle \times \langle m(\mathbf{k}) | \boldsymbol{\nabla}_k H | n(\mathbf{k}) \rangle}{(E_n(\mathbf{k}) - E_m(\mathbf{k}))^2}.$$

For 2D systems, the Berry phase can be written as

$$\gamma_n = \int_{1\mathrm{BZ}} dk_x dk_y \Omega^n_{k_x, k_y}, \tag{1.5}$$

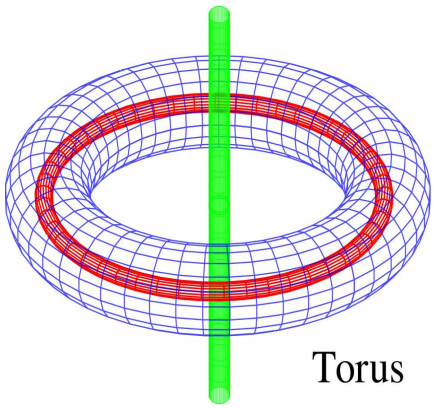

Figure 1.1: Torus (in blue) along with two embedded magnetic fluxes. The flux Φ^x is drawn in green and Φ^y in red.

where $\Omega^n_{k_x,k_y}$ is called the Berry curvature defined by

$$\Omega^n_{k_x,k_y} = -i\left[\left\langle \partial_{k_x} n(\mathbf{k}) \middle| \partial_{k_y} n(\mathbf{k}) \right\rangle - H.c.\right].$$

The Chern number of n-th energy band is defined as the total Berry curvature passing through the entire Brillouin zone for that energy band,

$$C_n = \frac{\gamma_n}{2\pi} = \frac{1}{2\pi}\int_{1\mathrm{BZ}} dk_x dk_y \Omega^n_{k_x,k_y}. \tag{1.6}$$

Now, the well-known Kubo formula for Hall conductivity is [58]

$$\sigma_H(E) = \frac{ie^2\hbar}{A_0}\sum_{\mathbf{k}}\sum_{E_m<E<E_n}\frac{\langle m|v_x|n\rangle\langle n|v_y|m\rangle - \langle m|v_y|n\rangle\langle n|v_x|m\rangle}{(E_m-E_n)^2}, \tag{1.7}$$

where v_α is the velocity operator defined by $v_\alpha = (1/i\hbar)[\alpha, H]$, where $\alpha = x, y$.

In order to relate C_n with $\sigma_H(E)$, let us consider a system of particles with charge e moving over the rectangular area $A = L_x L_y$. Under periodic boundary condition over two orthogonal directions, the surface becomes a torus. Now assume two magnetic fluxes $\Phi^\alpha, \alpha = x, y$ threaded through the x and y holes of the torus as shown in Fig. 1.1 [58, 59].

The states of the system are only sensitive to the non-integer part of $\frac{\Phi_i}{\Phi_0}$, where $\Phi_0 = 2\pi\hbar/e$ is the flux quantum. To parameterize the torus, dimensionless variables θ_i are introduced: [59]

$$\theta_i = 2\pi \frac{\Phi_i}{\Phi_0}, \quad \theta_i \in [0, 2\pi]. \tag{1.8}$$

For this system, the Berry curvature associated with the ground state $|\Psi_0\rangle$ is defined by

$$\Omega_{x,y} = -i \left[\left\langle \partial_{\theta_x} \Psi_0 \middle| \partial_{\theta_y} \Psi_0 \right\rangle - H.c. \right]. \tag{1.9}$$

The addition of fluxes generates a first order perturbation of the form:

$$H' = -\sum_{\alpha=x,y} \frac{J_\alpha \Phi_\alpha}{L_\alpha}. \tag{1.10}$$

where J is the associated electric current density. Hence,

$$\left| \frac{\partial \Psi_0}{\partial \Phi_\alpha} \right\rangle = -\frac{1}{L_\alpha} \sum_{m \neq 0} |m\rangle \frac{\langle m | J_\alpha | \Psi_0 \rangle}{E_m - E_0}. \tag{1.11}$$

So, Kubo formula for this system can be written as:

$$\begin{aligned} \sigma_{xy} &= \frac{i\hbar}{A} \sum_{m \neq \Psi_0} \frac{\langle m|J_x|\Psi_0\rangle\langle\Psi_0|J_y|m\rangle - \langle m|J_y|\Psi_0\rangle\langle\Psi_0|J_x|m\rangle}{(E_m - E_0)^2}, \\ &= i\hbar \left[\left\langle \frac{\partial \Psi_0}{\partial \Phi_x} \middle| \frac{\partial \Psi_0}{\partial \Phi_y} \right\rangle - H.c. \right], \\ &= -\frac{e^2}{\hbar} \Omega_{x,y}. \end{aligned} \tag{1.12}$$

Integrating over the torus T^2_Φ,

$$\sigma_{xy} = -\frac{e^2}{\hbar} \int_{T^2_\Phi} \frac{d^2\theta}{2\pi^2} \Omega_{x,y}. \tag{1.13}$$

Naturally, in the θ-space, Chern number is defined by the equation:

$$C = \frac{1}{2\pi} \int_{T^2_\Phi} d^2\theta \, \Omega_{x,y}. \tag{1.14}$$

As a result, Hall conductivity and Chern number are related by the equation:

$$\sigma_{xy} = -\frac{e^2}{h} C. \tag{1.15}$$

In lattice systems, it can be concluded that, when energy E falls in one of the energy gaps, the contribution to σ_H by n completely filled bands is given by

$$\sigma_H\left(E\right) = \frac{e^2}{h} \sum_{E_n < E} C_n. \tag{1.16}$$

C_n takes only integral values when the integration is performed over the first Brillouin zone. For two-dimensional and two-band system, the most generic form of Hamiltonian is $H = \mathbf{h}(\mathbf{k}) \cdot \boldsymbol{\sigma}$, where σs are the Pauli pseudospin matrices. For this case, there is a beautiful expression of the Chern number:

$$C = \frac{1}{4\pi} \int_{1\mathrm{BZ}} \hat{\mathbf{h}} \cdot \left(\frac{\partial \hat{\mathbf{h}}}{\partial k_x} \times \frac{\partial \hat{\mathbf{h}}}{\partial k_y} \right) dk_x dk_y. \tag{1.17}$$

Hence, Chern number is simply the winding number that counts the number of times the surface traced by $\hat{\mathbf{h}}$ has wrapped around the origin which is also equal to the amount of solid angle swept by $\hat{\mathbf{h}}$. But performing this $\mathbf{k}$-integral may be difficult for many complex systems. Sticlet et al. [60] showed that the integral can be converted into a sum over Dirac points or high-symmetry points.

$$C = \frac{1}{2} \sum_{\mathbf{k} \in \mathbf{D_i}} \mathrm{sgn}(\partial_{k_x} \hat{\mathbf{h}} \times \partial_{k_y} \hat{\mathbf{h}})_i \mathrm{sgn}(h_i) \tag{1.18}$$

Where D_is are the Dirac points of the Hamiltonian and i is any arbitrary axis

chosen in pseudo-spin space. Dirac points are obtained by setting $h_{j\neq i}(D_i) = 0$.

Electrical charge polarization $\boldsymbol{p}$ is another topological invariant [6, 61] which is used to characterize many topological phases in any dimensions, even for HOTIs. Polarization along the α-direction is defined as

$$p_\alpha = \frac{1}{S}\iint_{1\mathrm{BZ}} d^2\mathbf{k} A_\alpha, \tag{1.19}$$

where $A_\alpha = -i\langle n(\mathbf{k})|\partial_{k_\alpha}|n(\mathbf{k})\rangle$ is the Berry connection along the axis $\alpha = x, y, z$, and S being the area of the first Brillouin zone.

1.7 Symmetries of the Hamiltonian

To characterize the topological insulators, three symmetries are required: time-reversal symmetry (TRS), particle-hole symmetry (PHS) or charge-conjugation and chiral or sublattice symmetry (CS). A system is invariant under TRS if and only if the complex conjugate of the first quantized Hamiltonian $\mathcal{H}^*$ is equal to $\mathcal{H}$ upon a unitary transformation, U_T [10], or

$$U_T^\dagger \mathcal{H}^* U_T = +\mathcal{H}. \tag{1.20}$$

Similarly, the system is invariant under PHS if and only if $\mathcal{H}^*$ is equal to $-\mathcal{H}$ upon a unitary transformation, U_P, which means

$$U_P^\dagger \mathcal{H}^* U_P = -\mathcal{H}. \tag{1.21}$$

Now combination of the two symmetry operations leads to

$$U_C^\dagger \mathcal{H} U_C = -\mathcal{H}, \tag{1.22}$$

where $U_C = U_T U_P$ is the unitary operator for the chiral symmetry.

Now when the Hamiltoian is expressed in second quantized form in the momentum space, like

$$\mathcal{H} = \sum_{\mathbf{k}} \psi^{\dagger}_{\mathbf{k}} H(\mathbf{k}) \psi_{\mathbf{k}}, \tag{1.23}$$

the Bloch Hamiltonian $H(\mathbf{k})$ obeys the symmetry relations as

$$TH(\mathbf{k})T^{-1} = H(-\mathbf{k}) \quad \text{and} \quad PH(\mathbf{k})P^{-1} = -H(-\mathbf{k}),$$

where T, P are the corresponding operators for TRS and PHS, respectively. As a consequence, the CS corresponds to

$$CH(\mathbf{k})C^{-1} = -H(\mathbf{k}),$$

where C is the operator for CS. By definition, the TRS operator T reverses the sign of the time, t *i.e* $T : t \to -t$. The PHS operator turns particle into holes. The operator C is a product of T and P, *i.e*, $C = T \cdot P$. It means that T, P and C form a closed group of operations. It can be shown that T and P are anti-unitary while C is unitary, where $T^2 = P^2 = \pm 1$, whereas $C^2 = +1$ [10]. Based on these three symmetries, topological insulators are classified into 10 classes as shown in the following table.

The 2D Chern insulator belongs to the Class A, so the CI phase will be exhibited by the systems where all the three symmetries are absent. The 1D Su-Schreiffer-Hegger (SSH) [63] model, which is characterized by either winding number or Zak phase, can fall in either class AIII or BDI. The Kane-Mele model comes under Class AII since it is characterized by Z_2 invariant.

Except these three symmetries, inversion symmetry also plays an important role in topological manifold. The inversion symmetry or parity operator I simply

	Symmetry			Dimension (D)		
Class	T	P	C	1	2	3
A	0	0	0	0	$\mathcal{Z}$	0
AIII	0	0	1	$\mathcal{Z}$	0	$\mathcal{Z}$
AI	+1	0	0	0	0	0
BDI	+1	+1	1	$\mathcal{Z}$	0	0
D	0	+1	0	$\mathcal{Z}_2$	$\mathcal{Z}$	0
DIII	-1	+1	1	$\mathcal{Z}_2$	$\mathcal{Z}_2$	$\mathcal{Z}$
AII	-1	0	0	0	$\mathcal{Z}_2$	$\mathcal{Z}_2$
CII	-1	-1	1	$2\mathcal{Z}$	0	$\mathcal{Z}_2$
C	0	-1	0	0	$2\mathcal{Z}$	0
CI	+1	-1	1	0	0	$2\mathcal{Z}$

Table 1.1: Ten-fold symmetry class of topological insulators. Classification of the topological invariant with respect to the symmetry and dimension of the systems. Absence of any symmetry is denoted by the number '0'. The numbers '± 1' for TRS and PHS correspond to respective symmetries when $T^2 = \pm 1$ and $P^2 = \pm 1$. For CS, the number '1' corresponds to $C^2 = +1$. [10, 62]. Nonzero values of the topological invariant are given by $\mathcal{Z}$ (any integer), $\mathcal{Z}_2$ (0 or 1, or ± 1, according to convention), $2\mathcal{Z}$ (even integer).

reverses all spatial coordinates, i.e $I : (x, y, z) \rightarrow (-x, -y, -z)$. It is an unitary operator.

1.8 One-dimensional SSH model

This is a very simple yet elegant model for describing topological phase in 1D. SSH model was introduced in 1979, to demonstrate primarily the formation of low energy solitonic excitations in conducting polymers, like polyacetylene, polythiophene, etc [63]. Tight binding Hamiltonian for the SSH model reads as

$$H = -\sum_{n=1}^{N} \Big((t+\delta)[c_{An}^{\dagger} c_{Bn} + H.c.] + (t-\delta)[c_{An+1}^{\dagger} c_{Bn} + H.c.] \Big), \tag{1.24}$$

where A, B are the sublattices, $(t+\delta)$ is intra-cell or long hopping parameter and $(t-\delta)$ is inter-cell or short hopping parameter. n is the unit cell index.

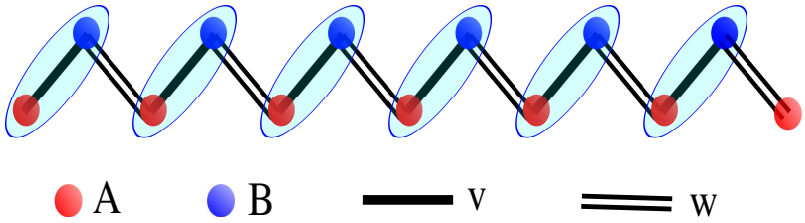

Figure 1.2: The geometry of SSH model. A, B are the two sublattices denoted by red and blue spheres respectively. Single bold line denotes the intra-cell hopping strength while the double bold line denotes the inter-cell hopping strength.

c_α ($c_\alpha^\dagger$) is the annihilation (creation) operator. After Fourier transformation, the Bloch Hamiltonian in the momentum space looks like:

$$H = \sum_k \Psi_k^\dagger (d_x \sigma_x + d_y \sigma_y) \Psi_k, \tag{1.25}$$

where $d_x = (t+\delta) + (t-\delta)\cos(k)$, $d_y = (t-\delta)\sin(k)$, and $\Psi_k^\dagger = (a_k \;\; b_k)$ is a spinor field. The spectrum has two bands separated by a energy gap $= 2\delta$ at $k = \pi$.

Topological invariant can be calculated in terms of Berry phase, which is known as Zak phase in one dimension. Using the formula

$$\gamma_n = i \int_{k \in 1\mathrm{BZ}} \langle n(\mathbf{k}) | \, \boldsymbol{\nabla}_k \, | n(\mathbf{k}) \rangle \, d\mathbf{k},$$

where $n(\mathbf{k})$ is the eigen vector.

It is found that

$$\begin{aligned} \gamma_n &= \pi, \text{ and } \nu_n = 1, \text{ if } \delta < 0, \\ \gamma_n &= 0, \text{ and } \nu_n = 0, \text{ if } \delta > 0, \\ \gamma_n &= \text{undefined, when } \delta = 0, \end{aligned}$$

where the Zak phase is related with the winding number, by the equation $\nu =$

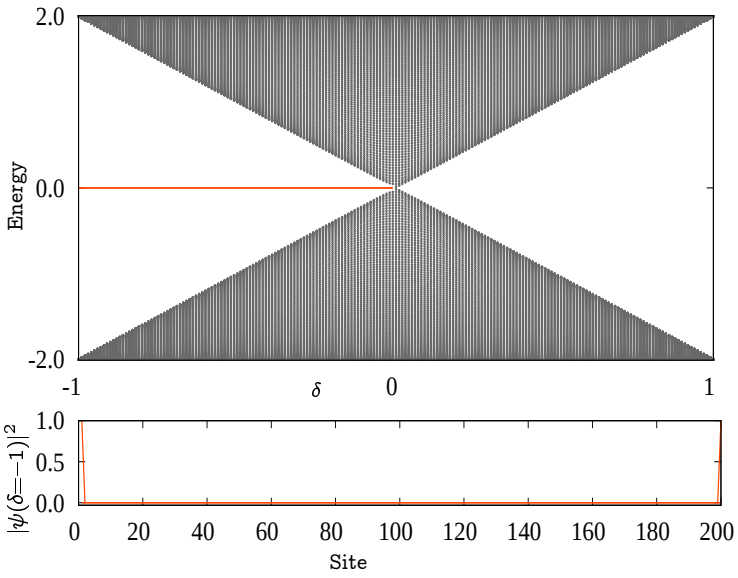

Figure 1.3: Energy spectrum of the SSH model with open boundary condition. Evidently, zero energy edge states emerge for the parameter $\delta < 0$. Lower panel shows the distribution of probability density of the edge states with respect to site number. Indeed, those states are localized at the left and right edges of the finite SSH model.

γ/π, which is valid for the models preserving the chiral symmetry. General definition of the winding number, ν is given by

$$\nu = \frac{1}{2\pi}\int_{-\pi}^{\pi}\left[\hat{\boldsymbol{d}}(\mathrm{k})\times\partial_{\mathrm{k}}\hat{\boldsymbol{d}}(\mathrm{k})\right]_z d\mathrm{k},$$

where $\hat{\boldsymbol{d}}(\mathrm{k}) = \boldsymbol{d}(\mathrm{k})/|\boldsymbol{d}(\mathrm{k})|$, and $\boldsymbol{d}(\mathrm{k}) = d_x\hat{x} + d_y\hat{y}$.

In summary, the model has topological phase for $\delta < 0$, becomes gapless or trivial for $\delta = 0$, undergoes topological phase transition and becomes gapped trivial for $\delta > 0$. The existence of zero-energy edge states in case of non-trivial topological phase can be verified simply by diagonalizing the Hamiltonian for finite number of unit cells under open boundary condition as shown in Fig. 1.3. This system has all the three symmetries, so it belongs to class BDI. As soon as the Zak phase becomes zero, the edge states decay into the bulk states. This

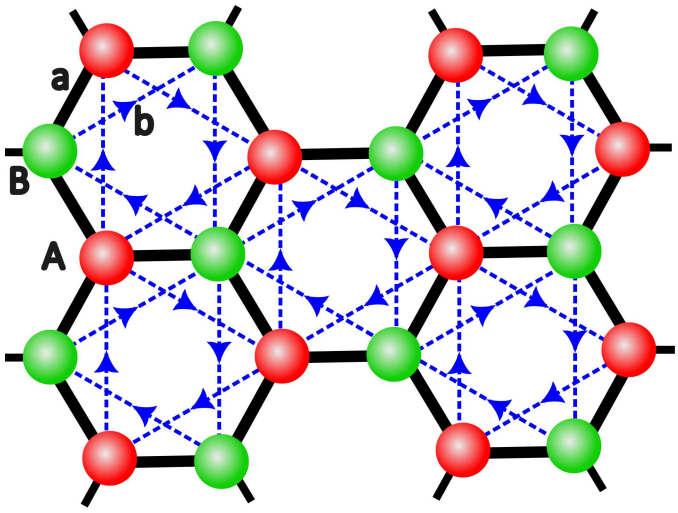

Figure 1.4: Haldane model on honeycomb lattice. A and B are the two sublattices of the honeycomb lattice, denoted by red and green spheres respectively. The solid black and dotted blue lines represent NN and NNN hopping respectively. The arrow shows the direction in which the phase ϕ is considered positive.

proves the bulk-boundary correspondence for this one-dimensional topological model. It is worth mentioning that, for 1D trimerized model [34] without inversion and chiral symmetry, this correspondence is broken since the edge modes are found along one of the edges only. When inversion and chiral symmetries are restored, edge modes are found to reappear along both the edges and the topological phase is characterized by the Zak phase.

Experimentally, the Berry phase has been measured recently by mimicking the 1D periodic potential of polyacetylene using system of ultracold atoms in optical lattices [64]. Moreover, properties of tight-binding SSH model have been experimentally validated in photonic lattice composed of helical waveguides [65].

1.9 Two-dimensional Haldane Model

In this section, we would briefly describe Haldane model [2], which laid the founding stone for further research on CI. Haldane considered a tight-binding

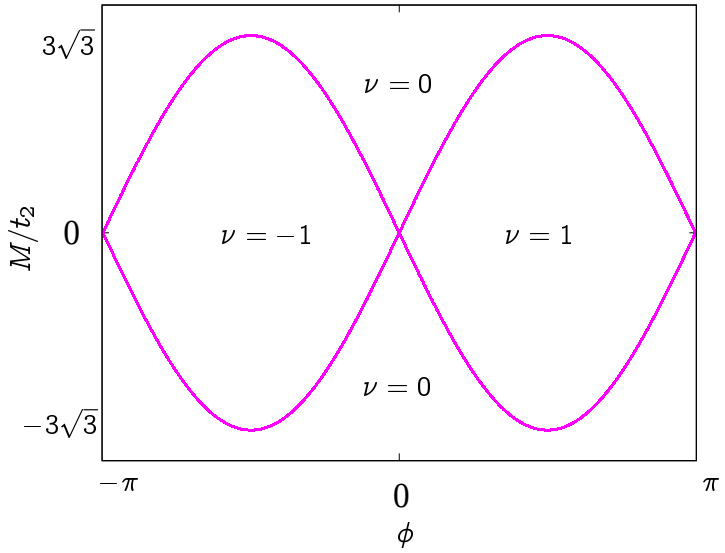

Figure 1.5: Phase diagram of the Haldane Model with $|t_2/t_1| < 1/3$ to ensure the bands do not overlap. If the sign of t_2 reverses, the sign of ν changes. The gap closes at two different Dirac points along the two different TPTs: one from $\nu = -1$ to $\nu = 0$ and another from $\nu = 1$ to $\nu = 0$.

Hamiltonian of spinless fermions on the honeycomb lattice. A and B are the two sublattices. The hopping strength between nearest neighbour (NN) sites (A-B bond) is t_1 and that between next-nearest-neighbour (NNN) sites (A-A and B-B bonds) is t_2. Presence of NNN hopping breaks the PHS. A staggered onsite energy M has been added in order to break the CS. Finally to break the TRS, a magnetic flux ϕ has been introduced. The direction of magnetic flux has been modulated through the NNN hopping parameter in such a fashion that the total flux crossing through unit cell is zero leading to no net magnetic field through the system. After Fourier transforming the real-space Hamiltonian, the momentum-space Hamiltonian can be written as:

$$H = \mathbf{h}(\mathbf{k}) \cdot \boldsymbol{\sigma}, \tag{1.26}$$

$$h_0 = 2t_2 \cos\phi \sum_{i=1}^{3} \cos(\mathbf{k} \cdot \mathbf{b_i}), h_z = M - 2t_2 \sin\phi \sum_{i=1}^{3} \sin(\mathbf{k} \cdot \mathbf{b_i})$$

$$h_x = t_1 \sum_{i=1}^{3} \cos(\mathbf{k} \cdot \mathbf{a_i}), h_y = t_1 \sum_{i=1}^{3} \sin(\mathbf{k} \cdot \mathbf{a_i})$$

where $\mathbf{b}_i$s are the NNN vectors connecting A-A or B-B sublattices defined by $\mathbf{b}_1 = \mathbf{a}_2 - \mathbf{a}_3$, $\mathbf{b}_2 = \mathbf{a}_3 - \mathbf{a}_1$, and $\mathbf{b}_3 = \mathbf{a}_1 - \mathbf{a}_2$, with $\mathbf{a}_i$s being the NN vectors connecting the A and B sites. $\mathbf{a}_1 = \frac{1}{2}a\hat{x} + \frac{\sqrt{3}}{2}a\hat{y}$, $\mathbf{a}_2 = a\hat{x}$, $\mathbf{a}_3 = \frac{1}{2}a\hat{x} - \frac{\sqrt{3}}{2}a\hat{y}$, where a is the lattice parameter. The sign of the phase ϕ is positive when considered in the clockwise direction. The h_0 term can be ignored unless there is a indirect gap-closing since this term shifts the energies of both the bands. For $t_2 = M = 0$, the Haldane model reduces to usual tight-binding model of graphene, where the gap closes at two non-equivalent Dirac points K$= (4\pi/3\sqrt{3}a, 0)$ and K$' = (-4\pi/3\sqrt{3}a, 0)$, over the Brillouin zone. When t_2 and M are incorporated, a gap opens up at the Dirac points. This plays an important role in the wrapping of $\hat{h_k}$ around Bloch sphere or the generation of non-trivial Chern numbers.

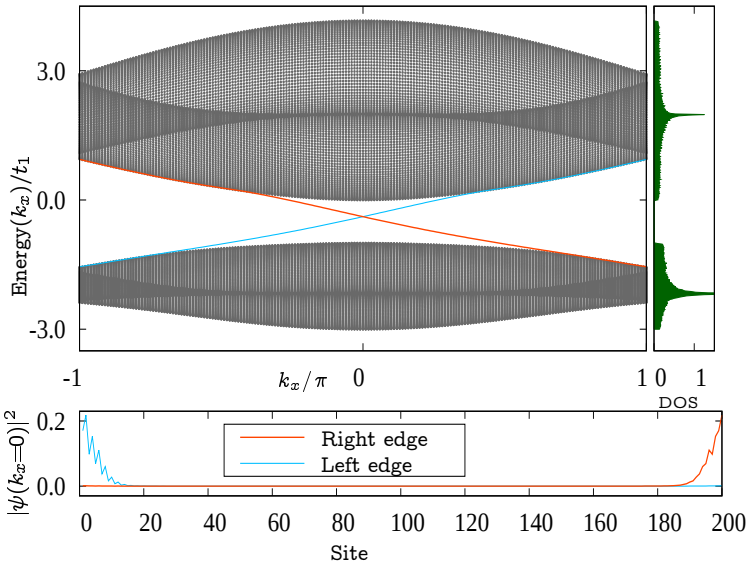

Figure 1.6: Energy spectrum of Haldane model with armchair Edge states for the parameters $t_2/t_1 = 1/3$, $M/t_1 = 1$, $\phi = \pi/3$ for $N = 200$ unit cells along y direction. The side-panel indicates the density of states (DOS). Lower panel shows the distribution of probability density of right (orange) and left (skyblue) going edge states with respect to site number of the strip for $k_x = 0$.

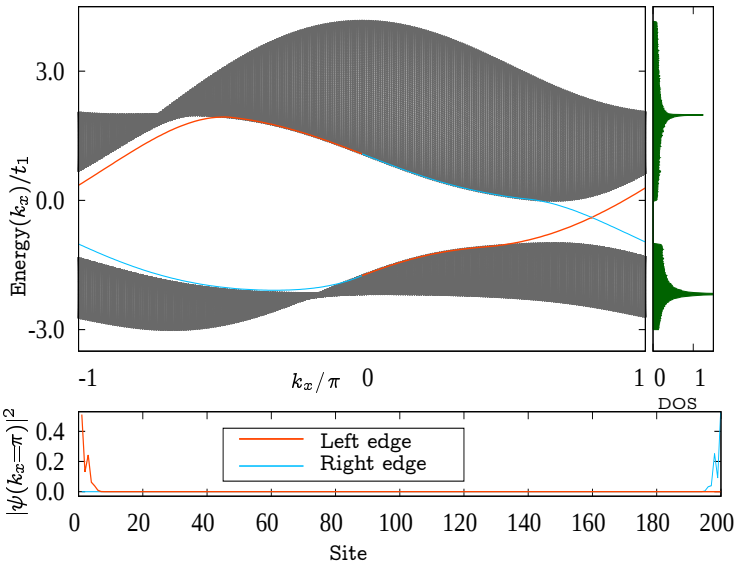

Figure 1.7: Energy spectrum of Haldane model with zigzag Edge states for the parameters $t_2/t_1 = 1/3$, $M/t_1 = 1$, $\phi = \pi/3$ for $N = 200$ unit cells along y direction in the honeycomb lattice of Fig. 1.4 rotated by 90°. The side-panel indicates the density of states. Lower panel shows the distribution of probability density of left (orange) and right (skyblue) going edge states with respect to site number of the strip for $k_x = \pi$.

Analytically, the Chern number can be computed from Eq. (1.18). It can be shown that whenever $|M/t_2| > 3\sqrt{3}|\sin\phi|$, the Chern number is zero and the system is gapped but topologically trivial. For $|M/t_2| = 3\sqrt{3}|\sin\phi|$, the two bands touch each other at the four corners of the Brillouin zone and the system becomes a trivial semimetal. For $|M/t_2| < 3\sqrt{3}|\sin\phi|$, the gap opens up, Chern number becomes ± 1, transforming the system into the topological Chern insulating phase. The TPT can be shown in a phase diagram as depicted in Fig. 1.5. Indeed, the system in the CI phase belongs to class A of the ten-fold TI class where all the symmetries are absent.

Haldane calculated the Hall conductivity σ_{xy} and from the relation Eq. (1.16), the constant term was taken to be topological invariant. When the Fermi level lies in the band-gap, the Hall conductivity σ_{xy} is quantized at temperature

$T = 0$. To calculate the value of σ_{xy}, Haldane used the thermodynamic relation,

$$\sigma_{xy} = \frac{\partial \sigma}{\partial B_0}\Big|_{\mu,T},$$

evaluated at $B_0 = 0$, where σ is the two-dimensional electric charge density and B_0 is the flux density of a uniform magnetic field along z direction.

The bulk property of this system manifests itself through exotic boundary property of surface states or edge states. Based on the direction of breaking of periodic boundary condition, honeycomb lattice produces zigzag and armchair edges. Both the edges show one pair of chiral edge states corresponding to the Chern numbers of ± 1 and obey the so-called bulk-boundary correspondence. In the Figs 1.6 and 1.7, the chiral edge states are shown and their probability densities prove that those are indeed localized along the edges, rather than in the bulk. Higher Chern numbers can be generated in this model by incorporating further neighbour hopping terms. Experimentally, G. Jotzu et. al. [3] realized the Haldane model and characterized its topological band structure using ultracold fermionic atoms in a periodically modulated optical honeycomb lattice.

1.10 Kane-Mele Model

This model was introduced by Kane and Mele [4, 66], which pioneered the realization of TI without breaking TRS. By introducing SOC between the NNN sites of honeycomb lattice, they essentially created two copies of Haldane model, each associated with a specific spin polarization. The Kane-Mele Hamiltonian

is composed of the following terms:

$$
\begin{aligned}
H_t &= -t \sum_{\langle i,j\rangle,\sigma} c_{i\sigma}^{\dagger} c_{j\sigma}, \\
H_{\mathrm{SOC}} &= i\lambda_{\mathrm{SO}} \sum_{\langle\langle i,j\rangle\rangle,\sigma} \nu_{ij} \sigma^{z} c_{i\sigma}^{\dagger} c_{j\sigma}, \\
H_{\Delta} &= \Delta \sum_{i,\sigma} \xi_i c_{i\sigma}^{\dagger} c_{i\sigma}.
\end{aligned}
\tag{1.27}
$$

Here, λ_{SO} represents the strength of the SOC, $\nu_{ij} = \pm 1$ depends on the chirality of the NNN hopping path and σ^z is the z-component of the Pauli spin matrix. The third term is the staggered sublattice potential, ($\xi_i = \pm 1$) describing the transition between the QSH phase and trivial insulator. Transforming the Hamiltonian into momentum space, a 4×4 matrix H_{KM} is obtained:

$$
H_{\mathrm{KM}} = \begin{pmatrix} H_{\uparrow} & 0 \\ 0 & H_{\downarrow} \end{pmatrix}.
$$

The spin-up (spin-down) part corresponds to the Haldane model with $\phi = \pi/2\,(-\pi/2)$. Diagonalizing the matrix, four energy bands are obtained. The competition between λ_{SO} and Δ determines the system's topological phase. If $\Delta < 3\sqrt{3}\lambda_{\mathrm{SO}}$, the system remains in the quantum spin Hall (QSH) phase, while for $\Delta > 3\sqrt{3}\lambda_{\mathrm{SO}}$, it transitions to a trivial insulating phase. The existence of QSH phase is confirmed by the presence of two pairs of non-chiral edge states in the zigzag strip geometry. The edge states are helical in nature since their motion is correlated with spin. The edge states come in pairs of degenerate states at the time-reversal invariant momentum (TRIM) in the Brillouin zone ($k_x = 0$ or $k_x = \pi$), which is the direct consequence of Kramers degeneracy occurring due to the presence of TRS.

The total Chern number of the Kane-Mele model is always zero, because

$C_\uparrow = -C_\downarrow$ and

$$C = C_\uparrow + C_\downarrow = 0.$$

Hence, spin Chern number is defined as

$$C_{spin} = (C_\uparrow - C_\downarrow)/2.$$

If Rashba coupling is incorporated in the Hamiltonian as

$$H_R = i\lambda_R \sum_{\langle i,j\rangle,\sigma,\sigma'} c^\dagger_{i\sigma}(\vec{\sigma} \times \hat{d}_{ij})^z_{\sigma\sigma'} c_{j\sigma'}, \tag{1.28}$$

then the spin-up and spin-down components are coupled together. Hence, instead of spin Chern number, topological phase is characterized by Z_2 invariant. If $u_i(\mathbf{k})$ and $u_j(\mathbf{k})$ are the two occupied Bloch wave-functions of the Hamiltonian, then the antisymmetric matrix of overlaps of time-reversed Bloch states are calculated as:

$$\langle u_i(\mathbf{k})|\Theta|u_j(\mathbf{k})\rangle = \epsilon_{ij} P(\mathbf{k}), \tag{1.29}$$

where Θ is the TRS operator defined by $i\sigma_y\kappa$, with κ being the complex conjugation operator and ϵ_{ij} is the 2D Levi-Civita symbol. $P(\mathbf{k})$ denotes the Pfaffian of this anti-symmetric matrix:

$$P(\mathbf{k}) = Pf[\langle u_i(\mathbf{k})|\Theta|u_j(\mathbf{k})\rangle]. \tag{1.30}$$

Finally, the Z_2 index is determined by evaluating the winding number of $P(\mathbf{k})$ around a loop enclosing half of the Brillouin zone,

$$Z_2 = \frac{1}{2\pi i} \oint_C d\mathbf{k} \cdot \nabla_{\mathbf{k}} \log(P(\mathbf{k}) + i\delta), \tag{1.31}$$

which is equal to the number of pairs of complex zeros of P. The value of Z_2 index is 1 for topological phase and 0 for trivial phase.

1.11 Bernevig-Hughes-Zhang Model

Bernevig-Hughes-Zhang (BHZ) [7] model solves the practical problem of experimental realization of Kane-Mele model by formulating 2D TI in HgTe/CdTe semiconductor quantum wells. By tuning the thickness of HgTe layer, TPT occurs between a trivial insulator and QSH phase. Unlike graphene, SOC is strong in this system. The momentum space Hamiltonian of the model is defined by a 4×4 matrix:

$$H(\mathbf{k}) = \begin{bmatrix} h(\mathbf{k}) & 0 \\ 0 & h^*(-\mathbf{k}) \end{bmatrix},$$

where $h(\mathbf{k})$ represents the spin-up block, and its time reversed component $h^*(-\mathbf{k})$ represents the spin-down block. The $h(\mathbf{k})$ is defined as:

$$h(\mathbf{k}) = \epsilon(\mathbf{k})I + \mathbf{d}(\mathbf{k}) \cdot \sigma,$$

where:

$$\epsilon(\mathbf{k}) = C - D(k_x^2 + k_y^2),$$
$$\mathbf{d}(\mathbf{k}) = (Ak_x, Ak_y, M - B(k_x^2 + k_y^2)).$$

Here, M is the mass term or gap parameter. This Dirac-like form of the Hamiltonian is derived from the standard $\boldsymbol{k} \cdot \boldsymbol{p}$ perturbation theory for semiconductors.

A simplified spinless tight-binding model can also be considered on a square lattice with two orbitals per site. The form of the Hamiltonian remains the

same, with the components given by:

$$\epsilon(\mathbf{k}) = C - 2D(2 - \cos k_x - \cos k_y),$$
$$\mathbf{d}(\mathbf{k}) = \Big[A \sin k_x,\ A \sin k_y,\ M - 4B + 2B(\cos k_x + \cos k_y)\Big] .$$

It reduces to the Kane-Mele model when expanded around the band inversion point $\Gamma(0,0)$. The spectrum becomes gapless at the high symmetry point Γ, for $M/2B = 0$, while it is gapless on the other high symmetry points $K(\pi, 0)$ and $M(\pi, \pi)$, respectively for $M/2B = 2$ and $M/2B = 4$. Chern number can be estimated using the well-known expression $C = \frac{1}{2}\text{sgn}[M]$ [67], which was derived analytically from the continuum model. For $M/2B < 0$, the system is in trivial insulator phase, while for $0 < M/2B < 2$, the system is in CI phase with $C = \pm 1$. The nontrivial topological phase is supported by the existence of edge states at the boundary of the finite system.

For the original block-diagonal Hamiltonian of the spinfull BHZ model, the system possesses TRS and PHS. Because of TRS, every eigen vector $|u_k\rangle$ has its degenerate Kramers partner $\Theta|u_k\rangle$. Evidently, the charge Hall conductance cancels out and spin Hall conductance remains, in a similar way as the Kane-Mele model. The modulation of quantum well thickness changes the sign of M and induces TPT.

1.12 Numerical Calculation of Chern Number

For complex systems, the integration over Berry curvature is tedious and calculation of Chern number from Eq. (1.18) also has its limitations. So, a numerical method of calculating C was developed by Fukui, Hatsugai and Suzuki [68]. The integration over Berry curvature (Ω) in Eq. (1.5) is replaced by summation of

the Ωs over discrete points of the Brillouin zone. x and y axes of the Brillouin zone have been divided into N_x and N_y segments, respectively. Each grid point corresponds to a definite plaquette denoted by k_l, where $l = 1, \cdots, N_x N_y$. So,

$$k_l = \left(\frac{2\pi j_x}{N_x}, \frac{2\pi j_y}{N_y} \right), \quad (j_\alpha = 0, \ldots, N_\alpha - 1;\ \alpha = x, y). \tag{1.32}$$

Each Bloch state varies periodically for $(j_x, j_y) = (N_x, N_y)$ along the x and y directions, respectively. Hence, any arbitrary eigen vector $|n(k_l)\rangle$ is periodic on the momentum space as, $|n(k_l + N_\alpha \mu_\alpha)\rangle = |n(k_l)\rangle$, where the vector $\boldsymbol{\mu} = \left(\frac{2\pi}{N_x}, \frac{2\pi}{N_y}\right)$.

A link variable $U_\mu(k_l)$ is defined from the wave functions of the nth band as

$$U_\alpha(k_l) \equiv \frac{\langle n(k_l) | n(k_l + \mu_\alpha) \rangle}{|\, \langle n(k_l) | n(k_l + \mu_\alpha) \rangle \,|}, \tag{1.33}$$

where $|n(k_l)\rangle$ represents the state vector for n-th band. From the link variable (Eq. (1.33)), a lattice field strength is defined by

$$\begin{aligned} F_{xy}(k_l) \;\equiv\; & \ln \left[U_x(k_l) U_y\left(k_l + \frac{2\pi}{N_x}\right) U_x\left(k_l + \frac{2\pi}{N_y}\right)^{-1} U_y(k_l)^{-1} \right], \\ & \text{with } -\pi < \frac{1}{i} F_{xy}(k_l) \leq \pi. \end{aligned} \tag{1.34}$$

The field strength is defined within the principal branch of the logarithm specified in Eq. (1.34). Evidently, this field strength is analogous to Berry Curvature. Summing the Berry curvatures over all grid points on the first Brillouin zone, Chern number for n-th band is obtained as

$$C_n \equiv \frac{1}{2\pi i} \sum_l F_{xy}(k_l). \tag{1.35}$$

The value of Chern number converges to the analytic value when the summa-

tion extends over large number of plaquettes. The algorithm works well for any shapes of Brillouin zones and for arbitrary number of bands. So, this method provides an efficient and alternative numerical route for estimating the Chern number for any lattice system and has been used extensively in numerous works.

1.13 Experimental Realizations and Applications

The material realization of QAHE, TI and QSHE have been stated before. The periodic flux in Haldane model, that mimics the effect of a magnetic field, is essentially a complex phase associated with hopping parameters in tight-binding model. This artificial gauge field has been experimentally realized [69]. It has paved the way for experimental observation of QAHE in Haldane-like models on 2D lattices. Although material discovery of all the theoretically predicted 2D CIs have not been possible, these systems can be simulated by optical lattices of ultracold atoms [70]. Thus, topological phases and TPT can be observed as the tuning of hopping amplitudes are made possible in these systems. Experimental realizations of other members of the TI family e.g, topological crystalline insulator, photonic TI, HOTI, TMI, fractional TI, topological superconductor also have been reported. In 2013, Rechtsman et. al. used ultracold atoms in a periodically driven optical honeycomb lattice to create photonic TI or Floquet TI [71]. Following the pioneering study of the magnon thermal Hall effect in the pyrochlore ferromagnet $Lu_2V_2O_7$, [72] the evidence for the gapped TMI phase was reported in the Ising-like kagome FM Cu[1,3-bdc] under applied magnetic field [73]. HOTI was first reported in 2018 where it was observed in Bismuth crystals with helical hinge states in an investigation conducted by Schindler et. al. [74].

The applications of TI include spintronic devices where SOC is used to cre-

ate spin-based electronic devices for information storage. The robust surface states are fundamental to achieve dissipationless transport in these devices. In quantum computing, TIs can be used as the edge states are protected against local perturbations and can be utilized for robust qubit operations, fault-tolerant quantum gates etc. The exotic Majorana bound states of topological superconductors are used in quantum information processing.

TIs are also utilized in opto-electronic devices, spin-transport devices and magnetic devices. TRS invariant TIs have been extensively used in photodetectors to increase the light absorbing ability. The protection of the surface state by TRS prevents scattering from non-magnetic impurities. Application of topological materials have been extended to topological field effect transistors [75] and topological P-N junctions [76]. The high surface mobility, robust surface states and narrow bandgap of TIs enable to design FET with high performance and low power consumption. By leveraging the robust surface states, spin-momentum locking, and strong nonlinear responses of TIs, lasers can be developed having lower thresholds, enhanced polarization control, stable mode-locking, and robust performance.

1.14 Motivation of our work and Outline of the Thesis

We have focused mainly on the 2D CI phase in electronic and magnonic system throughout our work. This CI phase belongs to class A of the TI classification and lacks TRS, PHS and CS. Our motivation is to find new systems that would support this CI phase. However the systems without having those symmetries do not guarantee the presence of CI phase. Hence, there have been numerous works in search of this novel phase in many 2D lattice systems by perturbing the

Hamiltonian with all the known sources of asymmetry, e.g, artificial gauge-field, spin-orbit coupling, periodic irradiation of light, electronic interaction, DMI in bosonic systems and so on. Many systems have been shown to host the phase, while others have not.

In order to frame multi-band systems with single atomic orbital, topological models are generally formulated on the non-Bravais lattices. From the structural point of view, those lattices can be divided into two different groups. Based on their origin, all those 2D lattices are derived eventually from either square or triangular lattices which are Bravais. For examples, Lieb [23], CaVO [77, 78], square-octagon [31, 24] and checkerboard [28] lattices belong to first group as they are derived from square lattice either by depleting lattice sites or introducing nonsymmetric hopping terms in the Hamiltonian. However, their reciprocal lattice is always a square lattice. More precisely, Lieb, CaVO and square-octagon lattices are nothing but depleted square lattice, where 25% of sites are removed from the square lattice in a regular manner for the Lieb lattice. For both CaVO and square-octagon lattices, 20% of the sites are removed. On the other hand, checkerboard lattice is nothing but (undepleted) square lattice where tight-binding Hamiltonian is formulated by invoking nonsymmetric hopping terms. Topological phase can also be observed on Bravais lattices considering more than one orbitals on each lattice point, e.g, multi-orbital square or triangular lattice [5]. Finally, symmetry of the resulting Hamiltonian depends on the nature of depletion and arrangement of hopping paths.

In the same way, honeycomb [2], stuffed-honeycomb [26], kagome [24, 25], breathing kagome [61], star [29, 30], α-$\mathcal{T}_3$ [20] and dice [21, 79] lattices constitute the second group as they are derived from the triangular lattice. So their reciprocal lattice is also triangular. In this group, honeycomb, kagome, breathing kagome and star lattices are depleted triangular lattice while stuffed-honeycomb,

α-$\mathcal{T}_3$ and dice lattices are essentially triangular lattice with nonsymmetric hopping bonds. Both of them are tripartite also. Our investigation drives along this path across six such 2D non-Bravais lattices in order to exhibit topological non-triviality. Those topological systems have been described in the four subsequent chapters.

Chapter 2: We report the appearance of nontrivial topological phases in a tight-binding model on the stuffed honeycomb lattice. The model contains NN and NNN hopping terms coupled with an additional phase depending on the direction of hopping. CI and CSM phases emerge with the variation of hopping parameters. Nonzero Chern numbers characterizing the bands and the existence of topologically protected edge states in the gap between the relevant bands confirm the presence of those phases. We show that adding an extra basis to Haldane's honeycomb model can lead to an additional topological phase characterized by Chern number ± 2. Transition between different topological phases driven by the hopping parameters has been illustrated in the topological phase diagram of the system. Zero temperature Hall conductivity along with density of states is evaluated. Topological properties of another tight-binding model on the stuffed square lattice are also reported in this study.

Chapter 3: A tight-binding model on square-octagon lattice with NN and NNN hoppings is considered. The system is topologically trivial although it exhibits quadratic band-touching points in its band-structure. It is shown that the system drives towards topologically non-trivial phases as soon as it is exposed to monochromatic circularly polarized light. Multiple topological phases are found to emerge with the variation of amplitude of radiation. An effective time-independent Hamiltonian of the system is obtained following the Floquet-Bloch formulation. Quasi-energy band-structures along with definite values of Chern numbers for respective bands are obtained. Characterization of topologi-

cal phases are made in terms of band structure and Chern numbers. In addition, Hall conductance and topologically protected chiral edge states are obtained to explain the topological properties. The system undergoes a series of topological phase transitions among various topological phases upon variations of both amplitude of radiation and hopping strengths. It exhibits CI and CSM phases depending on the values of lattice filling.

Chapter 4: In this chapter, topological properties of a FM Heisenberg model on a breathing kagome lattice are investigated extensively in the presence of DMI. While the kagome ferromagnet hosts only a single first order topological phase, the breathing kagome system exhibits multiple first and second order topological phases along with their coexistence. Magnon dispersion relation is obtained by using linear spin wave theory. Flat band and Dirac cones are obtained in the absence of DMI. A topological phase diagram is presented where several first and second order phases as well as their overlap are identified. Values of thermal Hall conductivity for all the first order phases are obtained. Distinct first order phases are characterized by different sets of Chern numbers in association with the chiral edge states in accordance to the first order bulk-boundary-correspondence rule. Second order phase is characterized by polarization along with the emergence of corner states. Violation of the second order bulk-corner correspondence rule has been noted in some regions.

Chapter 5: Existence of nontrivial topological phases in a tight binding Haldane-like model on the depleted Lieb lattice is reported. This two-band model is formulated by considering the NN, NNN and next-NNN (NNNN) hopping terms along with complex phase which breaks the TRS of this semi-metallic system. Topological feature of this model is studied along with the presence of sublattice symmetry breaking staggered onsite energy. Combined effect of these two broken symmetries is found crucial for an additional transition between non-

trivial and trivial phases. System exhibits two types of phase transitions, say, between two nontrivial phases and nontrivial to trivial phases. Nonzero Chern numbers, existence of Hall plateau and symmetry protected edge states confirm the presence of the nontrivial phases. This two-band system hosts four different types of phases where two are topological. Additionally topological properties of stacked bilayer of the depleted Lieb lattices are also studied with similar Haldane-like Hamiltonian. This four-band system is found to host Chern insulating phases, with higher values of Chern numbers supported by in-gap edge states.

The list of abbreviations along with the symbols for several physical quantities used in this thesis are given below. They will be defined again on their first appearance in the text.

Table 1.2: The abbreviations

TI	topological insulator
IQHE	integer quantum Hall effect
QSHE	quantum spin Hall effect
FQHE	fractional quantum Hall effect
HOTI	higher order topological insulators
TPT	topological phase transition
CI	Chern insulators
1D	one-dimensional
2D	two-dimensional
3D	three-Dimensional
TKNN	Thouless-Kohmoto-Nightingale-den Nijs
QAHE	quantum anomalous Hall effect
SOC	spin-orbit coupling
TRIM	time reversal invariant momentum
CSM	Chern semi-metallic
FM	ferromagnetic
TMI	topological magnon insulator
DMI	Dzyaloshinskii-Moriya interaction
HOTMI	higher order topological magnon insulator
FTI	Floquet topological insulator
FCI	fractional Chern insulator
BBC	bulk-boundary-correspondence
TRS	time-reversal symmetry
PHS	particle-hole symmetry
CS	chiral symmetry
SSH	Su-Schreiffer-Hegger
NN	nearest neighbour
NNN	next-nearest-neighbour
NNNN	next-next-nearest-neighbour
QSH	quantum spin Hall
BZ	Brillouin zone
BHZ	Bernevig-Hughes-Zhang
AFM	antiferromagnetic
AHE	anomalous Hall effect
PBC	periodic boundary condition
DOS	density of states
MHE	magnon Hall effect
SOTI	second order topological insulator
SOTMI	second order topological magnon insulator
LSWT	linear spin wave theory
THC	thermal Hall conductivity

Bibliography

[1] Klitzing K. V., Rev. Mod. Phys. **58**, 519 (1986).

[2] Haldane F. D. M., Phys. Rev. Lett. **61**, 2015 (1988).

[3] Jotzu G., Messer M., Desbuquois R., Lebrat M., Uehlinger T., Greif D. and Esslinger T., Nature **515**, 237-240 (2014).

[4] Kane C. L. and Mele E. J., Phys. Rev. Lett. **95**, 226801 (2005).

[5] Yang S., Gu Z., Sun K. and Das Sarma S., Phys. Rev. B **86**, 241112(R) (2012).

[6] Benalcazar W. A., Bernevig B. A., and Hughes T. L., Science **357**, 61 (2017).

[7] Bernevig B. A., Hughes T. L. and Zhang S. C., Science **314**, 1757 (2006).

[8] Alexandradinata A., Wang C., Duan W., Glazman L., Phys. Rev. X. **8**, 011027 (2018).

[9] Kitaev A. Y., Physics-Uspekhi **44**, 131 (2001).

[10] Ryu S., Schnyder A. P., Furusaki A., and Ludwig A. W. W., New J. Phys., **12**, 065010 (2010).

[11] Hall, E. H., Am. J. Math **2**, 287-92 (1879).

[12] Thouless D. J., Kohomoto M., Nightingale P. and den Nijs M., Phys. Rev. Lett. **49**, 405 (1982).

[13] Chang C. Z., Zhang, J. and Feng X. et al., Science **340**, 167-70 (2013).

[14] Konig M., Wiedmann S., Brune C., Roth A., Buhmann H., Molenkamp L. W., Qi X. L. and Zhang S. C., Science **318**, 766-70 (2007).

[15] Fu L. and Kane C.L., Phys. Rev. Lett. **98**, 106803 (2007).

[16] Fu L. and Kane C.L., Phys Rev B **76**, 045302 (2007).

[17] Hatsugai Y., Phys. Rev. Lett. **71**, 3697 (1993).

[18] Hatsugai Y., Phys. Rev. B **48**, 11851 (1993).

[19] Hasan M. Z. and Kane C. L., Rev. Mod. Phys. **82**, 3045 (2010).

[20] Dey B. and Ghosh T. K., Phys. Rev. B **99** 205429 (2019).

[21] Mondal S. and Basu S., Phys. Rev. B **107** 035421 (2023).

[22] Dey B., Kapri P., Pal O. and Ghosh T. K., Phys. Rev. B **101**, 235406 (2020).

[23] Weeks C. and Franz M. Phys. Rev. B **82** 085310 (2010).

[24] Liu X. P., Chen W. C., Wang Y. F. and Gong C. D., J. Phys.:Condens. Matter **25** 305602 (2013).

[25] Guo H. M. and Franz M., Phys. Rev. B **80**, 113102 (2009).

[26] Sil A. and Ghosh A. K., J. Phys.: Condens. Matter **32**, 025601 (2019).

[27] Mondal S. and Basu S., Phys. Rev. B **108**, 045307 (2023).

[28] Sun K., Gu Z., Katsura H. and Das Sarma S., Phys. Rev. Lett. **106**, 236803 (2011).

[29] Chen W. C., Liu R., Wang Y. F. and Gong C. D., Phys. Rev. B **86**, 085311 (2012).

[30] Chen M. and Wan S., J. Phys.: Condens. Matter **24**, 325502 (2012).

[31] Kargarian M. and Fiete G. A., Phys. Rev. B **82**, 085106 (2010).

[32] Kellendonk J., Richter T. and Schulz-Baldes, H., Rev. Math. Phys. **14(1)**, 87-119 (2002).

[33] Kudo K., Yoshida T. and Hatsugai Y., Phys. Rev. Lett. **123**, 196402 (2019).

[34] Martinez Alvarez V. M. and Coutinho-Filho M. D., Phys. Rev. A. **99**, 013833 (2019).

[35] Zhang L., Ren J., Wang J. S. and Li B., Phys. Rev. B **87**, 144101 (2013).

[36] Owerre S. A., Phys. Rev. B **95**, 014422 (2017).

[37] Morimoto T. and Furusaki A., Phys. Rev. B **88**, 125129 (2013).

[38] Fu L., Phys. Rev. Lett. **106**, 106802 (2011).

[39] Benalcazar W. A., Bernevig B. A., and Hughes T. L., Phys. Rev. B **96**, 245115 (2017).

[40] Peng Y., Bao Y., and Von Oppen F., Phys. Rev. B **95**, 235143 (2017).

[41] Langbehn J., Peng Y., Trifunovic L., Von Oppen F., and Brouwer P. W., Phys. Rev. Lett. **119**, 246401 (2017).

[42] Song Z., Fang Z., and Fang C., Phys. Rev. Lett. **119**, 246402 (2017).

[43] Lahiri S. and Basu S., Scientific Reports **14**, 1880 (2024).

[44] Wakao H., Yoshida T., Araki H., Mizoguchi T., and Hatsugai Y., Phys. Rev. B. **101**, 094107 (2020).

[45] Inoue J., Phys. Rev. B **81**, 125412 (2010).

[46] Oka T. and Aoki H., Phys. Rev. B **79**, 081406 (2009).

[47] Wang Y. F., Gu Z. C., Gong C. D. and Sheng D. N., Phys. Rev. Lett. **107**, 146803 (2011).

[48] Regnault N. and Bernevig B. A., Phys. Rev. X **1**, 021014 (2011).

[49] Tsui D. C., Stormer H. L. and Gossard A. C., Phys. Rev. Lett. **48**, 1559-62 (1982).

[50] Sato M. and Ando Y., Rep. Prog. Phys. **80**, 076501 (2017).

[51] Sato M. and Fujimoto S., J. Phys. Soc. Jpn. **85**, 072001 (2016).

[52] Young S. M., Zaheer S., Teo J. C. Y., Kane C. L., Mele E. J. and Rappe A. M., Phys. Rev. Lett. **108**, 140405 (2012).

[53] Wan X. G., Turner A. M., Vishwanath A. and Savrasov S. Y., Phys. Rev. B **83**, 205101 (2011).

[54] Pancharatnam, S., Proc. Indian Acad. Sci. **44**, (5): 247-262 (1956).

[55] Berry, M. V., Proceedings of the Royal Society A.**392**, (1802): 45-57 (1984).

[56] Griffiths D. J., Introdution to Quantum Mechanics, Second Edition, Pearson Prentice Hall, New Jersey (2005).

[57] Nascimento L. O., Braz. J. Phys. **47**, 215 (2017).

[58] Kohmoto M., Ann. Phys. **160**, 343-354 (1985).

[59] Tong D., arXiv:1606.06687 (2016).

[60] Sticlet D., PiÃľchon F., Fuchs J. N., Kalugin P. and Simon P., Phys. Rev. B **85**, 165456 (2012).

[61] Ezawa M., Phys. Rev. Lett. **120**, 026801 (2018).

[62] Altland A. and Zirnbauer M. R., Phys. Rev. B **55**, 1142-1161 (1997).

[63] Heeger A. J., Kivelson S., Schrieffer J. R. and Su W. P., Rev. Mod. Phys. **60**, 781 (1988).

[64] Atala M., Aidelsburger M., Barreiro J. T., Abanin D., Kitagawa T., Demler E. and Bloch I., Nature Physics **9**, 795 (2013).

[65] Li X., Meng Y., Wu X., Yan S., Huang Y., Wang S. and Wen W., Appl. Phys. Lett. **113**, 203501 (2018).

[66] Kane C. L. and Mele E. J., Phys. Rev. Lett. **95**, 146802 (2005).

[67] Redlich A. N., Phys. Rev. D **29**, 2366 (1984).

[68] Fukui T., Hatsugai Y. and Suzuki H., J. Phys. Soc. Jpn. **74**, 1674 (2005).

[69] Jiménez-García K., LeBlanc L. J., Williams R. A., Beeler M.C., Perry A. R. and Spielman I. B., Phys. Rev. Lett. **108**, 225303 (2012).

[70] Wu C., Phys. Rev. Lett. **101**, 186807 (2008).

[71] Rechtsman M., Zeuner J., Plotnik Y., Lumer Y., Podolsky D., Dreisow F., Nolte S., Segev M. and Szameit A., Nature **496**, 196-200 (2013).

[72] Katsura H., Nagaosa N. and Lee P. A., Phys. Rev. Lett. **104**, 066403 (2010).

[73] Chisnell R., Helton J.âĂĽS., Freedman D.âĂĽE., Singh D.âĂĽK., Bewley R.âĂĽI., Nocera D.âĂĽG. and Lee Y.âĂĽS., Phys. Rev. Lett. **115**, 147201 (2015).

[74] Schindler, F., Cook A. M., Vergniory M. G., Wang Z., Parkin S. S. P., Bernevig B. A. and Neupert T., Science Advances, **4(6)**, eaat0346 (2018).

[75] Li X. and Liu F., Phys. Rev. B **107**, 224101 (2023).

[76] Tu N., Tanabe Y., Satake Y., Huynh K. K. and Tanigaki K., Nat Commun **7**, 13763 (2016).

[77] Bose I. and Ghosh A. K., Phys. Rev. B **56**, 3149 (1997).

[78] Deb M. and Ghosh A. K., J. Magn. Magn. Mater. **533**, 167968 (2021).

[79] Debnath S. and Basu S., arXiv:2409.19343 (2024).

Chapter 2

Topology on Stuffed Honeycomb Lattice

2.1 Overview

In this chapter, we search for nontrivial topological phase on the stuffed honeycomb lattice, which is a three-band system by itself but actually interpolates the triangular (Bravais) and two-band honeycomb (non-Bravais) lattices. Being a two-band system honeycomb model is capable to exhibit nontrivial topological phase in the presence of phase-coupled hopping terms, while triangular lattice fails to do so under the same situation for obvious reason. Therefore, emergence of new topological phase in the interpolating regime will be of great interest. Eventually it turns out that addition of extra sublattice does lead to the emergence of new topological phase in the resulting system. In support of this claim, another tight-binding model on stuffed square lattice is hereby introduced which is capable to host new topological phase.

The antiferromagnetic (AFM) Heisenberg model on this lattice was studied previously in search of new spin-liquid phase. However, in that case, triangular,

honeycomb as well as the intermediate stuffed honeycomb lattices were found to host similar kind of spin-liquid phase [1]. Interpolating lattices are capable to exhibit nontrivial spin chirality, which may lead to anomalous Hall effect (AHE) [2]. Quantization of AHE generates topological phase or QAHE phase, where the quantum number is the topological invariant of the system. So, adding another basis to Haldane's honeycomb model could provide the platform to explore novel topological phases in tight-binding regime.

With this motivation, we formulated a three-band tight-binding model on this lattice in the presence of NN and NNN hopping terms. An additional phase coupled with NNN hopping has been considered to incorporate nontriviality in the otherwise trivial system. The sign of this phase depends on the direction of hopping. This phase breaks the TRS in the momentum space representation of the Hamiltonian. Also, the net flux of the gauge field passing through a unit cell is zero. The system is shown to exhibit distinct TI phases characterized by different sets of Chern numbers. Transition between those phases are driven by the modulation of hopping strengths. Chiral edge states are simultaneously obtained in the finite system.

In section 2.2, stuffed honeycomb lattice is described and the tight-binding Hamiltonian is formulated. This is followed by section 2.3, where behavior of the relevant physical quantities to study topological properties is presented. In the following section 2.4, stuffed square lattice is introduced and its topological phases are presented. In next section 2.5, the structures of the Gell-Mann matrices are given. Finally, in section 2.6, discussions and conclusions on this work are summarized.

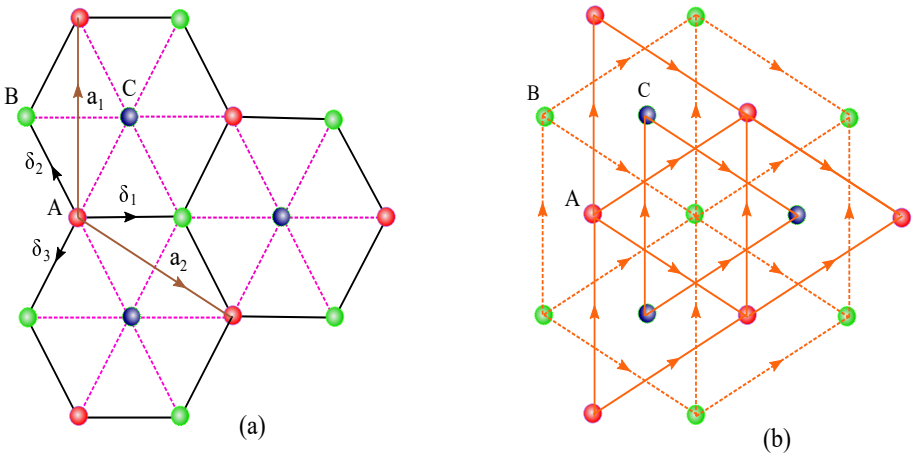

Figure 2.1: (a) NN interactions are shown. Hopping amplitude is t_1 along the solid lines and t_2 along dashed lines. Lattice vectors are shown as $\mathbf{a_1}$ and $\mathbf{a_2}$. Three types of lattice sites A, B, C are drawn as red, green and blue spheres, respectively. $\delta_\mathbf{1}, \delta_\mathbf{2}, \delta_\mathbf{3}$ are the three NN vectors. (b) NNN interactions are shown. Hopping amplitude is t_3 along the solid lines and $-t_3$ along dashed lines. Sign of the phase is assumed positive when hopping is along the direction of arrow and otherwise negative.

2.2 Stuffed Honeycomb Lattice and Formulation of Hamiltonian

Stuffed honeycomb lattice originates as a result of coupling between one honeycomb lattice and one triangular lattice which is shown in Fig. 2.1 (a). The honeycomb lattice is composed of two triangular lattices with site indices A and B, while the site index of the additional triangular lattice is C. So, essentially it is tripartite and composed of three interpenetrating identical triangular lattices. The resulting lattice is decomposed in this manner to define the hopping parameters for this tight-binding model in a comfortable way. We consider three different species of spinless fermions each for three sublattices to introduce the

Hamiltonian

$$
\begin{aligned}
H \;=\; & -\sum_{\langle ij\rangle}\left(t_1\, A_i^{\dagger}B_j + t_2\,(A_i^{\dagger}C_j + B_i^{\dagger}C_j) + H.c\right) \\
& -\;\sum_{\langle\langle ij\rangle\rangle}\left(t_{ij}\, e^{i\phi_{ij}}\,(A_i{}^{\dagger}A_j + B_i{}^{\dagger}B_j + C_i{}^{\dagger}C_j) + H.c\right) \\
& +\;\sum_i \epsilon_i\left(A_i{}^{\dagger}A_i + B_i{}^{\dagger}B_i + C_i{}^{\dagger}C_i\right), \qquad (2.1)
\end{aligned}
$$

where i is the site index. $\langle\cdot\rangle$ and $\langle\langle\cdot\rangle\rangle$ indicate the summations over NN and NNN pairs. ${\alpha_i}^{\dagger}(\alpha = A, B, C)$ is the fermion creation operator at site i. t_1 is the intra-honeycomb NN hopping amplitude and t_2 is the NN hopping amplitude between the honeycomb and triangular sublattices (Fig. 2.1 (a)). t_{ij} is the NNN hopping amplitude irrespective of sublattices but $t_{ij} = t_3\,(-t_3)$ for solid (dashed) lines as shown in Fig. 2.1 (b). The direction of the phases $\phi_{ij} = \pi/2$ is indicated by the arrow in Fig. 2.1 (b). ϵ_i is the onsite energy.

This model will become the honeycomb one when both t_2 and t_3 across the C-C bonds vanish. Similarly, it interpolates separately to triangular and dice lattices at t_2=t_1 and at t_2=∞, respectively [1]. The unit cell is defined by the primitive vectors $\mathbf{a_1} = \sqrt{3}\,(0,1)$ and $\mathbf{a_2} = \sqrt{3}\left(\sqrt{3}/2, -1/2\right)$, where the NN distance is taken to be unity. NN sites are connected by the vectors δ_1, δ_2 and δ_3 where $\delta_1 = (1,0) = 1/3\,(\mathbf{a_1} + 2\mathbf{a_2})$, $\delta_2 = \left(-1/2, \sqrt{3}/2\right) = 1/3\,(\mathbf{a_1} - \mathbf{a_2})$ and $\delta_3 = \left(-1/2, -\sqrt{3}/2\right) = -1/3\,(2\mathbf{a_1} + \mathbf{a_2})$. All those vectors are shown in Fig. 2.1 (a). The corresponding reciprocal lattice vectors are $\mathbf{b_1} = \left(2\pi/3, 2\pi/\sqrt{3}\right)$ and $\mathbf{b_2} = (4\pi/3, 0)$ which span the hexagonal first Brillouin zone.

Hamiltonian in the momentum space is written by invoking periodic boundary conditions (PBC) along both $\mathbf{a_1}$ and $\mathbf{a_2}$ directions,

$$
H\,(\mathbf{k}) = \sum_k {\psi_k}^{\dagger} h\,(\mathbf{k})\,\psi_k, \qquad (2.2)
$$

where $\mathbf{k} = (k_x, k_y)$, $\psi_{\mathbf{k}} = (A_{\mathbf{k}}, B_{\mathbf{k}}, C_{\mathbf{k}})$ is a 3-component spinor and $h(\mathbf{k})$ is a 3×3 matrix. This $h(\mathbf{k})$ can be expressed in terms of eight Gell-Mann matrices, λ_i as

$$h\left(\mathbf{k}\right) = \sum_i h_i \, \lambda_i + a \, I_3, \tag{2.3}$$

with

$$\begin{aligned}
h_1 &= t_1 \Big[\cos\left(\frac{k_1 + 2k_2}{3}\right) + \cos\left(\frac{k_1 - k_2}{3}\right) \\
&\quad + \cos\left(\frac{2k_1 + k_2}{3}\right) \Big], \\
h_2 &= -t_1 \Big[\sin\left(\frac{k_1 + 2k_2}{3}\right) + \sin\left(\frac{k_1 - k_2}{3}\right) \\
&\quad - \sin\left(\frac{2k_1 + k_2}{3}\right) \Big], \\
h_3 &= 2t_3 f(k_1, k_2), \\
h_4 &= h_1\left(\frac{t_2}{t_1}\right) = h_6, \\
h_5 &= -h_2\left(\frac{t_2}{t_1}\right) = -h_7, \\
h_8 &= -\frac{4}{2\sqrt{3}} t_3 f(k_1, k_2) + \sqrt{3}\epsilon, \\
a &= \frac{2}{3} t_3 f(k_1, k_2),
\end{aligned} \tag{2.4}$$

where I_3 is the 3×3 identity matrix, $k_1 = \mathbf{k} \cdot \mathbf{a_1} = \sqrt{3}k_y$, $k_2 = \mathbf{k} \cdot \mathbf{a_2} = 3/2k_x - \sqrt{3}/2k_y$ and $f(k_1, k_2) = \Big[\cos\left(k_1 + \pi/2\right) + \cos\left(k_2 + \pi/2\right) + \cos\left(k_1 + k_2 + \pi/2\right)\Big]$. λ_i are shown in the section 2.5. We have written the Hamiltonian matrix in terms of k_1 and k_2 for ease of calculation. Evidently, TRS is broken by the phase $\phi_{ij} = \pi/2$ since $h(\mathbf{k}) \neq h^*(-\mathbf{k})$. Hopping parameters t_2 and t_3 as well as ϵ_i are measured with respect to t_1 which is assumed unity throughout this chapter. The value of ϵ_i is taken as ϵ (-2ϵ) for honeycomb (triangular) sublattice. This special distribution of values of ϵ_i is necessary to open up gaps between the otherwise gapless energy bands.

Signs of hopping terms are taken in such a way that one among the three

terms $h_n (n = 2, 5, 7)$ has sign opposite to that of the remaining two terms. This reverses the Bloch phase of one of the off-diagonal elements of the Hamiltonian with respect to the other two. The off-diagonal upper triangular terms of $h(\mathbf{k})$ are written as

$$\begin{aligned} h_1 - ih_2 &= t_1 e^{i\sum_j \mathbf{k}\cdot\delta_\mathbf{j}}, \\ h_4 - ih_5 &= t_2 e^{i\sum_j \mathbf{k}\cdot\delta_\mathbf{j}}, \\ h_6 - ih_7 &= t_2 e^{-i\sum_j \mathbf{k}\cdot\delta_\mathbf{j}}, \end{aligned} \tag{2.5}$$

where $\mathbf{k} = (k_x, k_y)$. We note that in the case of SU(3)-invariant models such a situation is a necessary criterion for generating the nontrivial topology [3].

Analytic expressions for the eigenvalues of $h(\mathbf{k})$ are given by

$$E_m(\mathbf{k}) = 2\sqrt{\frac{-p}{3}} \cos\left(\frac{1}{3}\arccos\left(\frac{3q}{2p}\sqrt{\frac{-3}{p}}\right) - \frac{2\pi m}{3}\right), \tag{2.6}$$

$m = 0, 1, 2$; where the real parameters are

$$\begin{aligned} p &= -\frac{4}{3}h_3^2(\mathbf{k}) + 2h_3\,\epsilon - ({t_1}^2 + 2{t_2}^2)|f(\mathbf{k})|^2 - 3\,\epsilon^2, \\ q &= \frac{16}{27}\,{h_3}^3(\mathbf{k}) - \frac{4}{3}\,{h_3}^2(\mathbf{k})\,\epsilon - t_1{t_2}^2(f^3(\mathbf{k}) + {f^*}^3(\mathbf{k})) \\ &\quad - 2({t_1}^2 - {t_2}^2)\left(\frac{h_3(\mathbf{k})}{3} - 2\,\epsilon\right)|f(\mathbf{k})|^2. \end{aligned} \tag{2.7}$$

Here, $f(\mathbf{k}) = (h_1(\mathbf{k}) - ih_2(\mathbf{k}))/t_1$. The dispersion relations are shown in Fig. 2.2 (a) and (b) for two sets of (t_2, t_3, ϵ) where nonzero Chern numbers are found.

2.3 Topological Properties

In order to study the topological properties, Chern numbers, Hall conductance at zero temperature (σ_H) and edge states of this model have been calculated.

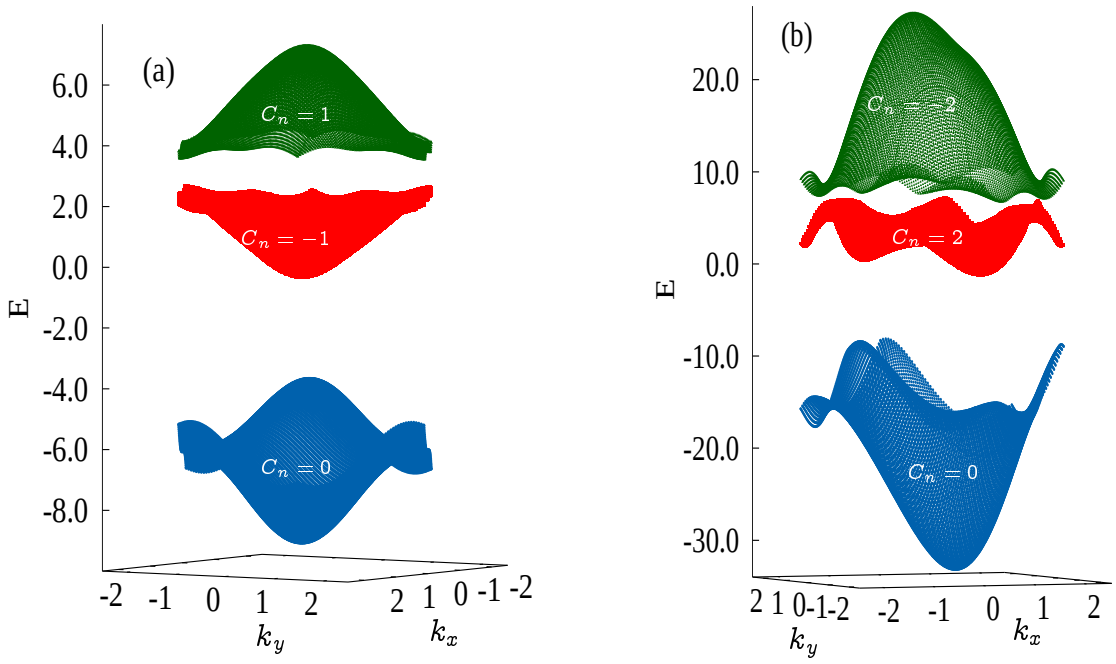

Figure 2.2: Dispersion relation for (a) t_2=0.8, t_3=0.5, ϵ=3.0 and (b) t_2=6.0, t_3=2.0, ϵ=6.0. t_1 is taken to be unity. The Chern numbers of the respective bands are specified.

2.3.1 Chern Numbers and Topological Phase Transition

In the beginning, we calculate C_n of the three bands to characterize the topological phases of this system. As mentioned earlier, C_n is defined as the integration of the Berry curvature and calculated from Eq. 1.6. C_n is well-defined for a particular band as long as it does not touch other neighboring bands *i.e.*, the eigenvalues $E_n(\mathbf{k})$ are not degenerate for any fixed $\mathbf{k}$. In our numerical calculation, we use the discretized version of Eq. 1.6 introduced by Fukui and others [4], explained previously.

In this model, the presence of TRS breaking NNN phase, ϕ_{ij} gives rise to the non-vanishing Chern number, since the TRS invariant Hamiltonian leads to $\Omega_n(\mathbf{k}) = -\Omega_n(-\mathbf{k})$, resulting to $C_n = 0$. Evolution of both the dispersion relation and the topological phases is studied in a space spanned by the three

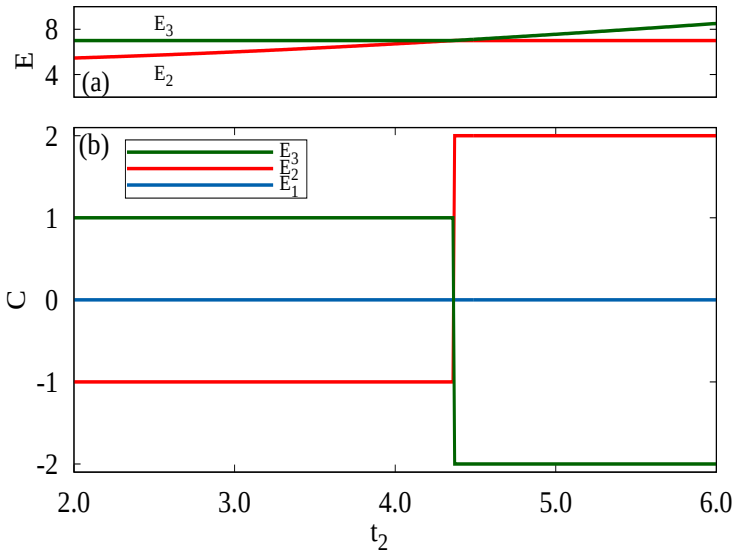

Figure 2.3: (a) Plot of two upper energies (red and green lines) with respect to t_2 showing the crossing between them for $(k_x, k_y) = (\pi, 0)$ or $(0, \pi)$ or (π, π), (same value in each case), $t_3 = 2.0$ and $\epsilon = 6.0$. The lowest energy (blue line) is not shown here. (b) Topological phase diagram for $t_3 = 2.0$ and $\epsilon = 6.0$ with varying t_2. The energy bands are denoted by $E_n(n = 1, 2, 3)$ in ascending order of energy. Summation of Chern numbers over all the bands are zero, which is obvious in the figure. By comparing the diagrams (a) and (b), it is evident that upper band gap closes at the phase transition point, $t_2 = 4.35$.

parameters t_2, t_3 and ϵ. C_n does not change its sign if the sign of t_2 is reversed. However, C_n is found to change its sign when either t_3 or ϕ_{ij} changes its sign.

Let us now explain the evolution of topological phases along definite lines in this three-dimensional parameter space. At first, ϵ and t_3 are kept fixed at 6.0 and 2.0, respectively, while t_2 is allowed to vary. For $t_2 = 0$, the two lower bands touch each other so that Chern numbers are ill-defined. As soon as t_2 becomes greater than 0.0, a pseudo-gap is opened up between the two lower bands and it remains so upto $t_2 < 1.3$. This pseudo-gap becomes a true gap when $t_2 > 1.3$. Along this line, there is always a true gap between the two upper bands as long as $0.0 < t_2 < 4.3$. Chern numbers are defined in these pseudo-gapped regions because of the fact that although the Fermi energy partially

crosses one or more bands, no bands are found to touch each other. On the other hand, Fermi energy never crosses any band where true band gap exists. Pseudo-gapped phase is known as Chern semi-metallic phase, whereas the true gapped phase is known as Chern insulating phase. Thus, nontrivial topological phases appear over this line when $0.0 < t_2 < 4.3$, which is characterized by the value of $C_n = (0, -1, 1)$. Two upper bands touch each other at $t_2 = 4.35$ where the system undergoes a topological phase transition. The closing of band gap at the transition point is essential to ensure the topological phase transition [5]. When $t_2 > 4.4$, the Chern numbers are redistributed as $C_n = (0, 2, -2)$. The Chern number exchange of $\Delta C_n = \pm 3$ may attribute to the fact that at $t_2 = 4.35$, two upper bands touch each other simultaneously at three different points in the first Brillouin zone, say, $(k_x, k_y) = (0, \pi), (\pi, 0), (\pi, \pi)$, each causing an exchange of $\Delta C_n = \pm 1$. No new topological phase is found to emerge upon further increase of t_2, since no band crossing is observed.

In the same way, let us explore the evolution of topological phases along another line by keeping t_2 and ϵ fixed at 0.5 and 3.0, respectively. At $t_3 = 0.0$, the upper two bands touch each other and the Chern numbers are undefined. As soon as t_3 becomes nonzero, a nontrivial phase with $C_n = (0, -1, 1)$ appears but the system exhibits true band gaps upto $t_3 = 1.0$. Afterwards, a pseudo gap develops between the two lower bands. This semi-metallic phase persists upto $t_3 = 2.0$. For $t_3 > 2.0$, the upper band-gap closes and the system becomes trivial. No new topological phase is found to appear further along this line.

Similarly, examining along many other lines in the parameter space, no new phase other than these two topologically different phases characterized by $C_n = (0, -1, 1)$, and $(0, 2, -2)$ are found to exist. In every case, Chern number for the lowest band is zero. The phase diagram is presented in Fig. 2.3 for $t_3 = 2.0$ and $\epsilon = 6.0$ indicating transitions between different phases. It is evident that these

topological phases are robust against change of external parameters as long as the alteration does not cause another band-touching or gap-closing.

The lowest energy band is partially localized on the triangular sublattice because of relatively strong sublattice potential, -2ϵ, with respect to that of honeycomb sublattice, ϵ. In the honeycomb limit, ($i.\ e.\ t_2 = 0$ and across C-C bond $t_3 = 0$), we get only a single phase, $C_n = \pm 1$. Additional $C_n = \mp 2$ phase appears after turning on t_2 which results the stuffed honeycomb lattice. This fact may be termed as generation of additional topological phase due to the entry of an additional sublattice.

It would be worth mentioning in this context that a hard-core bosonic model based on this stuffed-honeycomb lattice has been studied before, where the topological phase with all topologically non-trivial bands $C_n = (-1, -1, +2)$ is found. Additionally, the lowest band ($C_n = 2$) bears high flatness ratio, 15, which gives rise to bosonic FQHE at 1/3 filling and fermionic FQHE at 1/5 filling [6]. On the other hand, in our fermionic model, although the lowest band becomes nearly flat when the values of both t_2 and t_3 are very small, the system is not a potential candidate for FQHE states as this band always carries zero Chern number. However, the topological phase ($C_n = -1, -1, +2$) observed in the bosonic model could be realized in the fermionic counterpart by mimicking both the hopping terms and phase values like the former. As well as, FQHE state could be found in the lowest non-trivial flat band.

2.3.2 Hall conductance at zero temperature

At zero temperature, $\sigma_H(E)$ is estimated numerically by using the Kubo formula [7], mentioned in Eq. (1.7). $\sigma_H(E)$ along with the density of states (DOS) is plotted against Fermi energy in Fig. 2.4 for two different sets of parameters where two distinct topological phases are observed. DOS is useful to locate

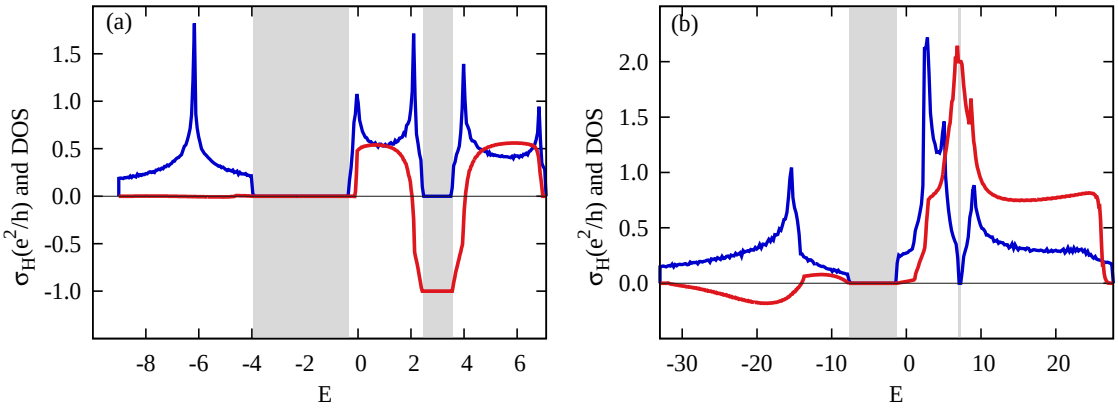

Figure 2.4: The Hall conductance σ_H (red line) and DOS (blue line) with respect to the Fermi energy E for (a) $t_2 = 0.8$, $t_3 = 0.5$, $\epsilon = 3.0$ and (b) $t_2 = 6.0$, $t_3 = 2.0$, $\epsilon = 6.0$. The shaded regions are showing the band-gaps.

the gap in the band diagram where $\sigma_H(E)$ always exhibits a Hall plateau. The height of a Hall plateau can be determined by using Eq. (1.16).

Two prominent Hall plateaus for $\sigma_H = n(e^2/h)$ with $n = (0, -1)$ are observed in Fig. 2.4 (a), which corresponds to the topological phase having $C_n = (0, -1, 1)$. Similarly, in Fig. 2.4 (b) two Hall plateaus exist for $\sigma_H = n(e^2/h)$ with $n = (0, 2)$, but the second one is not prominent in the figure since the band gap is very narrow in this case. This characteristic corresponds to the topological phase having $C_n = (0, 2, -2)$. Band gaps are identified by the shaded regions which hold these Hall plateaus. According to Eq 1.16, the value of $\sigma_H(E)$ over any Hall plateau becomes equal to the sum of all Chern numbers carried by the bands having energy lower than it. So, the sign of $\sigma_H(E)$ will be either positive or negative depending on the distribution of C_n over the energy bands. Also, width of the band gap equals to that of the plateau. DOS exhibits sharp peaks around the energies where $\sigma_H(E)$ undergoes sharp rise and fall. As a result, four sharp peaks in DOS are found in Fig. 2.4 (a). Another sharp peak in DOS at the lowest energy corresponds to the van Hove singularity

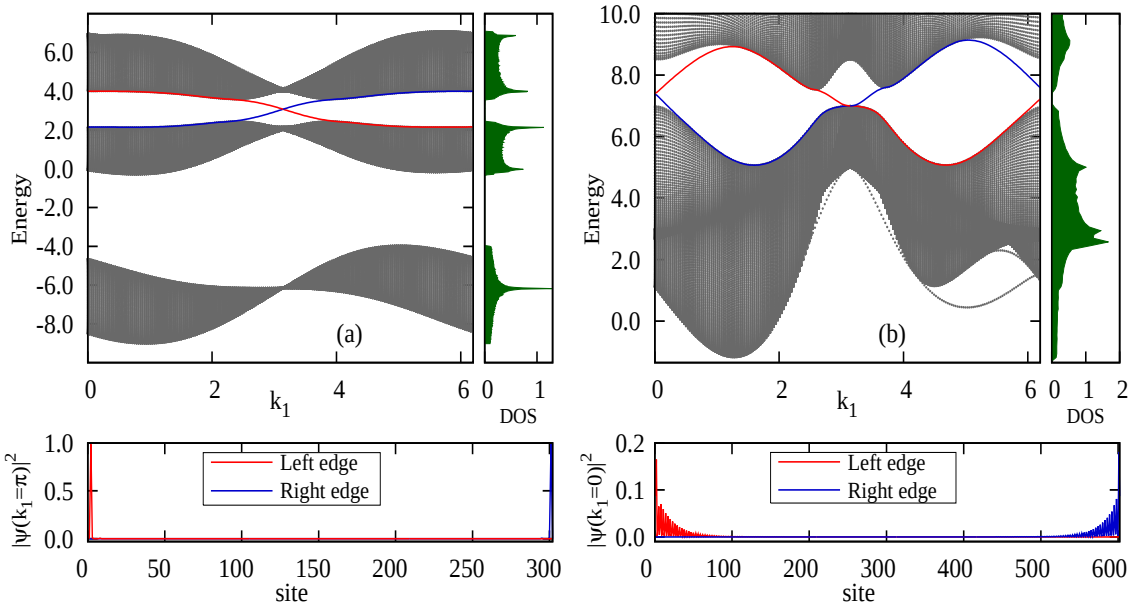

Figure 2.5: Edge states of the stuffed honeycomb lattice considering zigzag edge along $\mathbf{a_2}$ direction are shown in solid lines for (a) $t_2 = 0.8$, $t_3 = 0.5$, $\epsilon = 3.0$ with 100 cells and (b) $t_2 = 6.0$, $t_3 = 2.0$, $\epsilon = 6.0$ with 200 cells. For (b), only the upper band-gap is shown as the energy range being very high, lower gap containing zero edge states is not shown. Lower panels demonstrate the distribution of probability densities of a particular eigenstate with $k_1 = \pi$ for (a) and $k_1 = 0$ for (b). Red (blue) line corresponds to left (right) edge.

in the band diagram.

2.3.3 Edge States

As we have discussed earlier, Chern number is recognized as the bulk property of the system, where edge states correspond to the surface property. However, the presence of non-zero Chern number leaves its signature by generating edge states, and vice versa. To study the properties of edge states in case of nontrivial Chern number, boundary lines or edges are created by removing the periodic boundary condition along $\mathbf{a_2}$ axis, such that, k_2 is no longer a good quantum number for this finite system. But the periodic boundary condition along $\mathbf{a_1}$ is there, so that k_1 acts as a good quantum number like before. The resulting strip

has zigzag left and right edges.

Here, a finite strip of stuffed Honeycomb lattice is considered which has $N = 100$ cells, *i.e.*, 300 sites along $\mathbf{a_2}$ direction. The $3N \times 3N$ Hamiltonian has been constructed, which is a function of k_1 by taking partial Fourier transformation. Diagonalizing that Hamiltonian, the dispersion relation is obtained for $t_2 = 0.8$, $t_3 = 0.5$, $\epsilon = 3.0$, shown in Fig. 2.5 (a), which reveals that the pattern of edge states supports the pattern of Chern numbers $(0, -1, 1)$ for the relevant topological phase of the system. Similarly, for other topological phase, $C_n = (0, 2, -2)$, a honeycomb structure composed of $N = 200$ cells along $\mathbf{a_2}$ axis is considered. The dispersion relation for $t_2 = 6.0$, $t_3 = 2.0$, $\epsilon = 6.0$ is shown in Fig. 2.5 (b). To maintain a rich clarity in the figure, only two upper bands containing the edge states are shown in the second case. The edge states are indeed localized in either left (red curves) or right (blue curves) edge of the finite lattice, as shown in the lower panels of Fig. 2.5. Chiral nature of these edge states are also confirmed from the figures, since the right-going (left-going) states are always localized in the right (left) edge.

As the lowest band always carries zero Chern number, no edge states are found to exist in the lower band gap for both phases. Two pairs of edge states are found in the upper band gap for $C_n = (0, 2, -2)$, in contrast to one pair of that in the upper band gap for $C_n = (0, -1, 1)$ phase. Those results are in accordance with the BBC rule which states that: sum of the Chern number upto the i-th band, $\nu_i = \sum_{j \leqslant i} C_j$, is equal to the number of pair of edge states in the gap [8]. Thus the values of the Chern numbers can be recovered from the edge state pattern itself.

2.4 Stuffed Square Lattice

In order to justify our claim that incorporation of additional sublattice may induce new topological phase, we consider the example of a particular stuffed square lattice. In this body-centered square lattice, a two-orbital (denoted by $I = 1, 2$) square sub-lattice incorporates another single-orbital (denoted by $I = 3$) square sub-lattice in its centers which makes the system a three-band model, as shown in Fig. 2.6 (a). However, in this case, the system is driven towards non-trivial topological phase as soon as the SOC between (1, 2) and 3 is invoked. The Hamiltonian of this tight binding model on this lattice can be written as

$$H = H_{\text{NNN}} + H_{\text{NN}} + H_{\text{SOC}}, \tag{2.8}$$

where

$$H_{\text{NNN}} = -\sum_{\langle\langle jk\rangle\rangle, I=1,2} \left(t_{jk} + (-1)^{I+1} t_1\right) a^{\dagger}_{jI} a_{kI}, \tag{2.9}$$

$$H_{\text{NN}} = -\sum_{\langle jk\rangle} t_2 \, a^{\dagger}_{jI} a_{kI}, \tag{2.10}$$

$$H_{\text{SOC}} = -i \, \lambda_{\text{SOC}} \sum_{\langle jk\rangle} \nu_{jk} \, a^{\dagger}_{jI} \sigma_z a_{kI}. \tag{2.11}$$

Here, t_1 is the NNN hopping parameter between sublattice 1 and 2 while t_2 is the NN hopping parameter between sublattice (1, 2) and 3. λ_{SOC} is the strength of SOC between NN pairs. The term $\nu_{jk} = +1\,(-1)$, when the hopping takes place along (opposite to) the direction of the arrow as shown in Fig. 2.6 (a). a_j ($a^{\dagger}_j$) is the annihilation (creation) operator of electron at site j, such that $a_j = (a_{j\uparrow}, a_{j\downarrow})^T$, where, $a_{j\uparrow}$ ($a_{j\downarrow}$) is the annihilation operator of the electron with up (down) spin. $t_{jk} = +t_1(-t_1)$ for the horizontal (vertical) NNN bond.

After Fourier transformation, the resulting Hamiltonian, $H_{\mathbf{k}}$, comprises two

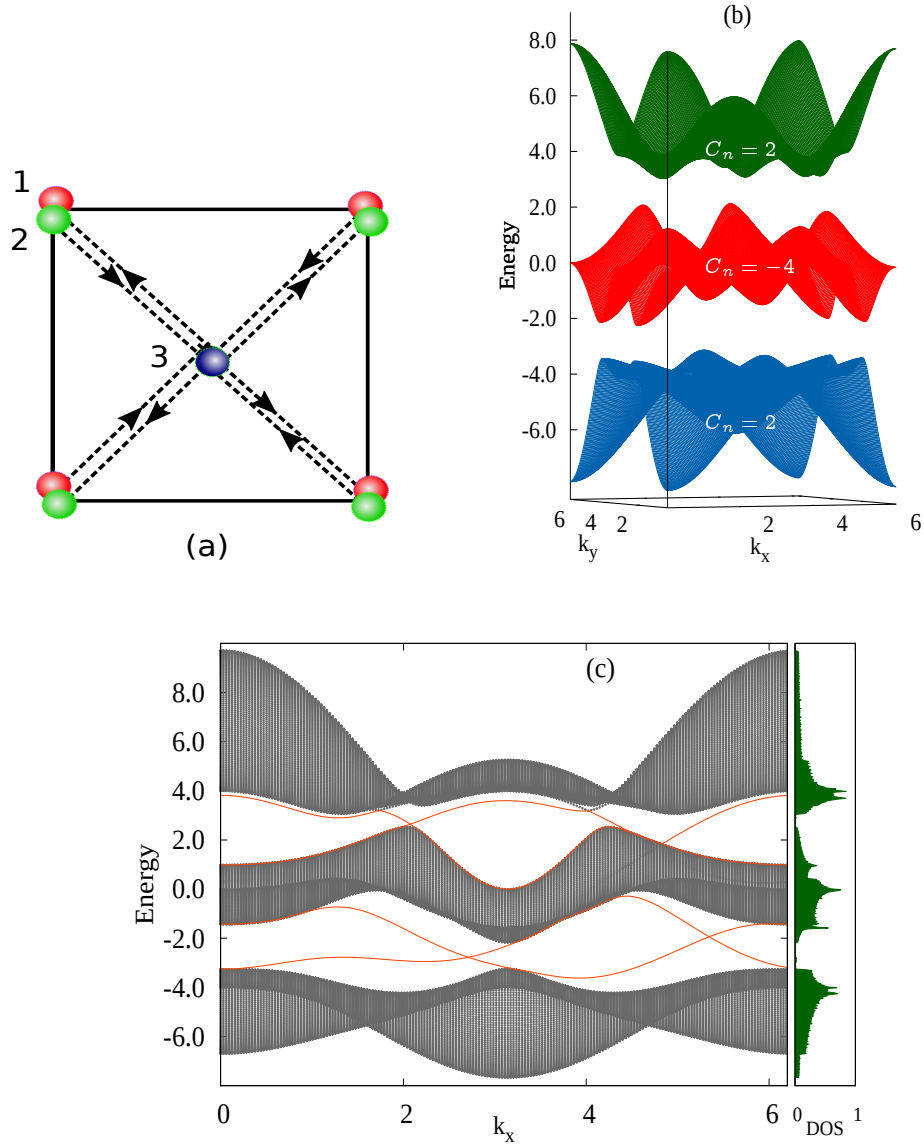

Figure 2.6: (a) Schematic diagram of a unit cell of the stuffed square lattice. Three sublattices 1,2,3 are shown as red, green and blue spheres, respectively. Arrows in the NN bond between (1, 2) and 3 show the direction of spin orbit coupling. (b) Energy spectrum for $t_1 = 1.0, t_2 = 1.2, \lambda_{\text{SOC}} = 0.8$. Chern numbers of respective bands are specified. (c) Edge states of the finite system for the same parameters and 100 unit cells along y-direction. Gapless edge states are shown by solid red lines. Density of states is shown in the side panel.

uncoupled diagonal blocks corresponding to up and down spins, those are related by TRS, *i. e.*, $H^{\uparrow}_{\mathbf{k}} = H^{\downarrow *}_{-\mathbf{k}}$. Now it is sufficient to consider either up- or down-spin sector for the calculation of energy spectrum and topological properties. It is noted that, the up- and down-spin sectors break TRS separately. So, we can treat Chern number as the topological invariant following the previous formulation as described in the main text. If we denote the Chern number for n-th band for up-spin sector as $C^{\uparrow}_n$ and down-spin sector as $C^{\downarrow}_n$, then $C^{\downarrow}_n = -C^{\uparrow}_n$ and spin Chern number for the whole n-th band can be defined as $C^s_n = C^{\uparrow}_n - C^{\downarrow}_n = 2C^{\uparrow}_n$. In the following, we restrict to the spin up sector only and omit the spin symbol for convenience. So,

$$H\left(\mathbf{k}\right) = \sum_k {\psi_k}^{\dagger} h\left(\mathbf{k}\right) \psi_k, \tag{2.12}$$

where $\mathbf{k} = (k_x, k_y)$ and $\psi_{\mathbf{k}} = (c_{\mathbf{k}1}, c_{\mathbf{k}2}, c_{\mathbf{k}3})$ is a three-component spinor. $h(\mathbf{k})$ can be expressed as

$$h\left(\mathbf{k}\right) = \sum_i h_i \, \lambda_i, \tag{2.13}$$

with

$$\begin{aligned}
h_1 &= 2t_1 \left(\cos(k_x) - \cos(k_y)\right), \\
h_2 &= 0 = h_8, \\
h_3 &= 2t_1 \left(\cos(k_x) + \cos(k_y)\right), \\
h_4 &= 4t_2 \cos(k_x/2) \cos(k_y/2) = h_6, \\
h_5 &= -4 \, \lambda_{\mathrm{SOC}} \, \sin(k_x/2) \sin(k_y/2) = -h_7.
\end{aligned} \tag{2.14}$$

When $\lambda_{\mathrm{SOC}} = 0.0$, the three bands touch each other and so the Chern numbers are ill-defined. As soon as λ_{SOC} becomes non-zero, gaps open up between the bands and this time those bands are characterized by definite Chern numbers, $C_n = (2, -4, 2)$. Fig. 2.6 (b) shows the band structure for $t_1 = 1$, $t_2 = 1.2$ and $\lambda_{\mathrm{SOC}} = 0.8$.

For the calculation of edge states, we consider a finite strip of stuffed square

lattice consisting of 100 cells *i. e.*, 300 sites along y-direction. By diagonilizing the resulting Hamiltonian as a function of good quantum number k_x, the dispersion of edge states is obtained, which is shown in Fig. 2.6(c). Two pair of edge states are found in both the band-gaps, which is in accordance with the BBC rule. DOS is shown in the side panel of the associated figure. Therefore, we put forward another example through which we successfully demonstrate the emergence of new topological phase with the addition of extra sublattice where the tight-binding model on the parent lattice was topologically trivial.

2.5 The Gell-Mann matrices

The Gell-Mann matrices are a set of eight traceless 3×3 linearly independent Hermitian matrices spanning the Lie algebra of the SU(3) group. They are given below.

$$\lambda_1 = \begin{pmatrix} 0 & 1 & 0 \\ 1 & 0 & 0 \\ 0 & 0 & 0 \end{pmatrix}, \qquad \lambda_2 = \begin{pmatrix} 0 & -i & 0 \\ i & 0 & 0 \\ 0 & 0 & 0 \end{pmatrix}, \qquad \lambda_3 = \begin{pmatrix} 1 & 0 & 0 \\ 0 & -1 & 0 \\ 0 & 0 & 0 \end{pmatrix},$$

$$\lambda_4 = \begin{pmatrix} 0 & 0 & 1 \\ 0 & 0 & 0 \\ 1 & 0 & 0 \end{pmatrix}, \qquad \lambda_5 = \begin{pmatrix} 0 & 0 & -i \\ 0 & 0 & 0 \\ i & 0 & 0 \end{pmatrix}, \qquad \lambda_6 = \begin{pmatrix} 0 & 0 & 0 \\ 0 & 0 & 1 \\ 0 & 1 & 0 \end{pmatrix},$$

$$\lambda_7 = \begin{pmatrix} 0 & 0 & 0 \\ 0 & 0 & -i \\ 0 & i & 0 \end{pmatrix}, \qquad \lambda_8 = \frac{1}{\sqrt{3}} \begin{pmatrix} 1 & 0 & 0 \\ 0 & 1 & 0 \\ 0 & 0 & -2 \end{pmatrix}. \tag{2.15}$$

2.6 Summary and Discussion

A three-band tight-binding model on the stuffed honeycomb lattice has been proposed where an additional phase associated with the NNN hopping terms is found to break the TRS by yielding a CI phase in the presence of NN hopping. Although the same phase coupled with the NN hopping breaks TRS, it does not give rise to any nontrivial topological phase. The phase is chosen in such a way that the net flux of gauge field per unit cell vanishes. This system exhibits CI and CSM phases with nonzero Chern numbers in the parameter regimes. Also, this one undergoes quantum phase transition between two topological phases driven by the hopping parameters. Hall conductance exhibits prominent IQHE plateaus. The emergence of topologically protected chiral edge states in a strip configuration with open boundary condition is also found when $C_n \neq 0$.

This study reveals the fact that additional triangular sublattice leads to the generation of one additional topological phase in the resulting stuffed honeycomb lattice. It is established that topological phases could be induced within the trivial systems by means of introducing phase dependent hopping terms [9]. So, more additional topological phases may be obtained by choosing those phases and hoppings in different ways. Topological phases with higher Chern numbers could be realized within a system by means of either exposing the systems to polarized light [10] or invoking long distant-neighbor hopping terms [11, 12]. Addition of extra sublattice may pave another route for the engineering of new topological phases wherever it is applicable. Thus, a desired topological phase may be realized in any system by combining those procedures along with the incorporation of additional sublattice. In this context, a tight-binding model is formulated on a body-centered stuffed square lattice which is found to harbour new topological phase. A brief description of the system as well as its topological

properties is available in section 2.4.

The picture of stuffed honeycomb lattice is brought into light in the context of AFM compound, $LiZn_2Mo_3O_8$ [13]. In this material the molecular cluster Mo_3O_8 forms a triangular lattice, however, its spin-liquid property is explained in terms of an effective spin-1/2 Heisenberg model built on the stuffed honeycomb lattice. Likewise, magnetic properties of the partially frustrated triangular AFM material, $RbFeBr_3$, was explained before in terms of distorted triangular lattice, which is essentially the stuffed honeycomb lattice [14]. However, no material is available at this moment where this electronic model could be realized for the verification of its topological properties.

Bibliography

[1] Sahoo J., Kochkov D., Clark B. K. and Flint R., Phys. Rev. B **98**, 134419 (2018).

[2] Nagaosa N., Sinova J., Onoda S., MacDonald A. H. and Ong N. P., Rev. Mod. Phys. **82**, 1539 (2010).

[3] Ray S., Ghatak A. and Das T., Phys. Rev. B. **95**, 165425 (2017).

[4] Fukui T., Hatsugai Y. and Suzuki H., J. Phys. Soc. Jpn. **74**, 1674 (2005).

[5] Hasan M. Z. and Kane C. L., Rev. Mod. Phys. **82**, 3045 (2010).

[6] Wang Y. F., Hong Y., Gong C. D. and Sheng D. N., Phys. Rev. B **86**, 201101(R) (2012).

[7] Thouless D. J., Kohomoto M., Nightingale P. and den Nijs M., Phys. Rev. Lett. **49**, 405 (1982).

[8] Mook A., Henk J. and Mertig I., Phys. Rev. B **90**, 024412 (2014).

[9] Haldane F. D. M., Phys. Rev. Lett. **61**, 2015 (1988).

[10] Sil A. and Ghosh A. K., J. Phys.: Condens. Matter **31**, 245601 (2019).

[11] Sticlet D. and Piéchon F., Phys. Rev. B **87**, 115402 (2013).

[12] Deb M. and Ghosh A. K., J. Phys.: Condens. Matter **31**, 345601 (2019).

[13] Flint R. and Lee P. A., Phys. Rev. Lett. **111**, 217201 (2013).

[14] Adachi K., Takeda K., Matsubara F., Mekata M. and Haseda T., J. Phys. Soc. Jpn. **52**, 2202 (1983).

Chapter 3

Topology on Square Octagon Lattice

3.1 Overview

Through a series of investigations, it has been established that periodic perturbation induced by photo-irradiation can also drive the system into non-trivial topological phase. That particular state of matter is known as Floquet topological insulator [1, 2]. Topological classification of periodically driven quantum systems has been formulated [3]. In order to study the FTI phase in a tight-binding system, one has to develop an appropriate Floquet-Bloch theory on it. A section of investigations is now devoted to find the existence of FTI phase on the systems those were otherwise declared as topologically trivial. These kind of investigations may help the experimentalists to develop suitable techniques for probing the existence of novel topological phases within the materials by irradiating them with polarized light of certain frequency and intensity. In addition, associated topological phase transitions can also be demonstrated by modulating the appropriate parameters of the irradiation [4].

Existence of FTI phase was also predicted in graphene for the first time. Since then there have been several studies on Floquet topological phase on honeycomb

lattice [5, 6, 7, 8, 9] in addition to other two-band systems [10, 11, 12, 13]. It has been shown that the effect of periodically driven circularly polarized light leads to a non-trivial mass term similar to that found in Haldane model [14]. This mass term now becomes a function of both the intensity and the state of polarization of light. So, detection of a particular non-trivial topological phase requires appropriate value of intensity and definite state of polarization of the light. In addition to the honeycomb lattice, effect of photo-irradiation is studied before on three-band tight-binding models formulated on kagomé [15] and Lieb [16] lattices. Again, in these tight-binding models, photo-irradiation opens up gaps in the otherwise gapless spectrum and the resulting energy-bands are found to emerge simultaneously with non-zero Chern numbers. Interestingly, in two-dimensional Floquet systems, evidence of chiral edge states is found even though the Chern numbers of the respective bulk bands are zero, which indicates the violation of BBC rule for that particular system [3, 17]. Therefore, determination of both Chern numbers for the bulk-bands and edge states between the respective bands are necessary to confirm the topological phases. Recently, the bosonic counterpart of FTI phase has been formulated in magnetic systems [18].

In this work, we pay attention to the four-band tight-binding model on square-octagon lattice. It has been reported that this model exhibits Z_2 band-insulating and CI phases in the presence of spin-orbit coupling [19] and external magnetic flux [20, 21], respectively. Topological phase transition (TPT) driven by SOC and exchange field are also found on this lattice [22]. Outcome of those studies based on square-octagon lattice along with the emergence of photoinduced topological phases on kagomé and Lieb lattices motivate us to search the FTI phase on this particular lattice.

The intrinsic tight-binding model on square-octagon lattice has an interesting band-structure which includes a pair of flat band and five different band-

touching points. The coherent photo-irradiation perturbs the band structure in such a manner that either true or pseudo band-gaps appear depending on the value of its amplitude. System undergoes a series of TPT with the variation of amplitude, where successive band-touching and gap-opening processes occur at the transition points separating the different topological phases. As a result, multiple topological phases are found to emerge in the parameter space, which can be categorized as either CSM or CI phases depending on the nature of band-gap. CI phase corresponds to true band-gap while CSM phase appears in case of pseudo band-gap. Rapid variation of topological phases with respect to the amplitude of irradiation is observed which is not reported before for the cases of honeycomb, kagomé and Lieb lattices. Chiral edge states are found to appear in finite system according to the BBC rule which confirms the existence of non-trivial topological phases.

In section 3.2, square-octagon lattice is described and the tight-binding Hamiltonian is formulated. Outline of Floquet theory and development of Floquet-Bloch effective Hamiltonian are presented in section 3.3. Detailed characterization of various topological phases and transition among them along with explanations are provided in section 3.4. Section 3.5 contains discussion on the theme of this work.

3.2 Model Hamiltonian and Band Structure

We consider a two-dimensional square-octagon lattice model consisting of two elementary plaquettes: square and octagon as shown in Fig. 3.1. The same lattice is noted before as 1/5-depleted square lattice [23] and Archimedean lattice T11 [24] in the context of investigations of several other properties based on it. The coordination number of this non-Bravais lattice is three which is similar to

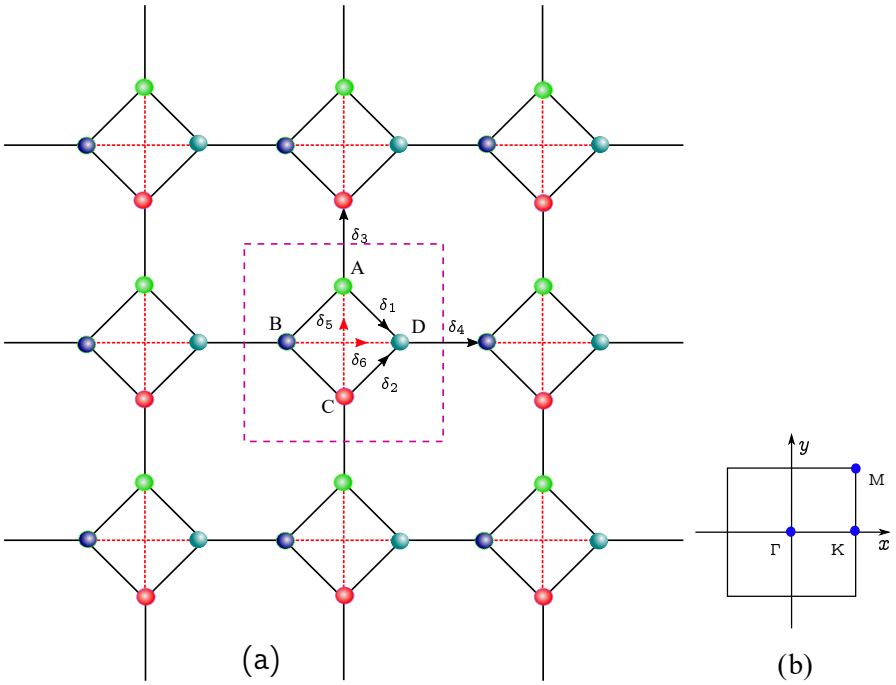

Figure 3.1: (a) The geometry of square-octagon lattice. A, B, C, D denote four different sites in the unit cell which is shown by large square (pink dashed lines). Strength of NN hopping along sides (black solid lines) of small square is t_1. Strength of NNN hopping along diagonals (red dotted lines) of small square is t_2. $\boldsymbol{\delta}_1, \boldsymbol{\delta}_2, \boldsymbol{\delta}_3, \boldsymbol{\delta}_4$ are the NN vectors and $\boldsymbol{\delta}_5, \boldsymbol{\delta}_6$ are the NNN vectors. (b) The first Brillouin zone of the lattice. High-symmetry points Γ, K and M have been marked.

that of honeycomb lattice, another non-Bravais one. However, this lattice can be considered as composed of four interpenetrating square sub-lattices each of which is formed by lattice points those are drawn by four different colours in Fig. 3.1. The tight binding Hamiltonian considering NN and NNN interactions can be written as

$$H = -\sum_{(m,n)}\left[t_1\sum_{\langle ij\rangle} c^{\dagger}_{m,n,i}\, c_{m,n,j} + t_2 \sum_{\langle\langle ij\rangle\rangle} c^{\dagger}_{m,n,i}\, c_{m,n,j} + H.c\right]. \tag{3.1}$$

The first summation (m, n) runs over the unit cell indices, while the second

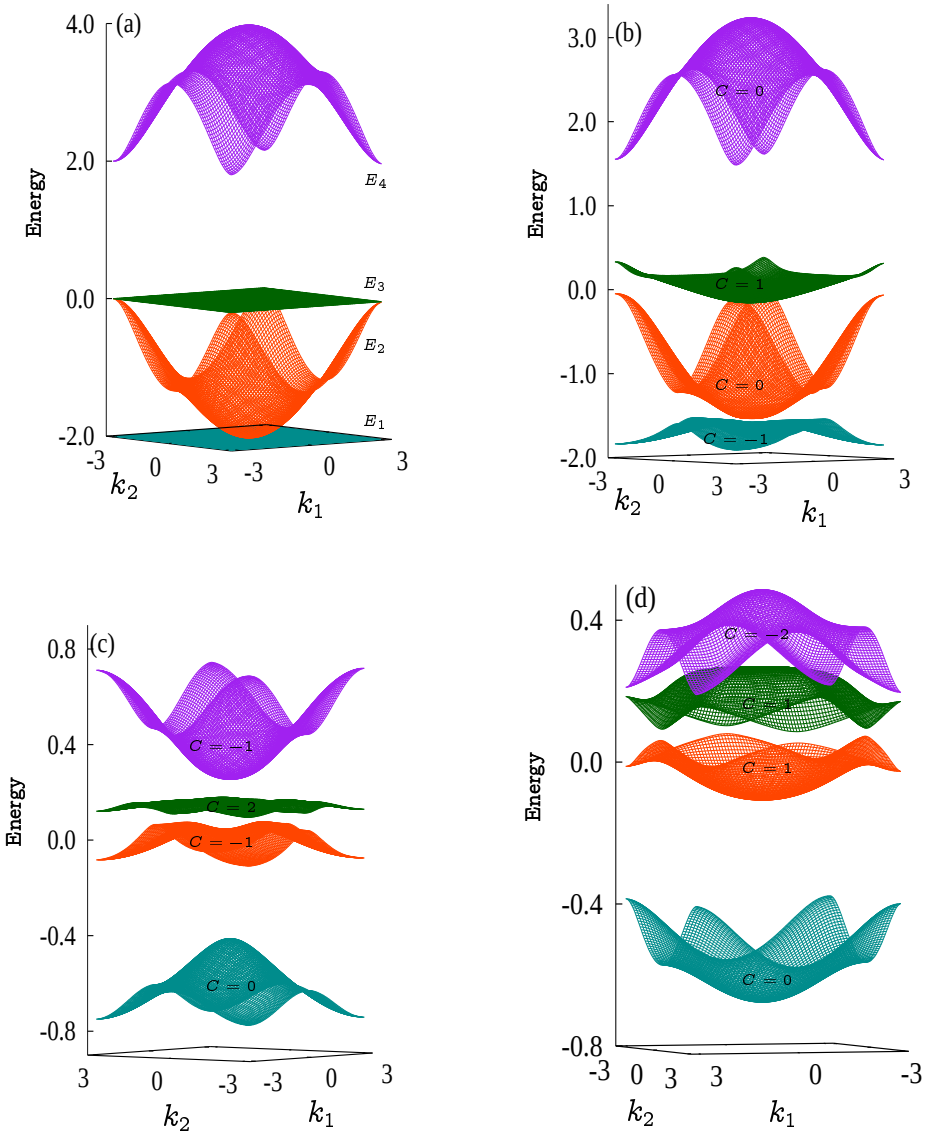

Figure 3.2: (a) Band diagram of tight-binding square-octagon lattice without any external perturbation when $t_2 = 1.0$. Floquet-Bloch band diagram in the presence of circularly polarized light for (b) $t_2 = 1.0\ \Omega = 7, A_0 = 0.8$, (c) $t_2 = 1.0, \Omega = 10, A_0 = 2.1$, (d) $t_2 = 0.6, \Omega = 10, A_0 = 2.7$.

summations $\langle\cdot\rangle$ and $\langle\langle\cdot\rangle\rangle$ run over NN and NNN pairs, respectively. $c^{\dagger}_{m,n,i}\,(c_{m,n,i})$ is the creation (annihilation) operator for an electron at the i-th site of the (m,n)-th unit cell. t_1 is the strength of NN hopping while t_2 is that of NNN hopping along the diagonals of each square plaquette. By setting the distance between NN points to be unity, four NN vectors are defined as $\boldsymbol{\delta}_1 = 1/\sqrt{2}\,(1,-1)$, $\boldsymbol{\delta}_2 = 1/\sqrt{2}\,(1,1)$, $\boldsymbol{\delta}_3 = (0,1)$, and $\boldsymbol{\delta}_4 = (1,0)$. Similarly, two NNN vectors are $\boldsymbol{\delta}_5 = \sqrt{2}\,(0,1)$, and $\boldsymbol{\delta}_6 = \sqrt{2}\,(1,0)$. The lattice translation vectors are $\boldsymbol{a}_1 = \left(1+\sqrt{2},0\right)$ and $\boldsymbol{a}_2 = \left(0,1+\sqrt{2}\right)$. Position of each unit cell is defined by $\boldsymbol{R}\,(m,n) = m\boldsymbol{a}_1 + n\boldsymbol{a}_2$. We set $t_1 = 1$ throughout this chapter.

Fourier transforming to the momentum space, the Hamiltonian becomes $H = -\sum_{\mathbf{k}} \psi^{\dagger}_{\mathbf{k}}\, H(\mathbf{k})\, \psi_{\mathbf{k}}$, where

$$H(\mathbf{k}) = \begin{pmatrix} 0 & t_1 & t_1 e^{ik_2} + t_2 & t_1 \\ t_1 & 0 & t_1 & t_1 e^{-ik_1} + t_2 \\ t_1 e^{-ik_2} + t_2 & t_1 & 0 & t_1 \\ t_1 & t_1 e^{ik_1} + t_2 & t_1 & 0 \end{pmatrix}, \tag{3.2}$$

with $\psi_{\mathbf{k}} = (A_{\mathbf{k}}, B_{\mathbf{k}}, C_{\mathbf{k}}, D_{\mathbf{k}})^T$, where $\alpha_{\mathbf{k}}$ with $\alpha = A, B, C, D$ are the electron annihilation operators on the four basis sites in the square unit cell, $k_1 = \boldsymbol{k}\cdot\boldsymbol{a}_1$ and $k_2 = \boldsymbol{k}\cdot\boldsymbol{a}_2$.

Diagonalizing the Hamiltonian we get two flat bands, (E_1, E_3) and two dispersive bands with energies $E_{2,4}(\mathbf{k}) = 1 \pm \sqrt{5 + 2\cos k_1 + 2\cos k_2}$, as shown in Fig. 3.2 (a), when $t_2 = 1.0$. The bands are denoted as E_1, E_2, E_3 and E_4 in the ascending order of energy. We note that, the lower two bands touch at the Γ point while the energy bands $E_2(\mathbf{k})$ and E_3 touch at four M points of the first Brillouin zone. All these are quadratic band touching points since the energy of the lower dispersive band, $E_2(\mathbf{k})$, is found to become proportional to the square of the wave-vectors when expanded in the vicinity of those points as shown

below.

$$E_2(k_1,k_2)|_{k_1,k_2\to 0} = -2 + \frac{{k_1}^2 + {k_2}^2}{6},$$
$$E_2(k_1,k_2)|_{k_1,k_2\to \pi} = -\frac{(k_1-\pi)^2}{2} - \frac{(k_2-\pi)^2}{2}. \tag{3.3}$$

The model without NNN hopping has been studied before in the absence of circularly polarized light. In this case, Dirac cones are found to appear at Γ and M points when the intra- and inter-square-plaquette NN hopping strengths are different. [23].

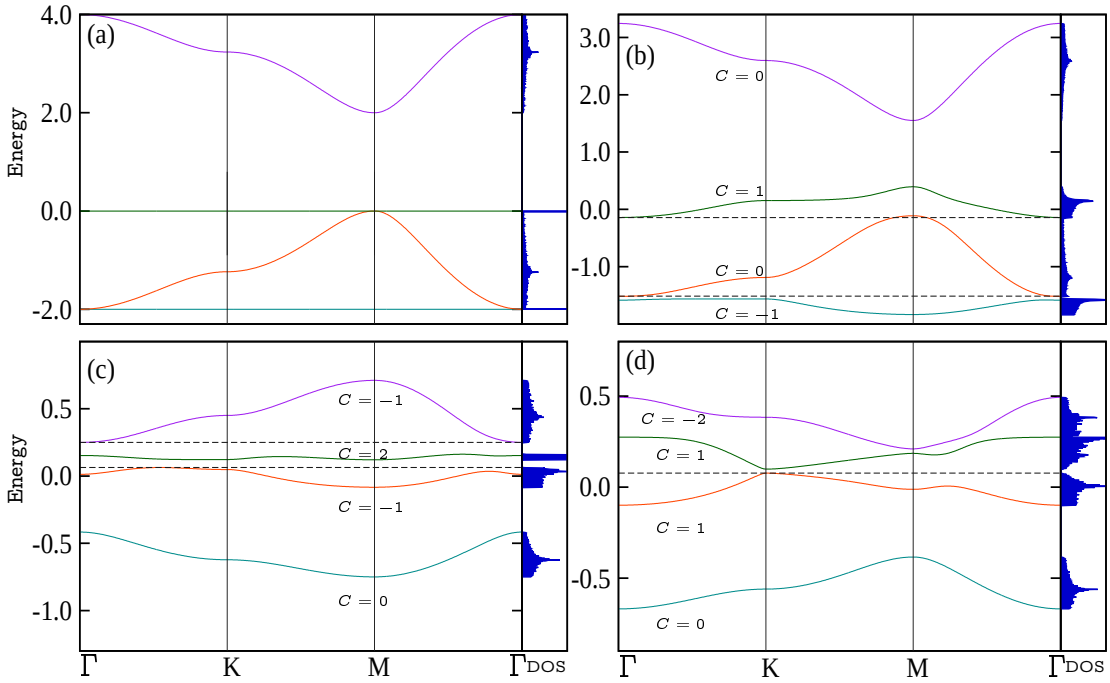

Figure 3.3: Floquet-Bloch band diagram of the tight-binding square-octagon lattice along the high-symmetry points of BZ. (a) Without any external perturbation for $t_2 = 1.0$. (b) In the presence of circularly polarized light when $t_2 = 1.0, \Omega = 7, A_0 = 0.8$. System clearly exhibits the CI phase for 1/4 filling and CSM phase for 1/2 filling as true band gap only exists between the two lower bands. (c) When $t_2 = 1.0, \Omega = 10, A_0 = 2.1$, the system exhibits the CI phase for both 1/2 and 3/4 fillings. True band gap exists between all the bands. (d) When $t_2 = 0.6, \Omega = 10, A_0 = 2.7$, CI and CSM phases appear for 1/2 and 3/4 fillings, respectively. Chern numbers of the respective energy-bands are noted. Density of states are also shown in the right panels. Horizontal dashed lines are drawn for the determination of true and pseudo band-gaps.

3.3 Derivation of Effective Hamiltonian by Floquet-Bloch Theory

In order to apply the Floquet-Bloch theory, the system is exposed to periodically driven monochromatic laser light which couples the momentum with the vector potential of the incident field $\mathbf{A} = \mathbf{A}_0 \left[\sin(\Omega t), \cos(\Omega t)\right]$ through the substitution $\mathbf{k} \to \mathbf{k} + \mathbf{A}(t)$. $\mathbf{A}_0$ and Ω are respectively amplitude and frequency of the laser light. Values of the relevant constants are assumed to be unity, so, $\hbar = 1, e = 1, c = 1$. Therefore, the time-dependent Hamiltonian looks like,

$$\begin{aligned} H(\mathbf{k}, t) = -t_1 \sum_{\mathbf{k}} \Big[& A_{\mathbf{k}}{}^{\dagger} B_{\mathbf{k}} e^{-i\mathbf{A}(t)\cdot\delta_2} + A_{\mathbf{k}}{}^{\dagger} D_{\mathbf{k}} e^{i\mathbf{A}(t)\cdot\delta_1} \\ & + B_{\mathbf{k}}{}^{\dagger} D_{\mathbf{k}} e^{-i\mathbf{k}\cdot\mathbf{R}(1,0)} e^{-i\mathbf{A}(t)\cdot\delta_4} + B_{\mathbf{k}}{}^{\dagger} C_{\mathbf{k}} e^{i\mathbf{A}(t)\cdot\delta_1} \\ & + A_{\mathbf{k}}{}^{\dagger} C_{\mathbf{k}} e^{i\mathbf{k}\cdot\mathbf{R}(0,1)} e^{i\mathbf{A}(t)\cdot\delta_3} + C_{\mathbf{k}}{}^{\dagger} D_{\mathbf{k}} e^{i\mathbf{A}(t)\cdot\delta_2} \Big] \\ & - t_2 \sum_{\mathbf{k}} \left[A_{\mathbf{k}}{}^{\dagger} C_{\mathbf{k}} e^{-i\mathbf{A}(t)\cdot\delta_5} + B_{\mathbf{k}}{}^{\dagger} D_{\mathbf{k}} e^{i\mathbf{A}(t)\cdot\delta_6} \right]. \end{aligned} \tag{3.4}$$

Now, the Hamiltonian becomes periodic with time period $T = 2\pi/\Omega$ like $H(\mathbf{k}, t) = H(\mathbf{k}, t + T)$ because of the periodicity of $\mathbf{A}(t)$ and monochromaticity of the laser light. This time-periodicity allows one to map the time-dependent problem into an effective time-independent problem by virtue of Floquet theory [25] as described below. By performing the Fourier transform in the time space, the periodic Hamiltonian can be expressed as

$$H(\mathbf{k}, t) = \sum_{p=-\infty}^{\infty} e^{ip\Omega t} H_p(\mathbf{k})$$

where $H_p(\mathbf{k}) = \frac{1}{T}\int_0^T e^{-ip\Omega t} H(\mathbf{k},t)\,dt = H^\dagger_{-p}(\mathbf{k})$ is the p-th order Fourier component. By considering the time-dependent Schrödinger equation for the system,

$$i\hbar \frac{d}{dt}\left|\psi(\mathbf{k},t)\right\rangle = H(\mathbf{k},t)\,\psi(\mathbf{k},t), \tag{3.5}$$

one may have the solution for the α-th band as

$$\psi_\alpha(\mathbf{k},t) = e^{i\epsilon_\alpha(\mathbf{k})t}\phi_\alpha(\mathbf{k},t), \tag{3.6}$$

where $\phi_\alpha(\mathbf{k},t)$ and $\epsilon_\alpha(\mathbf{k})$ are known as the time-periodic Floquet-Bloch wave function and Floquet quasi-energy of that band, respectively. Floquet-Bloch wave function can be expressed in the Fourier space as $\phi_\alpha(\mathbf{k},t) = \sum_{p=-\infty}^{\infty} e^{ip\Omega t}\phi_{\alpha,p}(\mathbf{k})$. Temporal periodicity of the Hamiltonian leads to the appearance of periodicity of the quasi-energies in the frequency space with period Ω, which, on the other hand, gives rise to the existence of quasi-energy BZ bounded within the limits $-\Omega/2 < \epsilon < \Omega/2$. This result is similar to the appearance of periodicity for the energy of Bloch electron in the momentum space.

By using Eqs (3.5, 3.6) and defining the Floquet operator as

$$H_F(\mathbf{k},t) = H(\mathbf{k},t) - i\partial_t$$

the following eigenvalue equation for the Floquet-Bloch wave function is obtained.

$$H_F(\mathbf{k},t)\left|\phi_\alpha(\mathbf{k},t)\right\rangle = \epsilon_\alpha(\mathbf{k})\left|\phi_\alpha(\mathbf{k},t)\right\rangle. \tag{3.7}$$

Solution of this equation in the Fourier space leads to a time-independent Floquet eigenvalue problem,

$$\sum_q \left[H_{p-q}(\mathbf{k}) + q\,\Omega\,\delta_{p,q}\right]\left|\phi_{\alpha,q}(\mathbf{k})\right\rangle = \epsilon_\alpha(\mathbf{k})\left|\phi_{\alpha,p}(\mathbf{k})\right\rangle. \tag{3.8}$$

Floquet theory finally leads to a set of infinite-dimensional coupled equations since both the Floquet numbers, p and q may assume any integral values in between $-\infty$ and $+\infty$. But, if the frequency of the incident light is greater than that of corresponding band-width of the system, the Floquet sub-bands become decoupled. In this limit, one can apply Floquet-Magnus expansion [26] to describe the system in terms of an effective Hamiltonian, H_{eff}, which can be written as $H_{\text{eff}} = \sum_i \frac{H^i_{\text{eff}}}{\Omega^i}$ where $H^0_{\text{eff}} = H^0$ and $H^1_{\text{eff}} = \sum_{p=1}^{\infty} \frac{1}{p} [H_p, H_{-p}]$. H_p is the p-th order Fourier component. Ignoring the higher order components ($|p| \geq 2$) for high frequency, H_{eff} is finally given by

$$H_{\text{eff}} = H_0 + \frac{1}{\Omega} [H_1, H_{-1}] . \tag{3.9}$$

Throughout this investigation, frequency of the light is kept greater than that of the band-width of the undriven system, *i.e.*, the system is always kept in the off-resonant regime. Although the electrons cannot be excited by direct absorption of this kind of irradiation, but instead the light is capable to modify the single-electron bands through virtual photon-absorption processes [27, 12]. In Eq. (3.9), H_0 describes the system where no photon exchange takes place, while H_1 (H_{-1}) takes into account the emission (absorption) of one virtual photon.

In order to obtain the expressions of H_0, H_1 and H_{-1}, for the construction of effective time-independent Hamiltonian H_{eff}, the Fourier components of severeal terms of $H(\mathbf{k}, t)$ (Eq. 3.4) have been derived. For example, the coefficient of a

particular term $-t_1 \sum_{\mathbf{k}} A^{\dagger}_{\mathbf{k}} B_{\mathbf{k}}$ is given by

$$\begin{aligned}
&\frac{1}{T}\int_0^T dt e^{-in\Omega t} e^{-\frac{iA_0}{\sqrt{2}}(\sin(\Omega t)+\cos(\Omega t)} \\
&= \frac{1}{T}\int_0^T dt e^{-in\Omega t} e^{-iA_0\sin(\Omega t+\pi/4)}, \\
&= \frac{1}{2\pi}\int_0^{2\pi} d\tau e^{-in\tau} e^{in\pi/4} e^{-iA_0\sin(\tau)}, \\
&= J_n(-A_0) e^{in\pi/4}, \qquad (3.10)
\end{aligned}$$

where $\tau = \Omega t + \pi/4$ and $\Omega T = 2\pi$. Similarly, the coefficient of $-t_1 \sum_{\mathbf{k}} B^{\dagger}_{\mathbf{k}} A_{\mathbf{k}}$ becomes $J_n(A_0)e^{in\pi/4}$. In the same way, all the other coefficients can be derived. The matrix elements of 4×4 matrix $H_n(\mathbf{k})$ are explicitly given by

$$\begin{aligned}
H_n^{12}(\mathbf{k}) &= t_1 J_n(-A_0) e^{in\pi/4}, \\
H_n^{21}(\mathbf{k}) &= t_1 J_n(A_0) e^{in\pi/4}, \\
H_n^{13}(\mathbf{k}) &= t_2 J_n(-\sqrt{2}A_0) e^{in\pi/2} + J_n(A_0) t_1 e^{i(n\pi/2+k_2}, \\
H_n^{31}(\mathbf{k}) &= t_2 J_n(\sqrt{2}A_0) e^{in\pi/2} + J_n(-A_0) t_1 e^{i(n\pi/2-k_2}, \\
H_n^{14}(\mathbf{k}) &= t_1 J_n(A_0) e^{-in\pi/4}, \\
H_n^{41}(\mathbf{k}) &= t_1 J_n(-A_0) e^{-in\pi/4}, \\
H_n^{23}(\mathbf{k}) &= t_1 J_n(A_0) e^{-in\pi/4}, \qquad (3.11) \\
H_n^{32}(\mathbf{k}) &= t_1 J_n(-A_0) e^{-in\pi/4}, \\
H_n^{24}(\mathbf{k}) &= t_2 J_n(\sqrt{2}A_0) + t_1 J_n(-A_0) e^{-ik_1}, \\
H_n^{42}(\mathbf{k}) &= t_2 J_n(-\sqrt{2}A_0) + t_1 J_n(A_0) e^{ik_1}, \\
H_n^{34}(\mathbf{k}) &= t_1 J_n(A_0) e^{in\pi/4}, \\
H_n^{43}(\mathbf{k}) &= t_1 J_n(-A_0) e^{in\pi/4},
\end{aligned}$$

Now, applying the relations $J_{-n}(A_0) = (-1)^n J_n(A_0)$ and $J_n(-A_0) =$

$(-1)^n J_n(A_0)$, matrix elements for the Fourier components of $H_0(\mathbf{k})$, $H_1(\mathbf{k})$ and $H_{-1}(\mathbf{k})$ have been obtained and finally, H_{eff} is obtained by using Eq. (3.9).

The diagonal elements of $H_{\text{eff}}(\mathbf{k})$ are zero. The off-diagonal upper-triangular elements of $H_{\text{eff}}(\mathbf{k})$ are written below.

$$
\begin{aligned}
H_{\text{eff}}^{12}(\mathbf{k}) &= J_0(A_0)t_1 - 4iPt_1t_2 + 2iQt_1^2(e^{ik_1} + e^{ik_2}),\\
H_{\text{eff}}^{13}(\mathbf{k}) &= J_0(\sqrt{2}A_0)t_2 + J_0(A_0)t_1e^{ik_2},\\
H_{\text{eff}}^{14}(\mathbf{k}) &= J_0(A_0)t_1 + 4iPt_1t_2 - 2iQt_1^2(e^{-ik_1} + e^{ik_2}),\\
H_{\text{eff}}^{23}(\mathbf{k}) &= J_0(A_0)t_1 - 4iPt_1t_2 + 2iQt_1^2(e^{-ik_1} + e^{ik_2}),\\
H_{\text{eff}}^{24}(\mathbf{k}) &= J_0(\sqrt{2}A_0)t_2 + J_0(A_0)t_1e^{-ik_1},\\
H_{\text{eff}}^{34}(\mathbf{k}) &= J_0(A_0)t_1 - 4iPt_1t_2 + 2iQt_1^2(e^{-ik_1} + e^{-ik_2}).
\end{aligned}
$$

$H_{\text{eff}}^{pq}(\mathbf{k})$ are the elements of p-th row and q-th column of the 4×4 Hamiltonian, $H_{\text{eff}}(\mathbf{k})$, where the constants P and Q are given by

$$
\begin{aligned}
P &= J_1(A_0)J_1(\sqrt{2}A_0)\sin(\pi/4)/\Omega,\\
Q &= {J_1}^2(A_0)\sin(\pi/4)/\Omega.
\end{aligned}
\tag{3.12}
$$

Here $J_n(x)$ is the n-th order Bessel function given by $J_n(x) = \frac{1}{2\pi}\int_0^{2\pi} e^{-i(n\tau - x\sin(\tau)}d\tau$.

It is evident that the circularly polarized light breaks the TRS of the undriven system since $H_{\text{eff}}(\mathbf{k}) \neq H_{\text{eff}}^*(-\mathbf{k})$. As soon as the periodic drive is turned on, *i.e.*, A_0 becomes non-zero, gaps appear in the band structure. At the same time, the system becomes topologically nontrivial in a sense that every band emerges with a definite value of Chern number. Band diagrams obtained by numerically diagonalizing the effective Hamiltonian $H_{\text{eff}}(\mathbf{k})$ are shown in Fig. 3.2 (b), (c) and (d) for few particular sets of parameter, t_2, A_0 and Ω. The Chern numbers of respective bands are also noted. The sets of parameters are chosen in such

a way that distribution of C for the four energy bands are different. In those figures, 'Energy' actually means the quasi-energies of the effective Hamiltonian since A_0 is non-zero. With the increase of A_0 beyond zero, both the flat-bands begin to become dispersive. At the same time, the remaining two bands get modified in such a fashion that a series of topological phase transitions occur, which will be described in detail in the next section. Dispersion relations along the path connecting the high-symmetry points of BZ are shown in Fig. 3.3 (b), (c) and (d).

The system exhibits true and pseudo gap in the band diagram for different parameter regimes and the corresponding topological phases are noted as CI and CSM [28], respectively, depending on the lattice fillings. True and pseudo band-gaps are defined in the following way. If $E_m(\mathbf{k}) \neq E_n(\mathbf{k}')$ for all $m \neq n$ and $\mathbf{k}$, $\mathbf{k}'$, then true gap exists between m and n-th energy bands. The gap is marked pseudo when $E_m(\mathbf{k}) \neq E_n(\mathbf{k})$ for all $m \neq n$ and $\mathbf{k}$. In the later case, $E_m(\mathbf{k}) = E_n(\mathbf{k}')$ is a possible scenario. For both the cases, Chern numbers are defined since the bands do not touch each other. The value of lattice filling determines the position of Fermi energy in the band diagram.

However, Figs 3.2(d) and 3.3(d) indeed reveal the occurrence of band inversion. This is due to the fact that dominant contribution to the band energy in the high-frequency regime is given by the term H_0. So, as A_0 crosses the value 2.4, the zeroth order Bessel function becomes negative, which is responsible for the inversion of the bands. The effect of linearly polarized light whose vector potential is given by $\mathbf{A} = A_0 [\sin(\Omega t), 0]$ is examined on the system. But the system remains trivial, which is similar to the outcome of previous investigation [15]. This is because of the fact that linearly polarized light fails to break the TRS of the system due to the combined effect of equal contribution and mutually compensating act of left and right circular states of polarization. However,

the energy bands are found to get modified and gaps emerge in the spectrum with the variation of both the parameters A_0 and t_2 in the presence of linearly polarized light.

3.4 Topological Properties

3.4.1 Chern numbers and Hall conductivity at zero temperature

The values of Chern numbers and Hall conductivity at zero temperature have been obtained in order to study the topological properties of the system by considering the effective time-independent Hamiltonian in off-resonant regime. Therefore, formalism developed for undriven system has been applied to obtain berry-curvature and zero-temperature Hall-conductivity, $\sigma_{H_{\text{eff}}}(E)$ [18]. $\sigma_{H_{\text{eff}}}(E)$ actually corresponds to the dc component of optical Hall conductivity in the Floquet theory [5, 15]. Here $\sigma_{H_{\text{eff}}}(E)$ is estimated numerically by using the Kubo formula (Eq. 1.7), When E falls in one of the band gaps, expression of $\sigma_{H_{\text{eff}}}$ is given by Eq. 1.16.

Here, C_n is the Chern number of n-th completely filled band, which is given by Eq. (1.6). In this numerical estimation, discretized version of Eq. 1.6 introduced before by Fukui and others has been used [29], as discussed earlier.

By keeping the frequency fixed at an off-resonant value, $\Omega = 10$, characteristics of topological phase transitions in the parameter space spanned by t_2 and A_0 have been investigated. Robustness of those results has been confirmed by fixing Ω to higher values. Now, the nature of phase transitions along two definite lines in the parameter-space will be described. First line is defined by fixing $t_2 = 1.0$. When A_0 is zero, Chern numbers are not defined for the lower three bands since

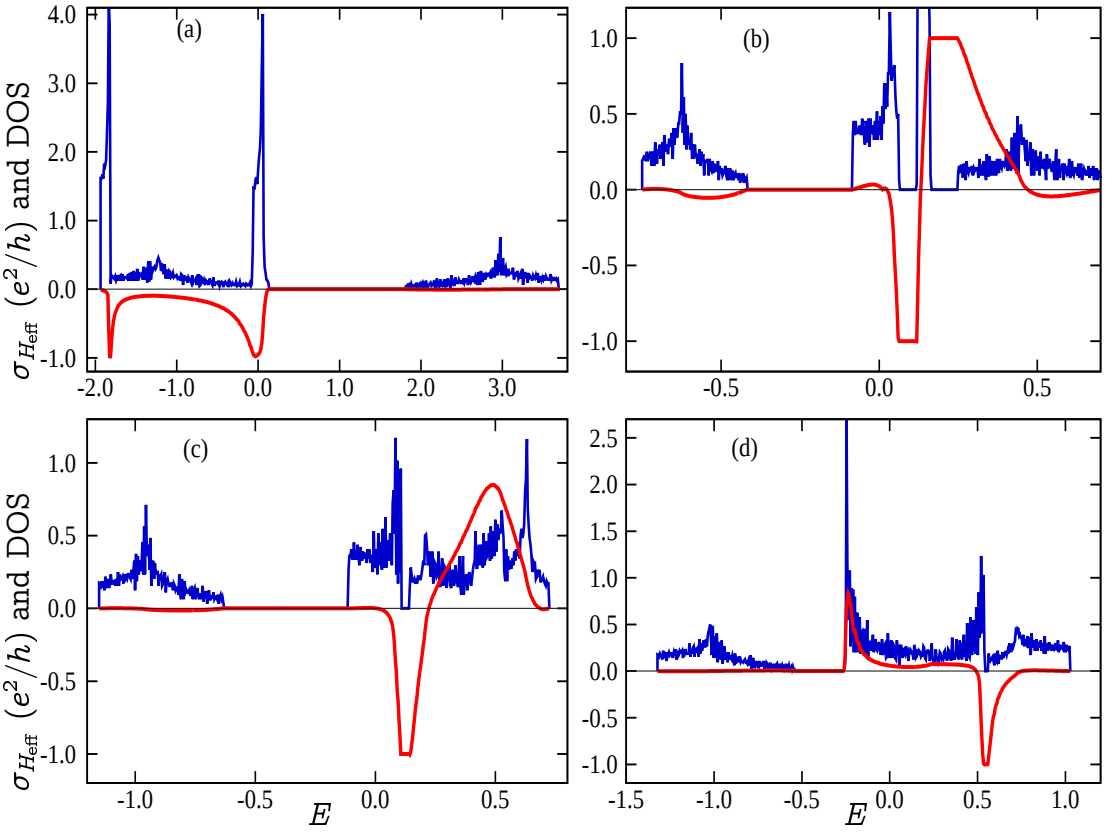

Figure 3.4: Topological phases in the presence of circularly polarized light with different A_0 when $t_2 = 1.0$, and $\Omega = 10$. (a) $A_0 = 0.5$ (b) $A_0 = 2.1$ (c) $A_0 = 3.0$ (d) $A_0 = 3.6$. The Hall conductance $\sigma_{H_{\rm eff}}$ (red line) and DOS (blue line) are plotted with respect to the Fermi energy, E.

there is no band gap. Value of C for the isolated upper band is found zero. For the line segment bounded by the limits $0.0 < A_0 \leq 1.2$, the system remains in a non-trivial topological phase with a definite value of C for each band. Here, $C = -1, 0, 1, 0$ for the bands arranged in the ascending order of energy. The system mostly remains in CSM phase for 1/2 and 1/4 lattice fillings.

From Fig. 3.4(a), it is observed that there are three plateaus for $\sigma_{H_{\rm eff}} = n(e^2/h)$ with $n = -1, -1, 0$. Plateaus are not always prominent due to the presence of either pseudo or narrow gaps in the band diagram. The density of states exhibits sharp peaks around the energies where $\sigma_{H_{\rm eff}}(E)$ undergoes sudden rise and fall.

It is worth mentioning that for infinitesimally small values of A_0, the original pair of flat bands develop very low curvature such that corresponding bandwidths are vanishingly small. At this limit, they acquire non-zero Chern numbers, $C = \pm 1$, but at the same time the band-gaps are too narrow to have a considerable value of flatness ratio.

With further increase of A_0 and when $1.2 < A_0 \leq 2.0$, a series of topological phase transitions is observed due to the rapid occurrence of intermediate band-touchings and gap-openings with the change of amplitude. A closer look reveals that gaps close and reopen when A_0 crosses 1.2 along with the emergence of a new topological phase with $C = 1, -2, 1, 0$. This is a quadratic band-touching point between the two lower bands as the Chern numbers of these bands are exchanged by ± 2 [6]. Upon further increase of A_0, a number of topological phases appear where the Chern numbers are redistributed consecutively as $(1, -2, 0, 1)$, $(-1, 0, 0, 1)$, $(-1, -1, 1, 1)$, $(0, -2, 1, 1)$, $(0, -2, 3, -1)$ and $(0, -1, 2, -1)$. The intermediate phase transitions are associated with the emergence of either Dirac or quadratic band touching points.

At $A_0 = 2.1$, the system again exhibits true band-gaps where the Chern numbers of the bands are $(0, -1, 2, -1)$. The corresponding figure (Fig. 3.4(b)) shows that there are three prominent plateaus in $\sigma_{H_{\text{eff}}} = n(e^2/h)$ with $n = 0, -1, 1$. The system remains in CI phase for $1/2$ and $1/4$ lattice fillings. When A_0 is increased to 2.12, a new topological phase with $C = 0, 1, 1, -2$ appears. At the subsequent transition point, the gap between middle two bands closes. Dispersion relations of the two bands are linear at the touching point. with slight increase of A_0, that gap reopens and the Chern numbers of those two middle bands are exchanged by ± 1 leading to a new topological phase with $C = 0, 0, 2, -2$.

At the points $A_0 = 2.4$ and 2.5, the system drives into the trivial phase

since all the Chern numbers become zero. This happens because of the fact that around those points, the value of zeroth order Bessel function becomes vanishingly small. When A_0 reaches to the value 2.6, the Chern numbers are restored to $(0, 0, 2, -2)$. The system again undergoes a series of rapid phase transitions with further modulation of A_0. Two different phases with $C = 0, -1, 2, -1$ at $A_0 = 3.0$ and $C = 0, 1, -2, 1$ at $A_0 = 3.6$ are shown in Fig. 3.4 (c) and (d), respectively. For $A_0 = 3.0$, the plateau at $n = -1$ is prominent as the system lies in CI phase for $1/2$ lattice filling. Elsewhere, the system remains in CSM phase.

Another series of phase transitions can be obtained if the parameter space is explored along a different line by fixing $A_0 = 2.1$. When $0 \leq t_2 \leq 0.2$, the system is in Chern insulating phase for all values of lattice fillings with $C = -1, -1, 1, 1$. Then the gap between the lower two bands closes and reopens to redistribute the Chern numbers as $(0, -2, 1, 1)$ at $t_2 = 0.3$. For $0.4 < t_2 < 0.5$, a phase $C = 0, -2, 3, -1$ appears due to quadratic closing of lower two bands. Then, we obtain fully gapped CI phase with $(0, -1, 2, -1)$ for $0.5 \leq t_2 \leq 1.1$. Thereafter, the system undergoes rapid transitions through the phases $(0, 1, 0, -1), (0, 1, 1, -2), (0, 0, 2, -2)$. Those can be identified as CSM phase because the system demonstrates several pseudo-gaps in its band diagram. For $t_2 > 1.5$, system becomes trivial as all the Chern numbers become zero.

Variation of topological phases as well as distribution of C for respective phases with the change of A_0 and t_2 are shown in Figs 3.5 (a) and (b), respectively. Rate of variation of phases with respect to A_0 is faster. Maximum value of C is $+3$ while minimum value of that is -2. Extent of phases is uneven and appearance of them is quite random. Multiple topological phases and rapid variations of them are the two special findings in this model.

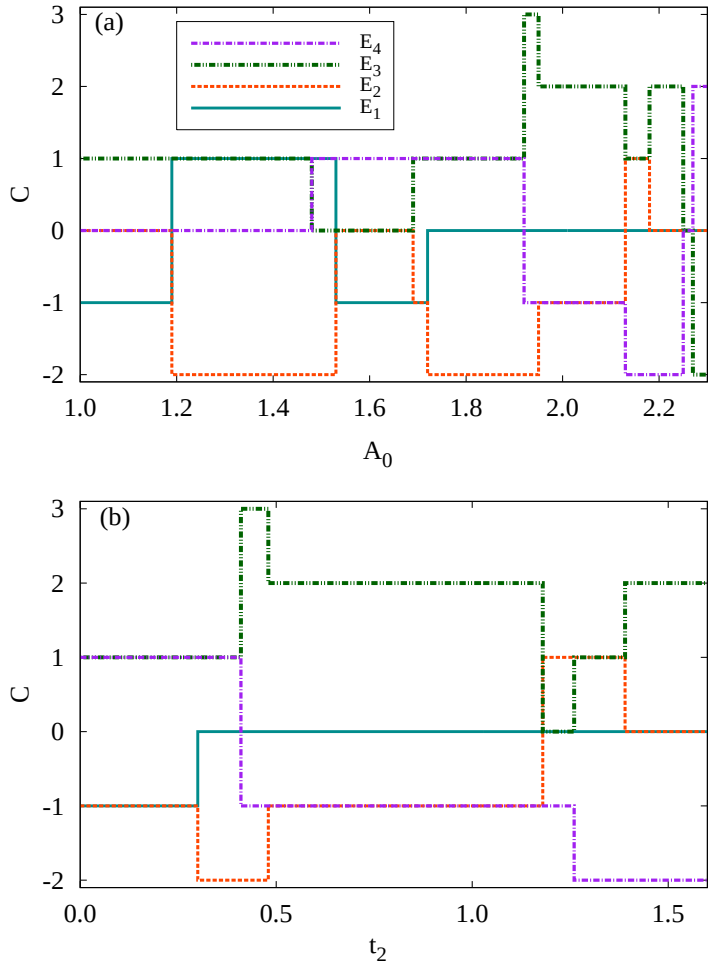

Figure 3.5: (a) Topological phase diagram of the system shows rapid variation of phases with A_0, where t_2 and Ω are fixed at 1.0 and 10.0, respectively. Chern numbers of the four bands are plotted as a function of A_0. (b) Topological phase diagram of the system with respect to t_2. A_0 and Ω are fixed at 2.1 and 10.0, respectively. Summation of the Chern numbers over all the bands are zero, which is evident from the figures.

3.4.2 Topological edge states

In order to examine whether the system obeys the BBC rule, the effective Hamiltonian of a finite strip of the system is considered. Values of the parameter are taken as $t_2 = 1.0, A_0 = 2.1, \Omega = 10$. The system remains in a particular CI phase for these values. To create edges in the system, periodic boundary condition along $\boldsymbol{a}_2$ direction is withdrawn, so that k_2 is no longer a good quantum

number. Now, considering $N = 50$ unit cells *i.e.* 200 sites along a_2 direction, the resulting $4N \times 4N$ Hamiltonian is diagonalized. The quasi-energy eigenvalues of the effective Hamiltonian are plotted as a function of k_1 in Fig. 3.6. Density of states are also drawn in the side-panel to show that the spectrum has a true gap.

Evidently, additional states are found to appear within the band gaps, those actually connect the distinct bulk bands. These are known as the edge states, which are indeed localized in either left (blue curves) or right (red curves) edge of the finite lattice, as shown in the lower panel of Fig. 3.6. It may be noted that the edge states are chiral in nature since the right-going states or the states with positive group velocity are localized in the right edge, and similarly, the left-going states with negative group velocity are always localized in the left edge.

Hence, the results are in accordance with the BBC rule which states that: sum of the Chern numbers up to the i-th band, $\nu_i = \sum_{j \leq i} C_j$ is equal to the number of pair of edge states in the gap [30]. It can be verified from the fact that the Chern numbers of the corresponding bands are $-1, 2, -1$ in the ascending order of energy as shown in Fig. 3.6. So, there must be one pair of edge states in each band gap.

3.5 Summary and Discussion

The effect of circularly polarized light on the topology and band-structure of square-octagon lattice is studied by using the Floquet-Bloch theory. The system is topologically trivial in the absence of light with a pair of flat bands and quadratic band-touching points in its band-diagram. As soon as the system is exposed to circularly polarized light, flat bands become dispersive and the

system is driven into non-trivial topological phase at the same time. Photo induced band structure exhibits true and pseudo gaps depending on the amplitude of light which eventually leads to the emergence of multiple topological phases with a variety of Chern number distribution. Thus a series of topological phase transitions is observed with the modulation of amplitude of the incident light and hopping strengths. The overall state of the system is identified either CSM or CI phase depending on the value of lattice filling. Those phases are topologically robust in a sense that no further change is observed with the variation of frequency as long as it is fixed in off-resonant regime. The frequency is always kept higher than the band-width of the undriven system to make sure that Floquet-Magnus expansion is always valid. Topological properties are characterized in terms of Chern numbers of distinct energy bands which is further justified with the behaviour of Hall conductance and evidence of edge states. Linearly polarized light has no effect on the topological properties of the system as it fails to break the TRS.

Previous investigation reveals that Dirac cones appear at the Γ and M points in the absence of NNN hopping [23]. The present study indicates that the system exhibits photo-induced CI phase in this case, for any values of lattice filling. So, it would be interesting to find the photo-induced topological properties of a particular model with different values of hopping strengths for intra- and inter-square-plaquette NN bonds on the square-octagon lattice. In this context, computation of finite-frequency optical conductivity will become useful for the experimental detection of topological phases. Additionally, further expansion of this work can be made by invoking further neighbour hoppings in this tight-binding model.

FTI phase has been observed on graphene with the help of opto-helical waveguides [31] and Floquet-Bloch bands have been found on the surface of the

compound, Bi_2Se_3 [32]. In another development, optical lattices with ultracold atoms for two-dimensional honeycomb [33], checkerboard [34] and kagomé [35] structures have been realized. So, the square-octagon optical lattice will hopefully become realizable in near future which, on the other hand, will pave the way for observation of these topological phases. However, square-octagon lattice based on real material had been come to light long ago in the context of antiferromagnetic compound, CaV_4O_9 [36]. The spin-1/2 V^{4+} ions in this spin-liquid constitute square-octagon lattice structure. Meanwhile, quasi square-octagon structure has been found in $(10\bar{1}0)$ surface of functional material ZnO [37]. So, the recent trends of investigation indicate the realization of these findings very soon.

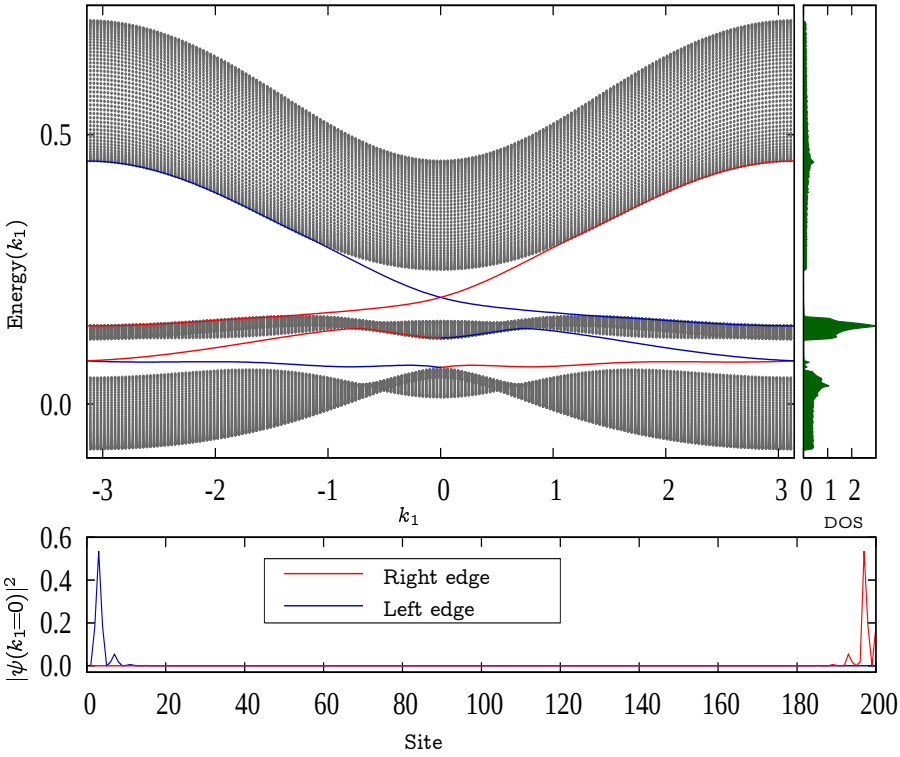

Figure 3.6: Edge states of square-octagon lattice in the presence of circularly polarized light for the parameters $t_2 = 1.0, \Omega = 10, A_0 = 2.1$ for $N = 50$ unit cell along k_2. Chern numbers of the upper three bands are $C = -1, 2, -1$. The lowest band with $C = 0$ is not shown in figure since the lowest band-gap does not accommodate any edge states. The side-panel indicates the density of states. Lower panel shows the probability density of left (blue) and right (red) going edge states with respect to site number of the strip for $k_1 = 0$. The colour of the edge state energies corresponds to the colour of particular edge where the probability density is concentrated.

Bibliography

[1] Oka T. and Aoki H., Phys. Rev. B **79**, 081406 (2009).

[2] Inoue J., Phys. Rev. B **81**, 125412 (2010).

[3] Kitagawa T., Berg E., Rudner M. and Demler E., Phys. Rev. B **82**, 235114 (2010).

[4] Inoue J. and Tanaka A., Phys. Rev. Lett. **105**, 017401 (2010).

[5] Dehghani H., Oka T. and Mitra A., Phys. Rev. B **91**, 155422 (2015).

[6] Kundu A., Fertig H. A. and Seradjeh B., Phys. Rev. Lett. **113**, 236803 (2014).

[7] D'Alessio L. and Rigol M., Nature Communications **6**, 8336 (2015).

[8] Perez-Piskunow P. M., Usaj G., Balseiro C. A. and Torres L. E. F. F., Phys. Rev. B **89**, 121401(R) (2014).

[9] Li S., Liu C. C. and Yao Y., New J. Phys. **20** 033025 (2018).

[10] Saha K., Phys. Rev. B **94**, 081103(R) (2016).

[11] Lindner N., Refael G. and Gaslitski V., Nat. Phys. **7**, 490 (2011).

[12] Ezawa M., Phys. Rev. Lett. **110**, 026603 (2013).

[13] Gomez-Leon A. and Platero G., Phys. Rev. Lett. **110**, 200403 (2013).

[14] Cayssol J., Dora B., Simon F. and Moessner R., Physica Status Solidi (RRL) 7, 101 (2013).

[15] Du L., Zhou X., and Fiete G. A., Phys. Rev. B **95**, 035136 (2017).

[16] Long Y. and Ren J., arXiv: 1706.01107.

[17] Rudner M. S., Lindner N. H., Berg E., and Levin M., Phys. Rev. X **3**, 031005 (2013).

[18] Owerre S. A., J. Phys. Commun. **1**, 021002 (2017).

[19] Kargarian M. and Fiete G. A., Phys. Rev. B **82**, 085106 (2010).

[20] Pal B., Phys. Rev. B. **98**, 245116 (2018).

[21] Liu X. P., Chen W. C., Wang Y. F. and Gong C. D., J. Phys.: Condens. Matter **25**, 305602 (2013).

[22] Yang Y., Yang J., Li X. and Zhao Y., Physics Letters A **382**, 723âĂŞ728 (2018).

[23] Yamashita Y., Tomura M., Yanagi Y. and Ueda K., Phys. Rev. B **88**, 195104 (2013).

[24] Yu U., Phys. Rev. E **91**, 062121 (2015).

[25] Floquet G., Ann. Sci. Ec. Normale Super. **12**, 47 (1883).

[26] Bukova M., D'Alessio L. and Polkovnikov A., Adv. Phys. **64**, 139 (2015).

[27] Kitagawa T., Oka T., Brataas A., Fu L. and Demler E., Phys. Rev. B **84**, 235108 (2011).

[28] Palumbo G. and Meichanetzidis K., Phys. Rev. B. **92**, 235106 (2015).

[29] Fukui T., Hatsugai Y. and Suzuki H., Journal of the Physical Society of Japan **74**, 1674 (2005).

[30] Mook A., Henk J. and Mertig I., Phys. Rev. B. **90**, 024412 (2014).

[31] Rechtsman M. C., Zeuner J. M., Plotnik Y., Lumer Y., Podolsky D., Dreisow F., Nolte S., Segev M. and Szameit A., Nature **496**, 196 (2013).

[32] Wang Y. H., Steinberg H., Herrero P. J. and Gedik N., Science **342**, 453 (2013).

[33] Soltan-Panahi P., Struck J., Hauke P., Bick A., Plenkers W., Meineke G., Becker C., Windpassinger P., Lewenstein M. and Sengstock K., Nat. Phys. **7**, 434 (2011).

[34] Wirth G., Olschlager M. and Hemmerich A., Nature Phys. **7**, 147 (2010).

[35] Jo G. B., Guzman J., Thomas C. K., Hosur P., Vishwanath A. and Stamper-Kurn D. M., Phys. Rev. Lett. **108**, 045305 (2012).

[36] Taniguchi S., Nishikawa T., Yasui Y., Kobayashi Y., Sato M., Nishioka T., Kontani M. and Sano K., J. Phys. Soc. Jpn. **64**, 2758 (1995).

[37] He M. R., Yu R., Zhu J., Angew. Chem. **124**, 78 (2012).

Chapter 4

First and Second Order Topology on Breathing Kagome Lattice

4.1 Overview

The concept of higher order TI's [1, 2, 3, 4, 5, 6] has been introduced where a d dimensional n-th order TI shows $(d–n)$ dimensional boundary states contrary to the conventional or first order TI's when $n = 1$. For instance, a two-dimensional second order TI will show zero-dimensional corner states but will not show one-dimensional gapless edge states [7, 8, 9, 10, 11, 12, 13, 14, 15]. In those HOTI's, the conventional BBC rule may not be applicable. Obviously, different types of topological invariants like polarization [7], Z_Q Berry phase [9, 16], nested Wilson loop [2], mirror Chern number [8] etc have been introduced depending on the symmetry of the system to characterize the topological property of the bulk. Origin of lower dimensional edge states can be attributed to quantization of dipole or quadrupole moment as observed in two-dimensional phononic and electric quadrupole topological insulators [1, 17, 18].

In recent times, besides electronic TI, topological magnon insulators (TMI)

[19] are being studied, where the quasiparticle excitation (magnon) is bosonic in nature. It has been known that the topological nature of a system is independent of the statistics of the quasiparticles. Topological magnons are found before in honeycomb lattice [20, 21], kagome lattice [22, 19], Lieb lattice [23], etc. Those topological phases have been experimentally observed in kagome ferromagnets, $Lu_2V_2O_7$ [24, 25], Cu[1,3-benzenedicarboxylate (bdc)] [26], and honeycomb ferromagnet, CrI_3 [27]. Topological magnons give rise to thermal magnon Hall effect (MHE), in which a temperature gradient transports a dissipationless heat current which has been verified experimentally [28]. Generally, in those spin systems, ferromagnetic Heisenberg model is considered where DMI is incorporated to trigger non-zero berry curvature. Spin models without DMI have also been shown to possess non-trivial topology. For example, FM Heisenberg models with Kitaev and spin-anisotropic interactions (HKSA) are found to host a number of topological phases [29, 30]. Thus, topological magnons have promising applications in the field of dissipationless spin transport, magnon spintronics and magnetic data storage.

On the other hand, HOTI's have been studied so far in fermionic systems in terms of tight-binding models on square and cubic lattice [1, 2, 3, 6], breathing kagome [7, 31], photonic systems [14, 32], non-Hermitian systems [11], etc. In addition, Kitaev model on Shastry-Sutherland lattice and magnetic vortex model on kagome lattice exhibit HOTI phases [12, 13]. Higher order topological Mott insulating phase has been demonstrated in a Hubbard model on the kagome lattice, where the topological state is characterized by Z_3 spin-Berry phase [33]. Besides, second order topological insulators (SOTI) have been experimentally realized using quantized dipole or quadrupole polarization [17, 18] and implemented in mechanical systems [17], electrical circuits [34], microwave systems [35], photonic [36] and phononic crystals [31]. However, no report on

higher order topological phase in the FM Heisenberg systems is available till date.

In this work, we focus on the realization of second order topological magnon insulating (SOTMI) phase in a spin system with and without DMI. Here, FM Heisenberg model is formulated on the breathing kagome lattice in the presence of DMI along the NN bonds. The system reveals the existence of simultaneous first and second order TMI phases in different parameter regimes when DMI is non-zero. When DMI is zero, only second order TMI can be realized as the Chern number (C), the first order topological invariant, is always zero for all the bands. In other case, polarization is used as the bulk topological index to characterize the HOTI phase due to the mirror symmetry of the system [7]. So, polarization plays the crucial role to distinguish between the nontrivial and trivial SOTI phase in the same way C distinguishes between the nontrivial and trivial TMI phases in case of first order. One dimensional gapless edge states are found for nontrivial TI phase, while gapped edge states along with zero dimensional corner states are found for nontrivial SOTMI phase. For certain values of DMI strength, both type of phases are found to exist simultaneously. Transition between different topological phases are shown in the parameter-space. In addition, thermal Hall conductivity is calculated for all the TMI phases.

The chapter is organized in the following way. In section 4.2, breathing kagome lattice is described and the linear spin-wave Hamiltonian is formulated. We describe the topological phases for zero DMI strength in the following section 4.3. Topological phases for non-zero DMI strength are explained in the subsequent section 4.4. The values of thermal Hall conductivities are available in section 4.5. Finally, section 4.6 contains the discussion along with the summary of the results.

4.2 Formulation of Heisenberg Hamiltonian with DM Interaction

A FM Heisenberg Hamiltonian is formulated on the breathing kagome lattice with DMI along NN bonds. Breathing kagome lattice is composed of three identical triangular sublattices. As a result, the unit cell comprises of three sites A, B and C forming a downward triangle (Fig. 4.1). The spin operators on those three sites are denoted by $\mathbf{S_n^a}, \mathbf{S_n^b}$ and $\mathbf{S_n^c}$, respectively. The coordinates of a unit cell are denoted by $\mathbf{n} = (n_1, n_2)$. So, the Hamiltonian of this system can be written as

$$H = H_{\text{NN}} + H_{\text{mag}} + H_{\text{DM}}, \tag{4.1}$$

where

$$\begin{aligned} H_{\text{NN}} &= -J_\alpha \sum_{\langle n,n' \rangle} \left(\mathbf{S_n^a} \cdot \mathbf{S_{n'}^b} + \mathbf{S_n^b} \cdot \mathbf{S_{n'}^c} + \mathbf{S_n^c} \cdot \mathbf{S_{n'}^a} \right), \\ H_{\text{mag}} &= -h \sum_n \left(S_n^{az} + S_n^{bz} + S_n^{cz} \right), \\ H_{\text{DM}} &= -D_\alpha \sum_{\langle n,n' \rangle} \left(\mathbf{S_n^a} \times \mathbf{S_{n'}^b} + \mathbf{S_n^b} \times \mathbf{S_{n'}^c} + \mathbf{S_n^c} \times \mathbf{S_{n'}^a} \right) \cdot \hat{z}. \end{aligned}$$

J_α, $\alpha = 1\,(2)$ is the NN exchange interaction strength between upward (downward) triangles and D_α, $\alpha = 1\,(2)$ is the DMI strength, pointing towards z $(-z)$ direction, between upward (downward) triangles. $\langle \cdot \rangle$ denotes the summations over NN pairs. Considering the FM case, we fix $J_\alpha > 0$ throughout this chapter. $h = g\mu_B \mathcal{H}$, where $\mathcal{H}$ is the strength of the external magnetic field along z direction, which helps to align the localized spins ferromagnetically along z direction when h is assumed greater than zero.

Now, based on the classical ground state in which all the spins point along

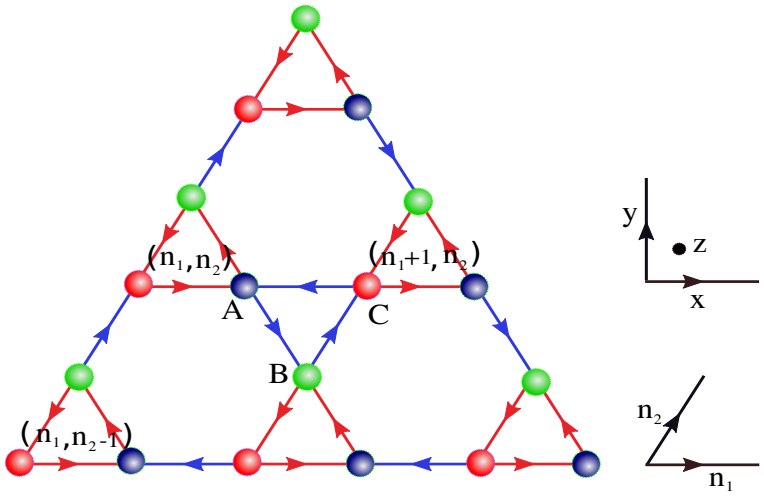

Figure 4.1: A triangular replica of breathing kagome lattice is shown. Three sites A, B and C are denoted by green, blue and red spheres, respectively. The notation of the unit cells is also shown. The Heisenberg interaction strength is J_1 for the red lines (upward triangles) and J_2 for the blue lines (downward triangles). Considering DMI along z direction, coupling strength of two sites along the arrow will be $J_1\,(J_2) + iD_1\,(D_2)$ and opposite to the arrow will be $J_1\,(J_2) - iD_1\,(D_2)$. The lattice vectors, $\mathbf{n_1} = (1, 0), \mathbf{n_2} = (1/2, \sqrt{3}/2)$ are shown in the side diagram.

the $+z$ direction, we obtain FM magnon dispersion relation by expressing the spin operators, $\mathbf{S}^{\eta}_{\mathbf{n}}$, in terms of bosonic creation ($\eta^{\dagger}$) and annihilation operators (η) by using the standard Holstein-Primakoff (HP) transformation:

$$S^{\eta z}_{\mathbf{n}} = S - \eta^{\dagger}_{\mathbf{n}}\eta_{\mathbf{n}},\; S^{\eta +}_{\mathbf{n}} \simeq \sqrt{2S}\,\eta_{\mathbf{n}},\; S^{\eta -}_{\mathbf{n}} \simeq \sqrt{2S}\,\eta^{\dagger}_{\mathbf{n}},$$

where $\eta = a, b$ and c for the respective sublattices A, B and C. $S^{\eta \pm}_{\mathbf{n}} = S^{\eta x}_{\mathbf{n}} \pm i S^{\eta y}_{\mathbf{n}}$. Now, following linear spin wave theory (LSWT) and using Fourier transformation of the operators in the form $\eta_{\mathbf{n}} = \frac{1}{\sqrt{N}} \sum_{\mathbf{k}} \eta_{\mathbf{k}} e^{i\mathbf{k}\cdot\mathbf{n}}$ (N is the total number of unit cells in the lattice), the Hamiltonian in the momentum space can be written as

$$H = E_0 + H_{SW}, \tag{4.2}$$

where $E_0 = -h\sum_n S - 3(J_1+J_2)\sum_{\langle n,n'\rangle} S^2$, is the classical ground state energy. H_{SW} can be written as (retaining terms only up to second order in bosonic operators)

$$H_{SW} = S\sum_k \psi_k{}^\dagger \mathcal{M}(\mathbf{k})\psi_k, \tag{4.3}$$

where $\mathbf{k} = (k_x, k_y)$, $\psi_\mathbf{k} = (c_\mathbf{k}, a_\mathbf{k}, b_\mathbf{k})$ and $\mathcal{M}(\mathbf{k})$ is a 3×3 matrix which is given by

$$\mathcal{M}(\mathbf{k}) = \begin{pmatrix} m_{11} & m_{12} & m_{13} \\ m_{12}^* & m_{22} & m_{23} \\ m_{13}^* & m_{23}^* & m_{33} \end{pmatrix}, \tag{4.4}$$

with the components, m_{ij}, given by

$$\begin{aligned} m_{11} &= m_{22} = m_{33} = 2(J_1+J_2) + h/S, \\ m_{12} &= -(J_1 + iD_1) - (J_2 + iD_2)e^{-ik_1}, \\ m_{13} &= -(J_1 - iD_1) - (J_2 - iD_2)e^{-ik_2}, \\ m_{23} &= -(J_1 + iD_1) - (J_2 + iD_2)e^{i(k_1-k_2)}, \end{aligned} \tag{4.5}$$

where $k_1 = \mathbf{k}\cdot\mathbf{n_1} = k_x$ and $k_2 = \mathbf{k}\cdot\mathbf{n_2} = k_x/2 + \sqrt{3}k_y/2$. Magnetic field only appears in each of the diagonal terms of $\mathcal{M}(\mathbf{k})$ with a fixed value, h/S, which means that topological properties of this system are totally insensitive to the value of $\mathcal{H}$. We have assumed a very small positive value of h only to ensure the FM ground state. As the Hamiltonian H_{SW} is number conserving, the magnon dispersion relation can be obtained by diagonalizing it. The results are valid for any value of S, while accuracy increases with the magnitude of S.

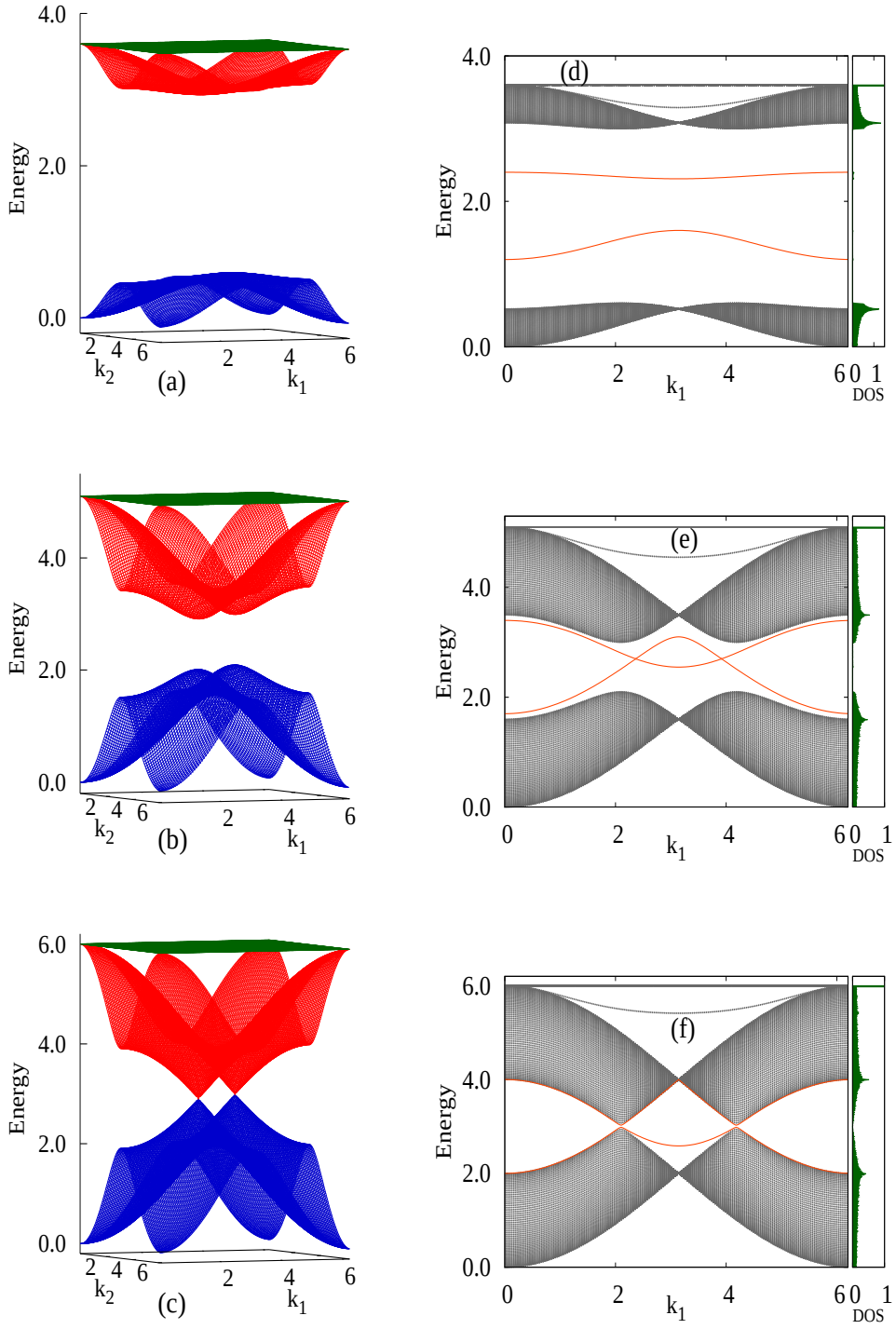

Figure 4.2: Dispersion relation of breathing kagome system for zero DMI strength with $J_2 = 1$ and (a)$J_1 = 0.2$, (b)$J_1 = 0.7$, (c)$J_1 = 1.0$. Edge state diagram for finite lattice with 70 unit cells along k_2 direction with same parameter values as the corresponding bulk band structures in the left column. The diagrams (d), (e) and (f) show the evolution of the in-gap edge modes (indicated by red lines).

4.3 Topological properties with zero DMI

While kagome ferromagnet ($J_1 = J_2$) is topologically trivial in the absence of DMI, FM breathing kagome ($J_1 \neq J_2$) with zero DMI is found nontrivial. In this section, topological nature of the system will be discussed by studying both bulk and boundary properties of it in terms of suitable topological invariants to characterize them. Henceforth, the value of J_2 is fixed at unity while exploring the variation of topological phases with respect to the parameter J_1. Three sets of bulk dispersion relation are shown in Fig. 4.2 (a), (b) and (c), where $J_1 = 0.2$ for the region $0.0 < J_1 < 0.5$, $J_1 = 0.7$ for the region $0.5 < J_1 < 1.0$, and $J_1 = 1.0$, respectively. Note that the uppermost band is always flat and it touches the lower band at four corners of the Brillouin zone spanned by (k_1, k_2), which are essentially the equivalent points. At this moment, the system is an insulator at 1/3 filling as the lower two bands are separated. The gap decreases with the increase of J_1 and vanishes at $J_1 = 1.0$. The gap again opens up for $J_1 > 1.0$.

Beside the bulk spectrum, we present the band structure of the corresponding finite strip of the system for every case. They are shown in Fig. 4.2 (d), (e) and (f) and depict the way how the evolution of in-gap edge modes affect the existence of corner states of the system. The finite strip is prepared by breaking the periodic boundary condition along the k_2 direction. In the region, $0.0 < J_1 < 0.5$, two gapped edge modes are found to exist between the lower two gapped bands, which do not decay into the bulk anymore. These are the signature of corner states, as proved in the previous studies [7, 8]. For $0.5 < J_1 < 1.0$, two edge modes are found to cross each other twice, without decaying into the bulk again. For $J_1 \geq 1.0$, there are no such edge modes. From this edge state spectrum, it is confirmed that the system is topologically trivial in first order

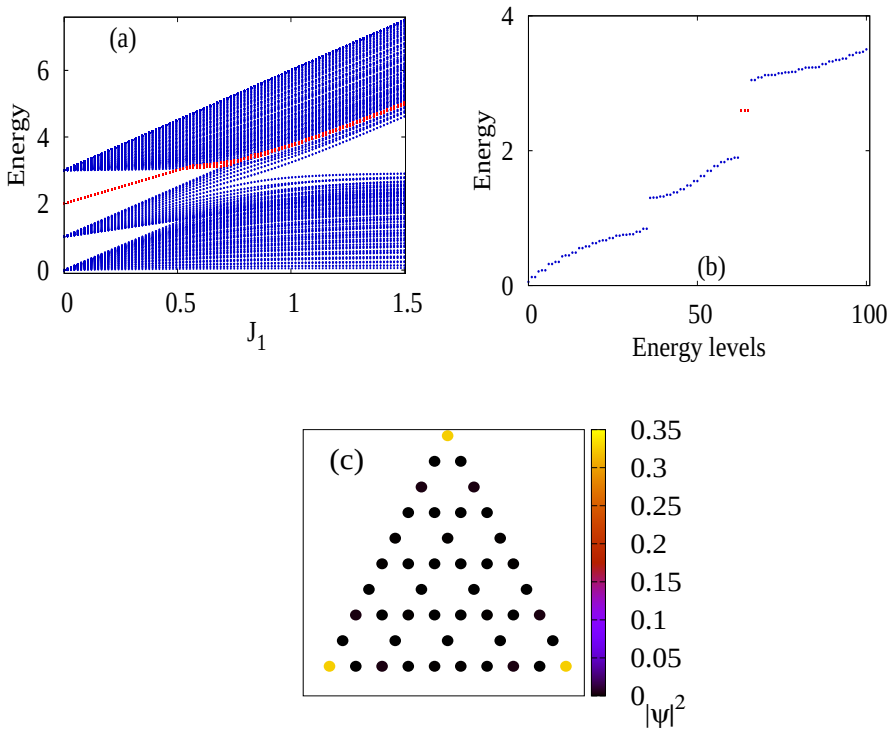

Figure 4.3: (a) Energy spectrum of breathing kagome lattice with varying J_1 for $L = 15$. Upto $J_1 = 0.5$, zero dimensional corner states (indicated by red dots) show its existence and beyond this value, it seems to decay into the bulk. (b) Energy of the same system is plotted with respect to energy levels for $J_1 = 0.3$. Three red dots at same energy, $E = 2.6$ show the states at the three corners of the finite triangle. The diagram is truncated to 100 energy levels (instead of 164 for $L = 10$) for better resolution of the three corner states. (c) Probability distribution of a particular eigenstate corresponding to a corner state energy for $J_1 = 0.2$ and $L = 5$. It shows that the states are indeed localized at the corners.

since there is no gap between the upper two bands in the region $0.0 < J_1 < 1.0$. Instead, the system is found to host a nontrivial second order topological phase in the above region.

For the characterization of topological phases, bulk topological invariant has been formulated by following the procedure developed in the article [7]. In this formulation, a particular quantity, polarization along the n_i axis is defined by

$$p_i = \frac{1}{S} \iint_{1\mathrm{BZ}} d^2\mathbf{k} A_i, \tag{4.6}$$

where $A_i = -i\langle\psi|\partial_{k_i}|\psi\rangle$ is the Berry connection with $i = 1, 2$ and $S = 4\pi^2$ being the area of the first Brillouin zone spanned by k_1 and k_2. The set of polarization $(p_1,\, p_2)$ is identical to the coordinates of the Wannier center [7]. The distance of the Wannier center from the origin can be taken as the bulk topological invariant as it changes its value only if the gap closes. For simplicity, we take p_1 as the topological index as it is protected by the mirror symmetry along the n_1 axis and it is also quantized. As we will see, it is non-zero in the topological phase and zero in trivial phase. It can be calculated analytically in extreme cases when either $J_1 = 0, J_2 \neq 0$, $(p_1 = 1/3)$ or $J_2 = 0, J_1 \neq 0$, $(p_1 = 0)$ as for the characterization of topological and trivial phases, respectively. For example, when $J_1 = 0, J_2 \neq 0$ the exact ground state wave function turns out to be $\psi = (1, e^{ik_1}, -e^{ik_2})^T/\sqrt{3}$. So, the Berry connection, A_1, as well as polarization, p_1, becomes equal to the value $1/3$, following the formula 4.6.

Values of p_i have been obtained numerically for every non-zero value of J_1, J_2 and DMI strength. To evaluate the integral, Eq. 4.6, we discretize the Brillouin zone and redefine p_i as p_{in} (n being the band index) and A_i as $A_{in} = -i\langle\psi_{n\mathbf{k}}|\partial_{k_i}|\psi_{n\mathbf{k}}\rangle$. The value of p_{1n} has been calculated for every band, n. In this case, as the gapped edge states exist between the lower two bands, p_1 should have a quantized value for the lowest band. Numerical evaluation obtains the value of $p_1 = 1/3$ for $0.0 < J_1 < 1.0$, and $p_1 = 0$ for $J_1 > 1.0$, for the lowest band. Hence, the non-zero value of topological invariant confirms the nontrivial second order topological phase of the system for the region mentioned above.

In order to investigate the existence of corner states in this system, we consider a triangular replica of the breathing kagome lattice, as shown in Fig. 4.1, whose size is defined by the number of small triangles, L, along every edge. The triangular replica preserves the three-fold rotation symmetry, C_3, of the breathing kagome lattice as well as it has the minimum number of corners, which is

three in this case. Different shapes of the finite lattice can be considered for this purpose. In Fig. 4.3 (a), we plot the energy spectrum as a function of J_1 for $L = 15$, which shows that corner states do exist for the region $0.0 < J_1 < 0.5$.

The numerical evaluation of the topological index p_1 shows that it bears the value $1/3$ for the entire region $0.0 < J_1 < 1.0$, which indeed should be the case as the insulating phase exists up to $J_1 = 1.0$ and the invariant has no scope to change its value since no phase transition occurs in the intermediate point. On the other hand, corner states cease to show its existence as soon as the gapped edge modes are found to cross each other. And it occurs in this system, when J_1 becomes greater than 0.5, which is illustrated in Fig. 4.2 (e). As a result, no corner states are found beyond $J_1 = 0.5$. But, the system hosts the second order topological phase in the entire region $0.0 < J_1 < 1.0$, even though the corner states are topologically protected only up to $J_1 = 0.5$. It implies that bulk-corner-correspondence is satisfied for the region $0.0 < J_1 < 0.5$, and violated for the region $0.5 \leq J_1 < 1.0$. However, the system becomes trivial beyond the limit, $J_1 = 1.0$. In Fig. 4.3 (b), the energy spectrum is plotted with respect to the energy levels for a particular value of J_1, which clearly shows the existence of three degenerate corner states at energy $2.6J_2$ which correspond to the three different corners of the triangular replica. The number of corner states may vary with the shape of replica with different number of corners. The distribution of probability density for a particular parameter value in this topological phase is shown in Fig. 4.3 (c), which clearly exhibits that the corner states are truly localized at each corner.

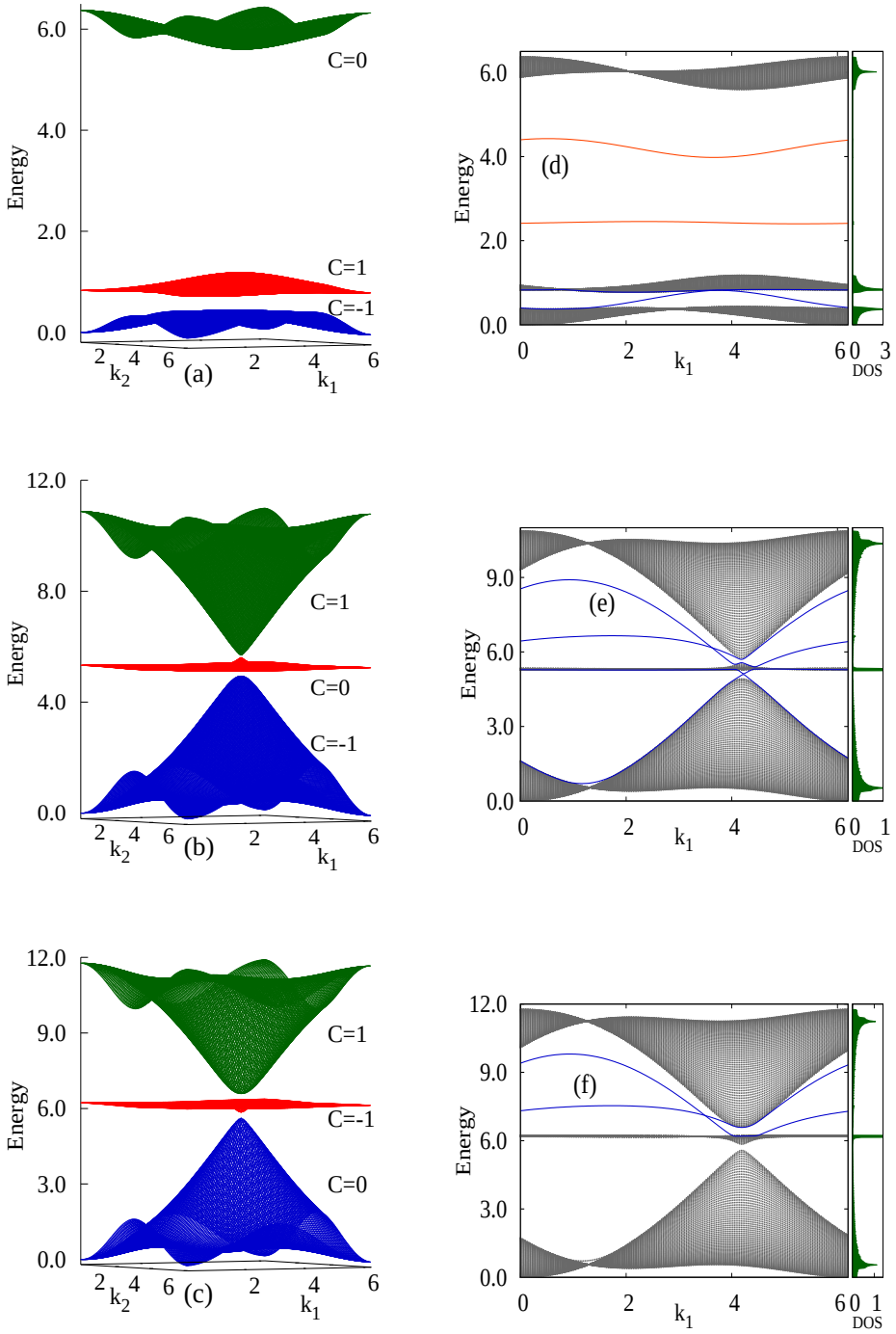

Figure 4.4: Dispersion relation of breathing kagome system for non-zero DMI strength with $J_2 = 1.0$, $D_1 = 0.1$, $D_2 = 1.5$ and (a) $J_1 = 0.2$, (b) $J_1 = 1.7$, (c) $J_1 = 2.0$. Edge state diagram for finite lattice with 70 unit cells along k_2 direction with same parameter values as the corresponding bulk band structures in the left column.

4.4 Topological properties with non-zero DMI

The kagome ferromagnet ($J_1 = J_2$ and $D_1 = D_2$) exhibits an unique first order TMI phase in the presence of DMI [19]. On the other hand, FM breathing kagome with non-zero DMI ($J_1 \neq J_2$ and $D_1 \neq D_2$) exhibits a rich topological phase diagram which includes distinct first and second order TMI phases as well as coexistence of both phases. In this section, effect of DMI on the topological properties will be discussed. DMI is turned on within upward and downward triangles with strenghts D_1 and D_2, respectively. For some specific values of J_1, D_1 and D_2, coexistence of both first and second order topological phases is found. Two such cases will be described extensively, where both edge and corner states are found simultaneously. Otherwise, distinct first or second order topological phases appear in different regions for the nontrivial cases.

Now, to characterize the first order topological phase, Chern number C_n for the n-th band has been evaluated which is defined as the integration of the Berry curvature as described in Eq. 1.6. To calculate the Chern number, we use the discretized version of the integration developed by Fukui and others [37], as explained earlier. For nontrivial first order topological insulating phase, Chern numbers of two or more bands must be non-zero while it will be identically zero for all the bands for the trivial insulating phase. Chern numbers are undefined when the bands either touch or overlap. To confirm the existence of this first order topological phase, we construct the edge state energy diagram by breaking PBC along k_2 direction, diagonalizing the resulting Hamiltonian and plotting the energy spectrum with respect to the good quantum number k_1. Likewise, for the characterization of second order topological phase, value of polarization is obtained in association with the prediction of corner states. To find the corner states a triangular replica of breathing kagome lattice with $L = 15$ is considered

by breaking PBC along both the directions.

In the presence of DMI, the kagome ferromagnet exhibits a particular TMI phase with $C_n = (1, 0, -1)$ [19]. Numbering of band index follows the ascending order starting from the lowest energy. For FM breathing kagome, the uppermost flat band for zero DMI is found to become dispersive as soon as DMI is non-zero. The bulk dispersion relations plotted in Fig. 4.4 (a), (b) and (c), with $D_1 = 0.1$ and $D_2 = 1.5$, reveal that the system is an insulator for this set of DMI in the region $0.00 \leq J_1 \leq 1.66$, as true gap exists between all the bands. At a particular point, $J_1 = 1.67$, the upper band gap vanishes and reopens thereafter. Therefore the system undergoes a phase transition at $J_1 = 1.67$. Similar phase transition occurs at $J_1 = 1.92$ when the lower band gap vanishes.

Calculating C_n for each of the cases, it is found that $C_n = (-1, 1, 0)$ for $0.00 < J_1 \leq 1.66$. When $J_1 \geq 1.68$, the Chern numbers are redistributed as $C_n = (-1, 0, 1)$. Thus, the system undergoes topological phase transition through which the upper two bands exchange Chern number of ± 1 since the upper two bands touch at a Dirac band touching point. Similar situation happens again at $J_1 = 1.92$, where lower two bands touch at a Dirac band-touching point. At this time, they exchange Chern number of ± 1 leading to new distribution, $C_n = (0, -1, 1)$.

The Figs 4.4 (d), (e) and (f) show the evolution of the gapless and gapped edge modes and depicts the way it affects the existence of corner states of the system. Pair of in-gap edge modes (denoted by red lines) indicates the existence of second order topological phase, while chiral edge modes (blue lines) signify the existence of first order topological phase. Fig. 4.4 (d) shows chiral gapless edge states connecting the lower two gapped bands according to the BBC rule since the Chern numbers are $(-1, 1, 0)$. The pair of gapped edge modes in the upper band gap indicates the existence of corner states. But this time, they

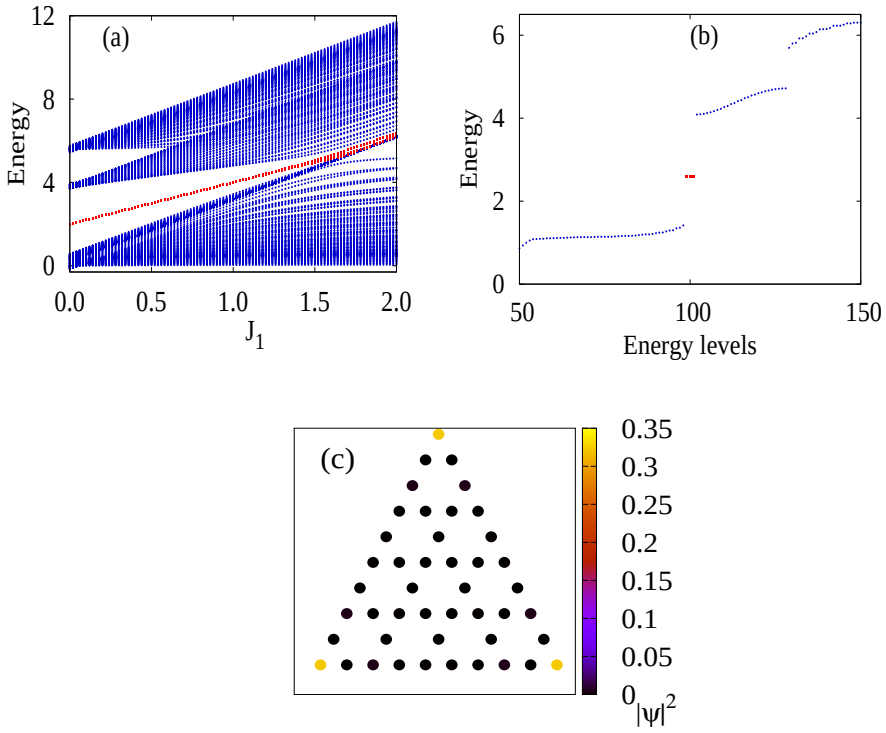

Figure 4.5: (a) Energy spectrum of breathing kagome lattice with varying J_1 for $L = 15$. D_1, D_2 and J_2 are kept constant at the values of 0.1, 1.5 and 1.0, respectively. Upto $J_1 = 1.6$, zero dimensional corner states exist (denoted by red dots) and beyond this, it decays into the bulk. (b) Energy of the same system is plotted with respect to energy levels for $J_1 = 0.3$. Three red dots at same energy (same value as in the case with zero DMI) show the states at the three corners of the finite triangle. The diagram is truncated for better resolution of the three corner states. (c) Probability distribution of a particular eigenstate corresponding to a corner state energy for $J_1 = 0.2$ and $L = 5$. It shows that the states are indeed localized at the corners and introduction of DM interaction has not changed the distribution considerably.

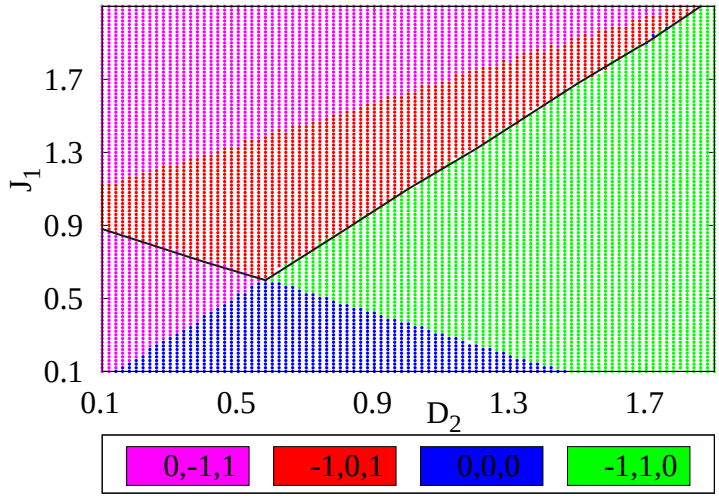

Figure 4.6: Topological phase diagram in $J_1 - D_2$ parameter space with $J_2 = 1.0$ and $D_1 = 0.1$. Four different phases are separated by different colors as shown in the lower panel. In first order, three of them are topologically nontrivial and one is trivial. The solid black line separates topologically nontrivial (lower portion) and trivial (upper portion) phases in second order. Evidently, green and magenta portions beneath the solid black line host both first and second order topological nontrivial phases.

do not cross each other. Thus, there are simultaneous existence of first and second order topological insulating phases for 1/3 and 2/3 filling, respectively. In similar fashion, Fig. 4.4 (e) and (f), correspond to the existence of other topological phases. The nature of edge states supports the pattern of Chern numbers for the corresponding parameter regions satisfying the BBC rule.

To confirm the presence of SOTMI phase, existence of the corner states is investigated. Fig. 4.5 (a) shows the energy spectra with varying J_1. It is evident that the SOTMI phase do exist up to $J_1 = 1.66$. The calculation of polarization further emphasizes our claim that TMI and SOTMI phase do simultaneously exist in the region $0.00 < J_1 \leq 1.66$. For this particular case, the topological invariant would be the value of p_1 of the uppermost band, since the gapped edge mode exist between the upper two bands. The value of p_1 remains fixed at 1/3 for the whole region, which is same as the value of p_1 for zero DMI. But,

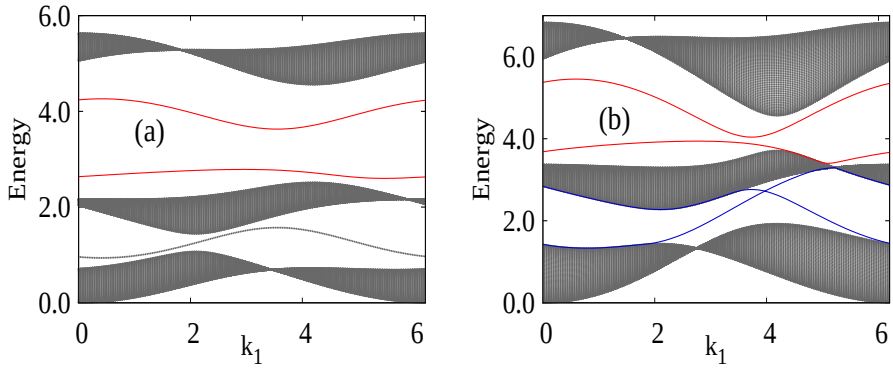

Figure 4.7: Edge state diagram for $D_1 = 0.1, D_2 = 0.9$ and (a) $J_1 = 0.3$, (b) $J_1 = 0.7$. Upper band-gap hosts two gapped pair of edge modes (denoted by red lines) in (a), while the lower one decays into the bulk in (b). A chiral edge state appears between the lower band-gap in (b).

in contrast to the zero DMI, here both corner states and non-zero polarization simultaneously persists for the region $0.00 < J_1 \leq 1.66$. This result can be implied from the fact that there is no crossover of in-gap edge modes in this insulating region. Thus, BBC as well as bulk-corner-correspondence rules are jointly satisfied both for TMI and SOTMI phases, as evident from the diagram. For $J_1 > 1.66$, the corner states decay into the bulk as well as polarization vanishes. Thus, SOTMI phase cease to exist beyond $J_1 > 1.66$.

This finding clearly predicts the existence of SOTMI phase as well as TMI phase in the region $0.00 < J_1 \leq 1.66$, when the strengths of DMI are fixed at $D_1 = 0.1$ and $D_2 = 1.5$. Therefore, DMI not only helps to extend the range of SOTMI phase from $0.0 < J_1 < 1.0$ to $0.00 < J_1 \leq 1.66$, in addition, it favors the coexistence of first and second order topological phases. The system undergoes a phase transition in the vicinity of $J_1 = 1.67$, hosting a new TMI phase thereafter.

A topological phase diagram is presented in Fig. 4.6, which is drawn with respect to two parameters J_1 and D_2, where D_1 is kept fixed at 0.1. To explain the phase diagram, let us fix the value of D_2 at 0.9. Along this line, the system is topologically trivial insulator in first order in the region $0.00 < J_1 \leq 0.41$.

Additionally, the system is found to host second order topological phase in the same region since there is a pair of in-gap edge modes in the upper band gap. At $J_1 = 0.42$ lower gap vanishes. Thereafter, the system hosts a TMI phase with $C_n = (-1, 1, 0)$ up to $J_1 = 0.97$. Thus, the system becomes topologically nontrivial in first order for $0.42 < J_1 \leq 0.97$. But, at the same time, the gapped pair of edge mode in the upper band gap changes its shape in such a manner that the lower edge mode decays into bulk as it is shown in Fig. 4.7. Because of this fact, although the value of p_1 for upper band is $1/3$ up to $J_1 = 0.97$, but the corner states are topologically protected up to $J_1 = 0.41$. So, violation of bulk-corner-correspondence rule is noted again in the region $0.42 < J_1 \leq 0.97$. Thus, for $D_1 = 0.1$ and $D_2 = 0.9$, coexistence of both phases remains in the region $0.42 < J_1 \leq 0.97$. For $J_1 > 0.97$, the upper band-gap vanishes and the system undergoes a topological phase transition where it is driven into a phase which is topologically trivial in second order but nontrivial in first order. This TMI phase is characterized by the Chern numbers $(-1, 0, 1)$. With further increase of J_1, another phase transition is observed at $J_1 = 1.57$. The resulting TMI phase has the Chern number distribution $(0, -1, 1)$.

So, it can be concluded that, although polarization, as a topological invariant, changes its value only when gap closes, its $(d-2)$ dimensional counterpart, the corner states will be found as long as the pair of in-gap edge modes survives distinctly without crossing each other or decaying into bulk band in $(d-1)$ dimension. Thus, there is an anomaly in the correspondence between two-dimensional bulk and its zero-dimensional boundary for the SOTMI phase. In addition, this diagram clearly exhibits the occurrence of phase transitions between different topological phases with the variation of parameters, J_1 and D_2.

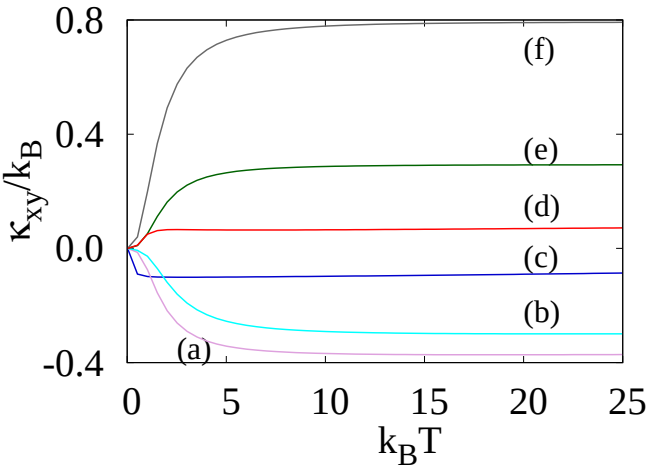

Figure 4.8: Variation of $\kappa_{xy}(T)$ as a function of T for $J_2 = 1.0$ and (a) $J_1 = 1.7, D_1 = 0.1, D_2 = 1.5$, for $C_n = (-1, 0, 1)$, (b) $J_1 = 2.2, D_1 = 0.1, D_2 = 1.5$, for $C_n = (0, -1, 1)$, (c) $J_1 = 0.2, D_1 = 0.1, D_2 = 1.5$, for $C_n = (-1, 1, 0)$, (d) $J_1 = 1.3, D_1 = -1.4, D_2 = 0.3$, for $C_n = (1, -1, 0)$, (e) $J_1 = 1.3, D_1 = 0.0, D_2 = -0.2$, for $C_n = (0, 1, -1)$, (f) $J_1 = 1.4, D_1 = -0.5, D_2 = -0.8$, for $C_n = (1, 0, -1)$.

4.5 Thermal Hall Conductivity

The values of thermal Hall conductivity (THC) of the system have been calculated for first order TMI phases. THC is useful to study the occurrence of phase transitions, and, at the same time, these values can be verified experimentally. Resulting diagram is shown in Fig. 4.8. We have included THC values for some extra TMI phases those are not discussed before. Additional TMI phases with different combinations of Chern numbers are obtained by varying all the parameters. The transverse THC can be formulated in terms of Berry curvatures, $\Omega_n(\mathbf{k})$ as [38],

$$\kappa_{xy}(T) = -\frac{{k_B}^2 T}{4\pi^2\hbar} \sum_n \iint_{1\mathrm{BZ}} c(\rho_n(\mathbf{k}))dk_x dk_y \Omega_n(\mathbf{k}). \tag{4.7}$$

Here the sum runs over all bands, n. k_B is the Boltzmann constant and $\hbar$ is the reduced Planck's constant. $\rho_n(\mathbf{k}) = 1/(e^{E_n(\mathbf{k})/k_BT} - 1)$ is the Bose distribution

function with $E_n(\mathbf{k})$ being the energy eigenvalue of the n-th band. $c(x) = (1+x)\ln\left(\frac{1+x}{x}\right)^2 - (\ln x)^2 - 2Li_2(-x)$ where $Li_2(y) = -\int_0^y dz \frac{\ln(1-z)}{z}$. In high temperature limit, THC can be simplified as $\kappa_{xy} = -\frac{k_B}{4\pi^2\hbar}\sum_n C_n \overline{E_n}$ [23], where the $\mathbf{k}$-dependent energy is replaced by the average energy of the respective band ($\overline{E_n}$). By using this equation and the distribution of Chern numbers, one can anticipate the sign of saturated value of κ_{xy} at high temperature. For example, sign will be positive (negative) if the band with higher energy has lower (higher) value of Chern number considering one of the bands always has $C_n = 0$ in this three-band system. The behavior of THC is reflected in Fig. 4.8.

4.6 Summary and Discussions

We have investigated the properties of FM Heisenberg model with and without DMI on breathing kagome lattice and established the simultaneous appearance of first and second order TMI phases for various values of the exchange and DMI strengths which have been taken of different magnitudes for upward and downward triangles. Topological phase diagram of breathing kagome ferromagnet is richer than that of kagome. Magnon dispersion relations are obtained following LSWT for any value of spin S. While only a single SOTMI phase exists when no DMI is present, either SOTMI or TMI or both of them are present for non-zero DMI strength. In order to characterize the first order conventional TMI phases the Chern numbers of the insulating band as well as chiral edge states in strip geometry are obtained. The existence of different phases with different distribution of Chern numbers and the transition between them are studied. Transverse THC values for various TMI phases are also calculated. While SOTMI phases are characterized by non-zero values of polarization or in terms of the coordinate of Wannier center, those are additionally verified by the

existence of zero-dimensional corner states where the pair of in-gap edge modes are clearly found in one dimension without any crossing. In previous studies on breathing kagome lattice, SOTI phase was found in a fermionic tight binding model [7]. A TI phase was found on another tight binding model in the presence of spin orbit coupling [39].

Six different TMI phases and one SOTMI phase are found in this system. Since the TMI phase in kagome ferromagnet has been observed before in $Lu_2V_2O_7$ [24, 25], these findings can also be verified experimentally in future. No material is available right now whose property can be explained in terms of FM breathing kagome lattice. DMI can be induced via external electric field if it is not present intrinsically [23]. Topological phases with higher Chern numbers may be obtained by introducing further neighbor interactions. Similarly, it would be more interesting to study the topological behavior of the FM models on three-dimensional pyrochlore lattice by following the same procedure. Violation of bulk-corner-correspondence rule found in some SOTMI phases demands more attention as well. Anomaly in bulk-corner-correspondence rule is reported before in a Hubbard model on kagome lattice, where gapless spin excitations around the corners are found in the presence of electron correlations instead of gapless charge excitations [33].

Bibliography

[1] Benalcazar W. A., Bernevig B. A., and Hughes T. L., Science **357**, 61 (2017).

[2] Benalcazar W. A., Bernevig B. A., and Hughes T. L., Phys. Rev. B **96**, 245115 (2017).

[3] Peng Y., Bao Y., and Von Oppen F., Phys. Rev. B **95**, 235143 (2017).

[4] Langbehn J., Peng Y., Trifunovic L., von Oppen F. and Brouwer P. W., Phys. Rev. Lett. **119**, 246401 (2017).

[5] Song Z., Fang Z., and Fang C., Phys. Rev. Lett. **119**, 246402 (2017).

[6] Schindler F., Cook A. M., Vergniory M. G., Wang Z., Parkin S. S. P., Bernevig B. A. and Neupert T., Science Advances **4**, 0346 (2018).

[7] Ezawa M., Phys. Rev. Lett. **120**, 026801 (2018).

[8] Seshadri R., Dutta A. and Sen D., Phys. Rev. B **100**, 115403 (2019).

[9] Wakao H., Yoshida T., Araki H., Mizoguchi T. and Hatsugai Y., Phys. Rev. B **101**, 094107 (2020).

[10] Geier M., Trifunovic L., Hoskam M. and Brouwer P. W., Phys. Rev. B**97**, 205135 (2018).

[11] Liu T., Zhang Y. R., Ai Q., Gong Z., Kawabata K., Ueda M. and Nori F., Phys. Rev. Lett. **122**, 076801 (2019).

[12] Dwivedi V., Hickey C., Eschmann T. and Trebst S., Phys. Rev. B **98**, 054432 (2018).

[13] Li Z., Cao Y., Yan P. and Wang X., Npj Comput. Mater. **5**, 107 (2019).

[14] B. Xie Y., Wang H. F., Wang H. -X., Zhu X. Y., Jiang J. -H., Lu M. H. and Chen Y. F., Phys. Rev. B **98**, 205147 (2018).

[15] Fukui T., Phys. Rev. B **99**, 165129 (2019).

[16] Araki H., Mizoguchi T. and Hatsugai Y., Phys. Rev. Research **2**, 012009(R) (2020).

[17] Serra-Garcia M., Peri V., SÃijsstrunk R., Bilal O. R., Larsen T., Villanueva L. G. and Huber S. D., Nature **555**, 342 (2018).

[18] Imhof S., Berger C., Bayer F., Brehm J., Molenkamp L. W., Kiessling T., Schindler F., Lee C. H., Greiter M., Neupert T. and Thomale R., Nat. Phys. **14**, 925 (2018).

[19] Zhang L., Ren J., Wang J. S. and Li B., Phys. Rev. B **87**, 144101 (2013).

[20] Owerre S. A., Phys. Rev. B **95**, 014422 (2017).

[21] Owerre S. A., J. Phys. Commun. **1**, 021002 (2017).

[22] Seshadri R. and Sen D., Phys. Rev. B **97**, 134411 (2018).

[23] Cao X., Chen K. and He D., J. Phys.: Condens. Matter **27**, 166003 (2015).

[24] Onose Y., Ideue T., Katsura H., Shiomi Y., Nagaosa N. and Tokura Y., Science, **329**, 297 (2010).

[25] Katsura H., Nagaosa N. and Lee P. A., Phys. Rev. Lett. **104**, 066403 (2010).

[26] Chisnell R., Helton J. S., Freedman D. E., Singh D. K., Bewley R. I., Nocera D. G. and Lee Y. S., Phys. Rev. Lett. **115**, 147201 (2015).

[27] Chen L., Chung J. -H., Gao B., Chen T., Stone M. B., Kolesnikov A. I., Huang Q. and Dai P., Phys. Rev. X **8**, 041028 (2018).

[28] Hirschberger M., Chisnell R., Lee Y. S. and Ong N. P., Phys. Rev. Lett. **115**, 106603 (2015).

[29] Joshi D. G., Phys. Rev. B **98**, 060405(R) (2018).

[30] Deb M. and Ghosh A. K., J. Phys.: Condens. Matter **31**, 345601 (2019).

[31] Xue H., Yang Y., Gao F., Chong Y. and Zhang B., Nature Materials **18**, 108 (2019).

[32] Chen X., Deng W. M., Shi F. L., Zhao F. L., Chen M. and Dong J. W., Phys. Rev. Lett. **122**, 233902 (2019).

[33] Kudo K., Yoshida T. and Hatsugai Y., Phys. Rev. Lett. **123**, 196402 (2019).

[34] Ezawa M., Phys. Rev. B **98**, 201402(R) (2018).

[35] Peterson C. W., Benalcazar W. A., Hughes T. L. and Bahl, Nature **555**, 346âĂŞ350 (2018).

[36] El Hassan A., Kunst F. K., Moritz A., Andler G., Bergholtz E. J., and Bourennane M., Nature photonics **13**, 697 (2019).

[37] Fukui T., Hatsugai Y. and Suzuki H., J. Phys. Soc. Jpn. **74**, 1674 (2005).

[38] Matsumoto R. and Murakami S., Phys. Rev. Lett. **106**, 197202 (2011).

[39] Bolens A. and Nagaosa N., Phys. Rev. B **99**, 165141 (2019).

Chapter 5

Topology on monolayer and bilayer depleted Lieb lattices

5.1 Overview

In this study, Haldane-like model is formulated on the depleted Lieb lattice which is found capable to host nontrivial topological phases. 2D non-Bravais lattices are generally derived from either square or triangular lattices which are Bravais. Lieb lattice belongs to the first group as it is derived from square lattice by depleting 25% of lattice sites in a regular manner. The reciprocal lattice is a square lattice. The depleted Lieb lattice is constructed from the square lattice by erasing 50% of its sites. Lieb lattice is tripartite square lattice while the depleted one is bipartite.

A number of investigations have been parallelly carried out on the Haldane model formulated over bilayer systems those yield nontrivial phases, specially on bilayer graphene systems [1]. Topological characterization of such systems facilitates the emergence of new phases in the expanded parameter space where the band structure gets enriched due to the multiplication of band number by

two. In another study, existence of flat bands with nonzero Chern number and fractional QHE has been reported on twisted bilayer graphene [2]. In this chapter, a Haldane model on the bilayer depleted Lieb lattice has also been formulated where a pair of topological phases is found to exist.

Among the several lattice systems exhibiting CI phase, the most fascinating one is the Lieb lattice since it exhibits several exotic topological properties under various interactions as summarized here. Tight-binding and Heisenberg models formulated on Lieb lattice essentially yield a three-band systems as it is composed of three non-equivalent lattice sites. In tight-binding regime, it shows a flat band [3] and a quadratic band crossing point or a Dirac cone, which is found topologically protected. In the presence of spin-orbit coupling (SOC) or incorporation of complex NNN hopping term, a gap opens up at the Dirac point and the model becomes topological [4, 5]. Since the Lieb lattice possesses inversion symmetry this phase is characterized by Z_2 topological invariant [6]. FTI phase on Lieb lattice has also been reported in helical photonic wave-guide [7]. TMI phase is found in FM Heisenberg model framed on Lieb lattice along with DM interaction [8]. Stacked multi-layer Lieb lattices have been shown to host CI phase with high Chern numbers in the presence of SOC [9]. Basically Lieb lattice is the 2D analogue of the 3D lattice found in perovskites. There have been several efforts to realize materials based on the Lieb lattice. This 2D structure has been successfully demonstrated by means of photonic and cold-atom crystals. In another attempt, it has been synthesized by the surface state electrons of Cu(111) confined by an array of CO molecules positioned with a scanning tunnelling microscope [10]. More recently, first principle study predicts that two covalent organic frameworks, sp^2C-COF and sp^2N-COF are actually two material realizations of organic-ligand-based Lieb lattice [11].

Depleted Lieb lattice was introduced before by Oliveira *et. al.*, where a XXZ

Heisenberg model was formulated on this lattice. The magnetic model comprised of three different nearest-neighbor FM exchange interactions [12]. However, no topological phase was found even in the presence of DMI and external magnetic field. In this work, we focus on the depleted Lieb lattice, and its bilayer structure. But nontrivial topological phases are obtained by formulating tight-binding Hamiltonian on those systems. This lattice is constructed from the Lieb lattice by removing few lattice sites in a regular way. A closer look reveals that it is nothing but the Bravais lattice with rectangular unit cell. And this particular geometry is formed by the Cu atoms observed in doped cuprate superconductors with larger Cu-O-Cu bond length and smaller buckling degree [13]. However, a tight-binding model similar to the Haldane model with nonsymmetric terms is formulated in such a way that the resulting system can be studied in terms of non-Bravais depleted Lieb lattice. In this model NNNN hopping terms are made complex unlike the original Haldane model where NNN terms are complex instead. Without the NNNN hopping the system is again trivial although the presence of staggered site energy induce a gap in this two-sublattice system. Both the complex NNNN hopping and staggered onsite energy are the essential ingredients of this model. The effect of uniform onsite energy would be trivial for obvious reasons.

Furthermore, a coupled bilayer version of this depleted Lieb lattice is introduced where the coupling among the layers is accomplished by the inter-layer hopping between same type of NN sublattice sites. It is shown that the bilayer system hosts four different topological phases. It is expected that those depleted lattice structures can be generated using the same techniques employed for Lieb lattice as discussed before [10].

The chapter is organized in the following way. In section 5.2, depleted Lieb lattice is described and the tight-binding Hamiltonian is formulated. In section

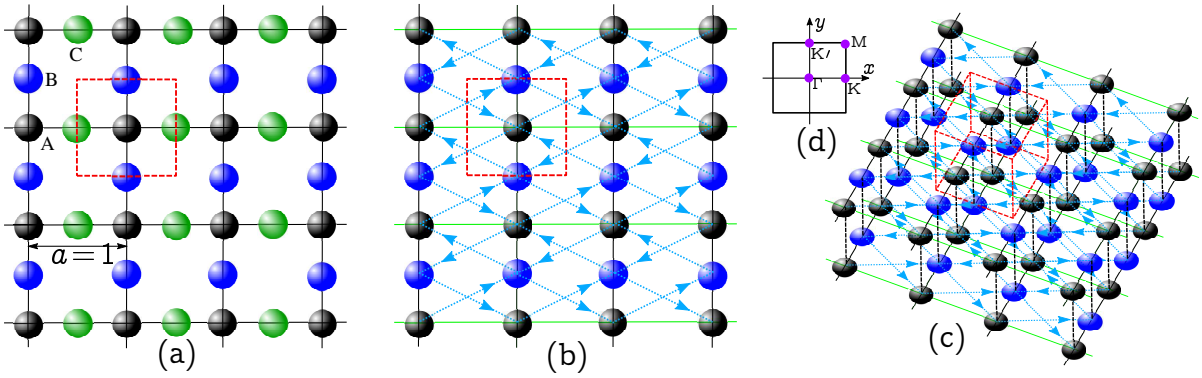

Figure 5.1: (a) Lieb lattice with three basis points shown by black (A), blue (B) and green (C) spheres. Unit cell is shown by red dashed square. (b) Depleted Lieb lattice with two basis points shown by black (A), blue (B). Strength of NN hopping between A and B sites along y direction is t_1 (black line). Strength of NNN hopping between A sites along x direction is t_2 (green line), while t_3 is that along the diagonals between the NNNN lattice sites (blue dotted line). Sign of the complex phase is assumed positive when hopping is along the direction of the arrow. (c) Bilayer depleted Lieb lattice, where the hopping strength between top and bottom layers is t_4 (black dashed line). (d) The first Brillouin zone (BZ) of the lattice. High-symmetry points of square BZ, Γ (0, 0), K (π, 0), K′ (0, π), and M (π, π) have been marked.

5.3, spectral properties are described. This is followed by section 5.4, where the topological phases of this monolayer system are presented. In next section 5.5, topological properties of the bilayer version of this lattice are described. Finally, in section 5.6, discussions and conclusions on this work are summarized.

5.2 Formulation of Tight-binding Hamiltonian on depleted Lieb lattice

Geometry of 2D Lieb lattice consisting of three sublattices with A (black), B (blue) and C (green) spheres is shown in Fig. 5.1(a). Unit cell is shown by red dashed square containing the three different sites. The depleted Lieb lattice is shown in Fig. 5.1(b), where the green sub-lattice points are removed. This two-

sublattice system can be generated alternatively by depleting blue sub-lattice points instead of green. The resulting structure is nothing but the rectangular Bravais lattice. The NN bonds are depicted in black, while the NNN bonds are green. The NNNN hoppings are complex as well as nonsymmetric owing to their directionality. Because of this nonsymmetric bonds the resulting Hamiltonian is composed on this non-Bravais lattice. It means adjacent rectangular plaquettes along the vertical direction are not identical. Although the Lieb lattice preserves the four-fold rotational symmetry (C_4) of the square lattice, depleted Lieb lattice possesses the two-fold (C_2) rotational symmetry. Now, the tight-binding Hamiltonian on this system is formulated as

$$H = \left[t_1 \sum_{\langle jj' \rangle} c_j^\dagger c_{j'} + t_2 \sum_{\langle\langle jj' \rangle\rangle \in A} c_j^\dagger c_{j'} + t_3 \sum_{\langle\langle\langle jj' \rangle\rangle\rangle} e^{i\phi_{jj'}} c_j^\dagger c_{j'} + H.c\right] + \sum_j \mu_j c_j^\dagger c_j. \quad (5.1)$$

The summations $\langle\cdot\rangle$, $\langle\langle\cdot\rangle\rangle$ and $\langle\langle\langle\cdot\rangle\rangle\rangle$ run over NN, NNN and NNNN pairs, respectively. $c_j^\dagger\,(c_j)$ is the fermionic creation (annihilation) operator for an electron at the j-th site. t_1, t_2 and t_3 are the strengths of NN, NNN and NNNN hopping, shown in black, green lines and blue dotted arrow, respectively in Fig. 5.1(b). μ_i is the site dependent chemical potential. The direction of the phases $\phi_{jj'}$ is shown in Fig. 5.1 (b). The sign of $\phi_{jj'}$ is assumed positive, $\phi_{jj'} = \phi$ (negative, $\phi_{jj'} = -\phi$), when it is directed along (opposite) the arrowhead. Sign of the phases are chosen in this way to ensure the net effective magnetic field arising from those phases per square plaquette is zero. The onsite energy is taken as $\mu = -\mu_A = \mu_B$, which breaks sublattice symmetry. Hamiltonian can be expressed as

$$H = \sum_{jj'} \psi_j^\dagger\, g_{jj'}\, \psi_{j'}, \quad (5.2)$$

where $\psi_j^\dagger = [c_{Aj}^\dagger \;\; c_{Bj}^\dagger]$, $g_{jj'} = g_0 I_0 + \boldsymbol{g}\cdot\boldsymbol{\sigma}$, $g_0 = t_2\delta_{j,j'\in A}$, $g_x = t_1\delta_{j,j'\in \mathrm{NN}} + t_3\cos(\phi)\delta_{j,j'\in \mathrm{NNNN}}$, $g_y = t_3\sin(\phi)\delta_{j,j'\in \mathrm{NNNN}}$, $g_z = -\mu$, I_0 is the 2×2 identity

matrix and σ_α, $\alpha = x, y, z$ are the Pauli matrices.

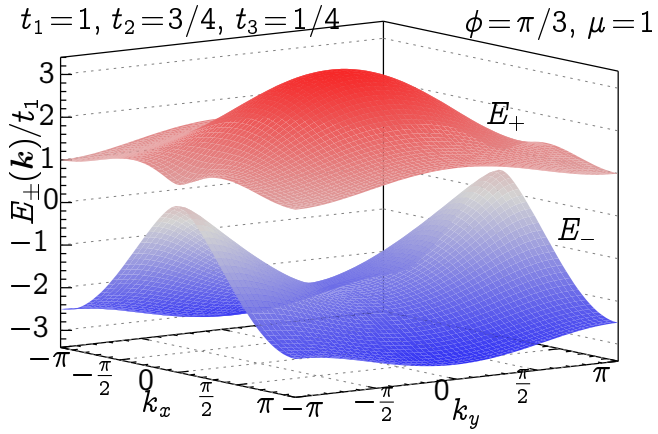

Figure 5.2: Dispersion relations, $E_\pm(\boldsymbol{k})$, when $t_2/t_1 = 3/4$, $t_3/t_1 = 1/4$, $\phi = \pi/3$, and $\mu/t_1 = 1$.

Length of the each side of the square unit cell is set as the unity ($a = 1$). The NN vectors between A and B sites are $\boldsymbol{\delta}_1 = (0, 1/2)$, the NNN vector between the A sites are $\boldsymbol{\delta}_2 = (1, 0)$ and the NNNN vectors between the A and B sites along the diagonals are $\boldsymbol{\delta}_3 = (1, 1/2)$. We set $t_1 = 1$ throughout this chapter. Hamiltonian is transformed into the reciprocal space under the Fourier transformation,

$$c_j = \frac{1}{\sqrt{N}} \sum_{\boldsymbol{k} \in \mathrm{BZ}} c_{\boldsymbol{k}}\, e^{i\boldsymbol{k}\cdot\boldsymbol{R}_j},$$

where N is the number of unit cells, $\boldsymbol{k} = (k_x, k_y)$, and $\boldsymbol{R}_j$ is the Bravais vector for the site j. So the Hamiltonian is

$$H = \sum_{\boldsymbol{k}} \psi_{\boldsymbol{k}}{}^\dagger\, h(\boldsymbol{k})\, \psi_{\boldsymbol{k}}, \tag{5.3}$$

where $\psi_{\boldsymbol{k}}^{\dagger} = [c_{Ak}^{\dagger}\ c_{Bk}^{\dagger}]$, is a two-component spinor and $h(\boldsymbol{k}) = h_0 I_0 + \boldsymbol{h}\cdot\boldsymbol{\sigma}$, where,

$$\begin{cases} h_0 = t_2 \cos k_x, \\ h_x = 2t_1 \cos\left(\frac{k_y}{2}\right) + 4t_3 \cos(\phi)\cos(k_x)\cos\left(\frac{k_y}{2}\right), \\ h_y = 4t_3 \sin(\phi)\sin(k_x)\sin\left(\frac{k_y}{2}\right), \\ h_z = t_2 \cos k_x - \mu. \end{cases}$$

The phase ϕ appears here in the off-diagonal terms while it is found in diagonal terms for the Haldane model [2]. Conservation of TRS and PHS for $h(\boldsymbol{k})$ means that the following relations

$$\begin{cases} \mathcal{T}\, h(\boldsymbol{k})\, \mathcal{T}^{-1} = h^*(-\boldsymbol{k}), \\ \mathcal{P}\, h(\boldsymbol{k})\, \mathcal{P}^{-1} = -h^*(-\boldsymbol{k}), \end{cases}$$

will be satisfied under the appropriate choice of TRS and PHS operators, $\mathcal{T}$, and $\mathcal{P}$, respectively. However, no operator is found to satisfy the above relations due to all the components, h_α, being nonzero and their typical dependence on $\boldsymbol{k}$. As a consequence, chiral symmetry is also broken. This 2D system belongs to class A, and hence its topological invariant may assume integral value upon its characterization [14]. The spectrum of $h(\boldsymbol{k})$ does not possess the inversion symmetry around the zero energy because of the absence of PHS. Dispersions of this two-band system are given by

$$E_{\pm}(\boldsymbol{k}) = h_0 \pm \sqrt{h_x^2 + h_y^2 + h_z^2}.$$

The dispersions within the BZ are shown in Fig. 5.2 for $t_2/t_1 = 3/4$, $t_3/t_1 = 1/4$, $\phi = \pi/3$, and $\mu/t_1 = 1$. It clearly indicates that inversion symmetry for the spectrum of $h(\boldsymbol{k})$ around $E = 0$ is lost. A band gap exists for obvious reason.

Inversion symmetry for the spectrum will be restored if h_0 becomes independent of $\boldsymbol{k}$ and $h_z = 0$. The band-structures along the high symmetric pathway for various parameter values are obtained and their properties are described in the next section.

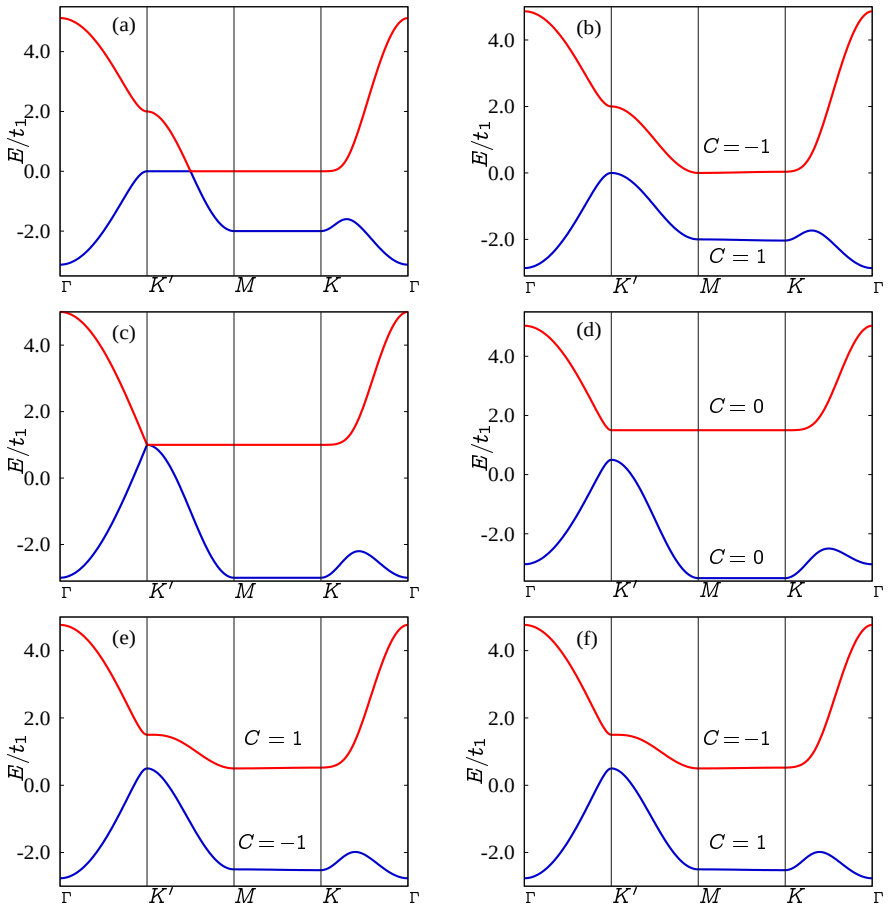

Figure 5.3: Band structure of depleted Lieb lattice along the high symmetry pathway Γ-K'-M-K-Γ of the BZ is shown with the variation of μ and ϕ, when $t_2/t_1 = 1, t_3/t_1 = 1/2$. (a) $\mu = 0$, $\phi = 0$, trivial semi-metallic phase with no band gap, (b) $\mu = 0$, $\phi = \pi/6$, nontrivial semi-metallic phase with pseudo-gap, (c) $\mu/t_1 = 1$, $\phi = 0$, trivial semi-metallic phase with band-gap point shifting to K' point, (d) $\mu/t_1 = 1.5$, $\phi = 0$, trivial insulating phase with true band gap, (e) $\mu/t_1 = 0.5$, $\phi = \pi/6$, Chern semimetallic phase with $C_n = (-1, 1)$, (f) $\mu/t_1 = 0.5$, $\phi = -\pi/6$, Chern semimetallic phase with $C_n = (1, -1)$.

5.3 Spectral Properties of depleted Lieb Lattice

Four different phases of the system are noted, which are shown in six band diagrams in Fig. 5.3 (a)-(f). Among them two phases are topological as indicated in Fig. 5.3 (b), (e) and (f). In order to explain the character of them, evolution of spectral properties with the variation of complex phase ϕ and onsite energy μ has been demonstrated in this section. So, values of other parameters are kept fixed, namely $t_2/t_1 = 1$ and $t_3/t_1 = 1/2$. When μ and ϕ are both zero, system is defined only by NN, NNN and NNNN interactions. In this condition, the system remains in one of its trivial state, when the two bands touch each other at the point $(k_x, k_y) = (\pi/2, \pi)$, an intermediate between two high symmetry points K' and M, as shown in Fig. 5.3 (a). It means the system always exhibit semimetallic state when $\mu = 0$ and $\phi = 0$. Now, in the presence of complex NNNN phase, $\phi \neq 0$, but $\mu = 0$, the two bands get separated immediately as shown in Fig. 5.3 (b). Again the system remains in semimetallic phase, since the bands are separated by indirect (pseudo) band-gap. This phase is termed as pseudo semimetallic phase. In this case, peak of lower band appears at K' while bottom of upper band remains in M-K region. The system becomes nontrivial as the bands acquire nonzero Chern number. On the other hand, when $\mu \neq 0$, but $\phi = 0$, the band-touching point shifts leftwards with the increase of μ, and at $\mu/t_1 = 1$, it moves ultimately to K' point of the BZ (Fig. 5.3 (c)). It happens due to fact that bottom of upper band extends with the increase of μ, and it reaches K', although peak of lower band remains fixed at K'. This is nothing but another semimetallic phase where band touching occurs at one of the high symmetry points, K'.

With the further increase of μ, or beyond $\mu/t_1 = 1$, but $\phi = 0$, the band gap opens up eventually at the K' point and the system lies in trivial insulating

phase. The band-structure at the values of $\mu/t_1 = 1.5$ and $\phi = 0$ is shown in Fig. 5.3 (d), which indicates the existence of true band gap. Now, when both the values of μ and ϕ are nonzero, the system is always in a pseudo-gapped phase and in most of the cases, the phase is nontrivial, namely CSM Phase. One of the case is demonstrated in Fig. 5.3 (e). At these values, both the bands acquire nonzero Chern numbers. The lower (upper) band acquires $C = -1$ ($C = 1$). The sign of the Chern numbers reverses with the sign reversal of ϕ as shown in Fig. 5.3 (f), leading to another CSM phase. The band structures of the last two cases are similar since the magnitudes of all the parameters are the same. However, in every case, it lacks inversion symmetry about $E = 0$, due to obvious reason. Among the four phases, two are topologically nontrivial, while the remaining two are trivial. The trivial phases are insulating and semimetallic. Two CSM phases emerge here, although no CI phase is noted in this case.

5.4 Topological Properties

5.4.1 Chern numbers and Hall conductivity

As pointed out before, nontrivial topological phases are characterized by the value of topological invariant, C which can assume only integral value as it belongs to 2D symmetry class A [14]. So, for both CI and CSM phases, each energy band is characterized by band Chern number, C_n, where n is the band index. Again, over all the bands, $\sum_n C_n = 0$, and some of the bands must have nonzero C_n for the system to be nontrivial. However, for the two-band topological system, each band must have nonzero value of C_n, but opposite in sign. In this section, value of C_n has been determined as per Eq. (1.6) in order to characterize the topological phases of this system. C_n is well-defined for a particular band as long as it does not touch other neighbouring bands *i.e.*,

there exists true or pseudo-gap between the bands. Chern metallic (CM) phase has also been reported before, where bands overlap each other [15], but in that case Chern number C_n is not defined and the bands are characterized by Hall conductance. In our numerical calculation, we use the discretized version of Eq. (1.6) introduced by Fukui and others in order to determine C_n [16].

In this model, the presence of TRS breaking NNNN phase, ϕ and sublattice symmetry breaking term μ gives rise to the non-vanishing Chern numbers. The system is in nontrivial phase for the entire range $-1 < \mu/t_1 < 1$, and $-\pi \leq \phi \leq \pi$, except at $\phi = 0$. As soon as $|\mu|/t_1 = 1$, transition occurs from nontrivial to trivial phase, and the Chern numbers of the bands become zero. For $\phi < 0$ ($\phi > 0$), the Chern numbers are $C = (1, -1)$ ($C = (-1, 1)$). So, whenever the value of ϕ crosses the $\phi = 0$ line for $-1 < \mu/t_1 < 1$, phase transition occurs from $C = (-1, 1)$ to $C = (1, -1)$ which is accompanied by closing and reopening of the band gap.

However, Chern numbers for this 2D two-band system can be obtained analytically using the generalized formula [17],

$$C_n = \frac{1}{2} \sum_{\boldsymbol{k} \in D_j} \text{sgn}(J(\boldsymbol{k})_z) \cdot \text{sgn}(h(\boldsymbol{k})_z), \tag{5.4}$$

where $\boldsymbol{J}(\boldsymbol{k}) = (\partial_{k_x} \boldsymbol{h}(\boldsymbol{k})) \times (\partial_{k_y} \boldsymbol{h}(\boldsymbol{k}))$, and D_j's are the Dirac points for the Hamiltonian. Dirac point corresponds to the location in the BZ where doubly degenerate states exist. In this case, by choosing $h(\boldsymbol{k})_z$ as the arbitrary axis, Dirac points are obtained by setting $h(\boldsymbol{k})_x = 0$, and $h(\boldsymbol{k})_y = 0$. At this moment, locations of Dirac points are obtained by the solutions of the equation, $h(\boldsymbol{k})_z = 0$. Thus the coordinates of the Dirac points are given by $D_1 = (0, \pi)$, and $D_2 = (\pi, \pi)$ for $\phi \neq 0$, those are nothing but the high-symmetry points in BZ, K' and M, respectively. Now $\text{sgn}(J_z(\boldsymbol{k}))$ and $\text{sgn}(h_z(\boldsymbol{k}))$ in the parameter space

can be obtained in a simple way which are given in the table 5.1 when $t_2/t_1 = 1$, and $t_3/t_1 = 1/2$.

Conditions	$[\text{sgn}(h_z)\cdot\text{sgn}(J_z)]_{D_1}$	$[\text{sgn}(h_z)\cdot\text{sgn}(J_z)]_{D_2}$	C_n
$-1<\mu/t_1<1$, $0<\phi<\pi$	$1\cdot 1=1$	$(-1)\cdot(-1)=1$	1
$\mu/t_1<-1$, $0<\phi<\pi$	$1\cdot 1=1$	$1\cdot(-1)=-1$	0
$\mu/t_1>1$, $0<\phi<\pi$	$(-1)\cdot 1=-1$	$(-1)\cdot(-1)=1$	0
$-1<\mu/t_1<1$, $-\pi<\phi<0$	$1\cdot(-1)=-1$	$(-1)\cdot 1=-1$	-1
$\mu/t_1<-1$, $-\pi<\phi<0$	$1\cdot(-1)=-1$	$1\cdot 1=1$	0
$\mu/t_1>1$, $-\pi<\phi<0$	$(-1)\cdot(-1)=1$	$(-1)\cdot 1=-1$	0

Table 5.1: Chern number in different parameter regime using the Eq. (5.4).

Afterwards it is straightforward to check that in the parameter regime: $-1 < \mu/t_1 < 1$, $\phi = \pi/6$, the value of Chern number, $C_n = \frac{1}{2}(1+1) = 1$, and for the parameter regime: $|\mu|/t_1 > 1$, $\phi = \pi/6$, the value of Chern number, $C_n = \frac{1}{2}(-1+1) = 0$, and so on. Evidently, the result matches with the numerically calculated values as obtained before. Therefore, the system undergoes phase transitions at the points, $\mu/t_1 = \pm 1$, for any nonzero values of ϕ, where the transition takes place between nontrivial and trivial phases. Another transition between two nontrivial phases occurs around the point $\phi = 0$, irrespective of any values of the remaining parameters. Band gap vanishes at every transition point. Obviously coordinates of D_j's depend on the values of parameters.

5.4.2 Topological Edge States

The Hall-conductivity ($\sigma_H(E)$) is another important quantity for determining topological phase since it can be verified experimentally. At zero temperature,

(a)

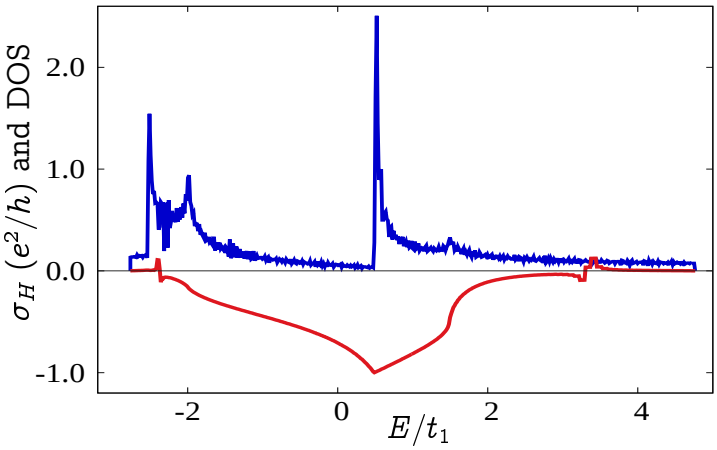

Figure 5.4: The Hall conductance σ_H (red line) and DOS (blue line) with respect to the Fermi energy E for $t_2/t_1 = 1$, $t_3/t_1 = 1/2$, $\mu/t_1 = 1/2$, $\phi = \pi/6$. σ_H shows a sharp edge instead of a plateau due to semimetallic phase. It indicates the absence of true band gap.

$\sigma_H(E)$ for this system has been estimated numerically by using the Kubo formula [12], as per Eq. (1.7). Now, according to Eq. (1.16), the value of $\sigma_H(E)$ over any Hall plateau becomes equal to the sum of all Chern numbers carried by the bands having energy lower than it. The Hall-conductivity shows quantized plateau as long as Fermi energy lies in the band-gap. The height of the plateau is determined by the Chern number of respective bands according to Eq. (1.16). Variations of $\sigma_H(E)$ and DOS for the monolayer depleted Lieb lattice with respect to Fermi energy, E are shown in Fig. 5.4. As shown in Fig. 5.4, the height of the plateau is $\sigma_H = n(e^2/h)$, with $n = -1$ since the Chern number distribution is $C_n = (-1, 1)$. The width of the plateau tends to zero since the phase is always semimetallic. $\sigma_H(E)$ shown in Fig. 5.4 mostly assumes negative values due to the topological phase $C_n = (-1, 1)$. Obviously it will be opposite if it is drawn for the other topological phase $C_n = (1, -1)$.

BBC rule states that the sum of Chern numbers up to the i-th band,

$$\nu_i = \sum_{j \leq i} C_j, \tag{5.5}$$

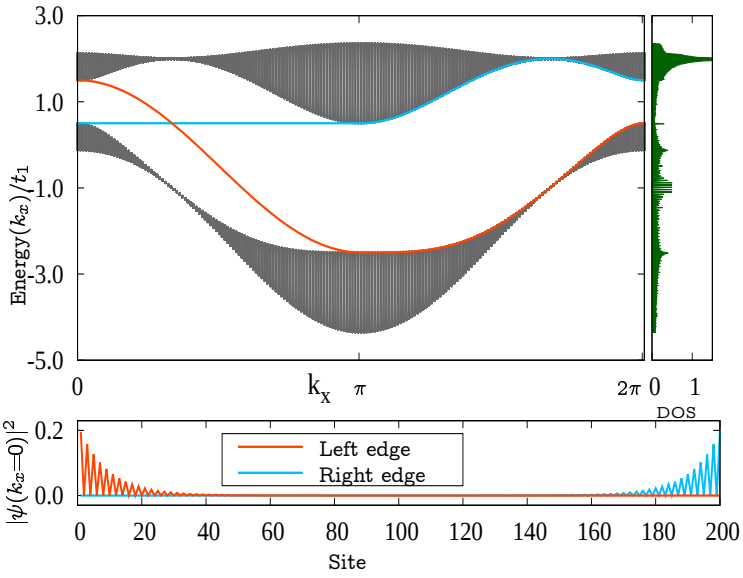

Figure 5.5: Edge states of depleted Lieb lattice for the parameters $t_2/t_1 = 1$, $t_3/t_1 = 1/2$, $\mu/t_1 = 1/2$, $\phi = 2\pi/3$ for $N = 200$ unit cells along y direction. Chern numbers of the bands are $C_n = -1, 1$. The side-panel indicates the density of states. Lower panel shows the distribution of probability density of left (orange) and right (skyblue) going edge states with respect to site number of the strip for $k_x = 0$.

is equal to the number of pair of edge states in the gap [18]. In order to establish this relation, a 1D ribbon of depleted Lieb lattice is created by removing the periodic boundary condition along y direction so that k_y is no longer a good quantum number. We consider $N = 200$ sites along y-direction and diagonalize the resulting Hamiltonian as a function of good quantum number k_x, since the PBC along x-direction is present.

In Fig. 5.5, the energy eigen-values are plotted for $t_2/t_1 = 1, t_3/t_1 = 1/2$, $\mu/t_1 = 1/2$, $\phi = \pi/6$. Evidently, one pair of edge modes exists in the band gap according to BBC rule since the Chern numbers are $(-1, 1)$ in ascending order of energy. Two edge modes connect the two bands but in opposite direction. The edge states are always localized in the left edge (orange curves) or right edge (skyblue curves) as verified from the lower panel of Fig. 5.5. Edge states

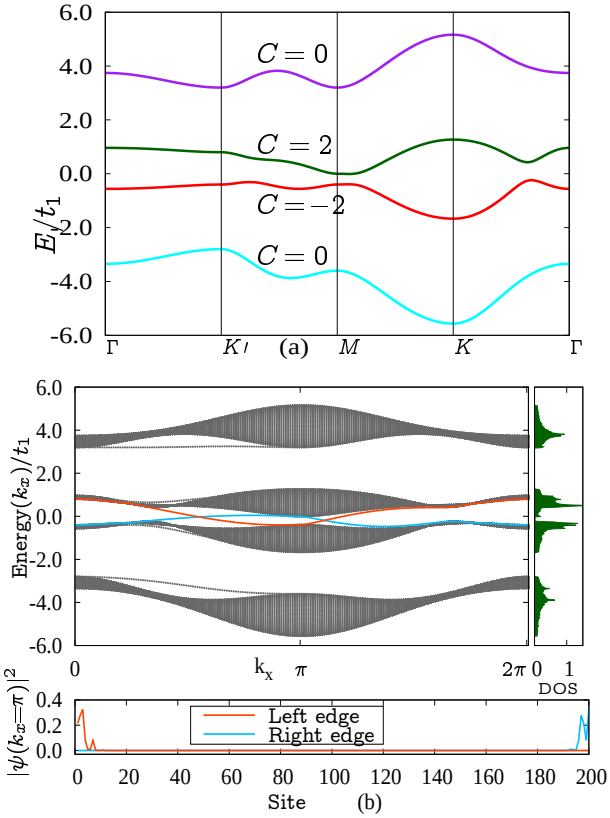

Figure 5.6: (a) Band structure along the high symmetry points of BZ for the bilayer depleted Lieb lattice when $t_2/t_1 = 0.2$, $t_3/t_1 = 0.5$, $t_4/t_1 = 1.8$, $\mu/t_1 = 1.4$, $\phi^b = 2.8$, $\phi^t = 1.6$. (b) Edge states of the bilayer depleted Lieb lattice ribbon for the same parameters for $N = 200$ unit cell along y direction. Chern numbers of the bands are $C_n = (0, -2, 2, 0)$. The side-panel indicates the DOS of the ribbon. Lower panel shows the distribution of probability density of left (orange) and right (skyblue) going edge states with respect to site number of the strip for $k_x = \pi$.

are chiral in nature since the states with positive (negative) group velocity are localized in the right (left) edge. The side panel shows the value of density of states of the system with ribbon geometry, which clearly indicates the absence of true (direct) band gap for those particular parameters. Tight-binding model identical to the original Haldane model, comprising complex NNN term and absence of NNNN hopping could not lead to nontrivial topology for the depleted Lieb lattice.

5.5 Bilayer depleted Lieb lattice

5.5.1 Formulation of Hamiltonian

In this section, a system for coupled bilayer of depleted Lieb lattice is considered, where two monolayer lattice is stacked identically. So, the A (B) sublattice of the bottom layer lies exactly below the A (B) sublattice of the top layer. Structure of bilayer depleted Lieb lattice is shown in Fig. 5.1 (c). Similar to the monolayer model, the tight binding Hamiltonian is formulated in the following manner,

$$\begin{aligned} H &= \sum_{q\in t,b}\left[t_1\sum_{\langle jj'\rangle} c_j^{q\dagger}\,c_{j'}^{q} + t_2\sum_{\langle\langle jj'\rangle\rangle\in A} c_j^{q\dagger}\,c_{j'}^{q} + t_3\sum_{\langle\langle\langle jj'\rangle\rangle\rangle} e^{i\phi_{jj'}^{q}} c_j^{q\dagger}\,c_{j'}^{q} + H.c\right] \\ &+ \; t_4\left[\sum_j c_j^{t\dagger}c_j^{b} + H.c\right] + \sum_{j,q\in t,b}\mu_j c_j^{q\dagger}\,c_j^{q}, \end{aligned} \tag{5.6}$$

where q indicates the layer index, which can be 't' (top layer) or 'b' (bottom layer). $c_j^{q\dagger}$ (c_j^{q}), $q \in t$, b, is the fermionic creation (annihilation) operator for an electron at the j-th site at top (t) or bottom (b) layer. t_1, t_2 and t_3 are the strengths of NN, NNN and NNNN hopping respectively and these are same for both the layers. t_4 is the strength of inter-layer hopping between A (and B) sublattices of both the layer. The direction of the phases $\phi_{jj'}$ is same as in monolayer case, while ϕ^t and ϕ^b can be different. However, choice of directions conforms to the fact that total field crossing the square plaquette is again zero. The onsite energy is taken as $\mu_B = -\mu_A = \mu$, for both the layers. None other than NN hopping between the two layers is taken into account.

Using PBC along both x and y directions, the Hamiltonian can be written in the momentum space:

$$H = \sum_k \psi_{\boldsymbol{k}}^{\dagger}\, h(\boldsymbol{k})\, \psi_{\boldsymbol{k}}, \tag{5.7}$$

where $\psi_{\boldsymbol{k}}^{\dagger} = [c_{A\boldsymbol{k}}^{t\dagger}\, c_{B\boldsymbol{k}}^{t\dagger}\, c_{A\boldsymbol{k}}^{b\dagger}\, c_{B\boldsymbol{k}}^{b\dagger}]$, is a four-component spinor and $h(\boldsymbol{k})$ is a 4×4

matrix. The upper diagonal components of $h(\mathbf{k})$ are given by

$$
\begin{aligned}
h_{11} &= -\mu + 2t_2 \cos\left(k_x\right) = h_{33}, \\
h_{12} &= 2t_1 \cos\left(\frac{k_y}{2}\right) + 4t_3 \cos\left(\phi^b\right) \cos\left(k_x\right) \cos\left(\frac{k_y}{2}\right) \\
&\quad - 4it_3 \sin\left(\phi^b\right) \sin\left(k_x\right) \sin\left(\frac{k_y}{2}\right), \\
h_{13} &= t_4 = h_{24}, \\
h_{22} &= \mu = h_{44}, \\
h_{34} &= 2t_1 \cos\left(\frac{k_y}{2}\right) + 4t_3 \cos\left(\phi^t\right) \cos\left(k_x\right) \cos\left(\frac{k_y}{2}\right) \\
&\quad - 4it_3 \sin\left(\phi^t\right) \sin\left(k_x\right) \sin\left(\frac{k_y}{2}\right).
\end{aligned}
\tag{5.8}
$$

The other components are zero and the lower diagonal components are complex conjugate of the upper diagonal components. Diagonalizing this matrix numerically, we obtain the band spectrum. In the large parameter-space, there is very few region where the system is in a insulating or semi-metallic phase. In most of the region, the system is in metallic phase. One of the nontrivial insulating phase is shown in Fig. 5.6 (a), in which the middle bands carry nonzero Chern numbers. Similarly, one nontrivial semimetallic phase has been identified as shown in Fig. 5.7. No inversion symmetry about $E = 0$ is found in those band structures which means PHS is absent in this bilayer model like the monolayer one.

5.5.2 Topological Properties

Following Eq. (1.6) and the numerical method developed by Fukui and others, we calculate the Chern numbers of the band. Nonzero Chern numbers are obtained for the values $t_2/t_1 = 0.2$, $t_3/t_1 = 0.5$, $t_4/t_1 = 1.8$, $\mu/t_1 = 1.4$, $\phi^b =$

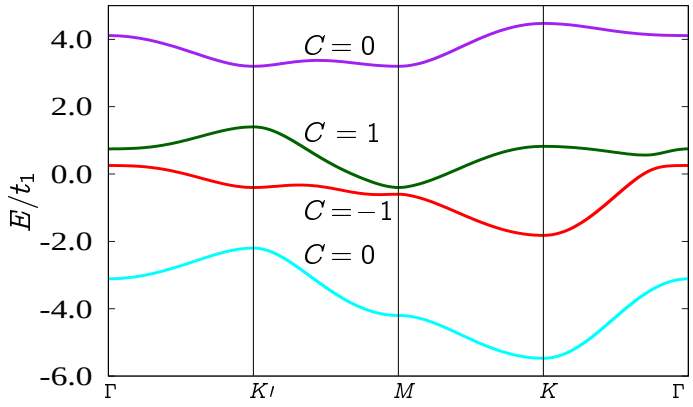

Figure 5.7: Band structure along the high symmetry points of BZ for the bilayer depleted Lieb lattice when $t_2/t_1 = 0.5$, $t_3/t_1 = 0.25$, $t_4/t_1 = 1.8$, $\mu/t_1 = 1.4$, $\phi^b = 2.8$, $\phi^t = 1.6$. Chern numbers of the bands from the top are $C_n = (0, 1, -1, 0)$.

2.8, $\phi^t = 1.6$. In ascending order of energy, the Chern numbers are given by $C_n = (0, -2, 2, 0)$. Hence, the system is in the CI phase for this particular set of values. Another CI phase with $C_n = (0, 2, -2, 0)$ is obtained by reversing the signs of ϕ^b and ϕ^t, simultaneously. It is interesting to note that, higher Chern number is obtained by coupling two identical layers of depleted Lieb lattice. If we vary the parameters, the middle two bands overlap and the Chern number becomes undefined. In addition, one pair of CSM phases with $C_n = (0, \mp 1, \pm 1, 0)$ have been identified when $t_2/t_1 = 0.5$, $t_3/t_1 = 0.25$, $t_4/t_1 = 1.8$, $\mu/t_1 = 1.4$, $\phi^b = \pm 2.8$, $\phi^t = \pm 1.6$. So unlike the monolayer system, both CI and CSM phases are found in the bilayer system.

In order to check the BBC rule, two isolated edges are created by means of bilayer depleted Lieb lattice ribbon for the system. The effective Hamiltonian is obtained by removing the PBC along y direction. In order to get the edge states, system of $N = 200$ sites along y direction is considered and the resulting Hamiltonian is diagonalized where energies are obtained as a function of good quantum number k_x. In Fig. 5.6(b), the energy eigen-values are plotted for

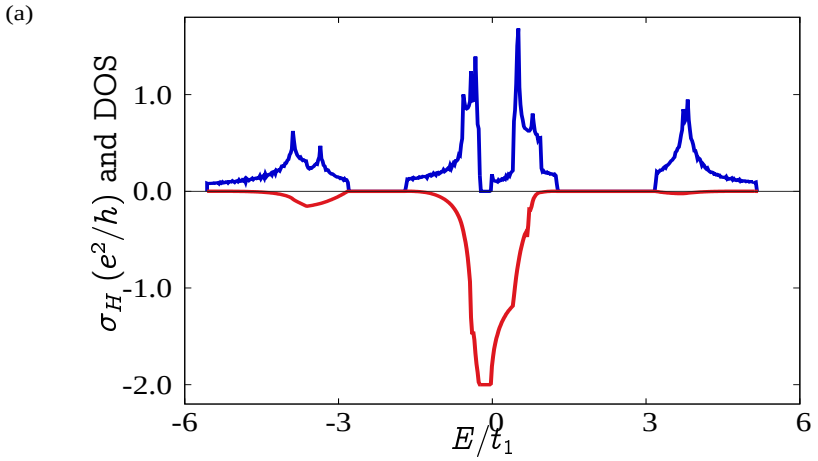

Figure 5.8: The Hall conductance σ_H (red line) and DOS (blue line) with respect to the Fermi energy, E for bilayer depleted Lieb lattice when $t_2/t_1 = 0.2$, $t_3/t_1 = 0.5$, $t_4/t_1 = 1.8$, $\mu/t_1 = 1.4$, $\phi^t = 2.8$, $\phi^b = 1.6$. σ_H shows three plateaus where DOS vanish.

the particular set of values. In this occasion, two pairs of in-gap edge modes are found to exist since the middle two bands carry the Chern numbers, either $C_n = \pm 2$, or $C_n = \mp 2$, depending on the sign of ϕ's. The chiral and localized nature of edge states are also verified from the plot. The side-panel shows the DOS of the ribbon which reveals the existence of true band gap. Variations of $\sigma_H(E)$ and DOS for the bilayer depleted Lieb lattice with respect to Fermi energy, E are shown in Fig. 5.8, when $t_2/t_1 = 0.2$, $t_3/t_1 = 0.5$, $t_4/t_1 = 1.8$, $\mu/t_1 = 1.4$, $\phi^t = 2.8$, $\phi^b = 1.6$. Hall conductivity shows three plateaus where DOS vanishes. Two plateaus are found when $\sigma_H(E) = 0$, and one at $\sigma_H(E) = -2$. In contrast no plateau is found for the monolayer system, since true band gap is absent there. The width of the plateau depends on the width of the band gap. As shown in Fig. 5.8, the height of the plateau is $\sigma_H = n(e^2/h)$, with $n = -2$ since the Chern number distribution is $C_n = (-2, 2)$.

5.6 Summary and Discussions

Search of topological phases in various materials became an intriguing part of investigation in condensed matter physics. Theoretical discovery of QAHE leads to an enormous possibility of finding new topological phases in a variety of systems in the absence of true magnetic field [19]. Investigations in this field began by formulating theoretical models on specific lattice structures. In the 2D systems, nontrivial topological phases are found to exist on the models formulated on non-Bravais lattices. Symmetries of studied models reveal that those non-Bravais lattices can be derived from either square or triangular lattices. For examples, Lieb [6], CaVO [20, 21, 22], square-octagon [23, 24] and checkerboard [15] lattices are derived from square lattice, while honeycomb [19], stuffed-honeycomb [25], kagome [24, 26], breathing kagome [27], star [28, 29], α-$\mathcal{T}_3$ [30] and dice [31] are derived from triangular lattice. Investigation in this field continues thereafter by means of finding topological phase on remaining non-Bravais lattices.

Previous study on the monolayer depleted Lieb lattice predicted no topological phase while formulating FM XXZ Heisenberg model with NN, NNN and NNNN exchange interactions even in the presence of DM term and external magnetic field [12]. In contrast, this study lets out the existence of nontrivial topological phases in monolayer and bilayer structures of depleted Lieb lattice. This 2D non-Bravais lattice is generated out of square lattice by removing its sites systematically in such a way that four-fold rotational symmetry of original square lattice reduces to two-fold. The resulting monolayer lattice is bipartite while the bilayer lattice is quadripartite.

In the nontrivial regime, each of the models hosts two topological phases. In each case, tight-binding models are formulated incorporating NN, NNN and NNNN hopping terms where NNNN terms are complex. The phases of the com-

plex terms is chosen in such a way that net magnetic field per square plaquette vanishes. Although, model with this characteristic feature does hold topologically nontrivial phase, additional staggered onsite energy term is taken into account in order to note another transition from nontrivial to trivial phase. System undergoes two types of phase transitions, namely, between two nontrivial phases and nontrivial to trivial phases. Topological phases found in monolayer model are characterized by $C_n = (\pm 1, \mp 1)$, while those for bilayer model are defined by $C_n = (0, \pm 2, \mp 2, 0)$, and $C_n = (0, \mp 1, \pm 1, 0)$. CSM phase appears in monolayer model while both CI and CSM phases emerge in bilayer case as they are noted before. Also, as stated before, tight-binding model on depleted Lieb lattice identical to the original Haldane model could not lead to nontriviality. It is now established that any artificial 2D lattices can be realized by means of photonic and cold-atom crystals or by synthesizing the surface state electrons on Cu(111)/CO substrate [10]. Existence of edge states may be verified in this route. Detection of topological phase is also possible by observing the feature of $\sigma_H(E)$, if real materials are found in future. At the same time, search of new topological phases in the remaining non-Bravais lattices will be carried on.

Bibliography

[1] Owerre S. A., Phys. Rev. B. **94** 094405 (2017).

[2] Sorn S., Phys. Rev. B. **98**, 125145 (2018).

[3] Nita M., Ostahie B., and Aldea A., Phys. Rev. B. **82**, 125428 (2013).

[4] Beugeling W., Everts J. C. and Smith C. M., Phys. Rev. B **86**, 195129 (2012).

[5] Karnaukhov I. N. and Sleptsov I. O., (arXiv:1510.07239v1) (2015).

[6] Weeks C. and Franz M., Phys. Rev. B. **82**, 085310 (2010).

[7] Long Y. and Ren J., (arXiv:1706.01107) (2017).

[8] Cao X., Chen K. and He D., J. Phys.: Condens. Matter **27**, 166003 (2015).

[9] Banerjee S. and Saxena A., Phys. Rev. B **103**, 235125 (2021).

[10] Slot M., Gardenier T. S., Jacobse P. H., van Miert G. C. P., Kempkes S. N., Zevenhuizen S. J. M., Smith C. M., Vanmaekelbergh D. and Swart I., Nature Phys **13**, 672-676 (2017).

[11] Cui B., Zheng X., Wang J., Liu D., Xie S. and Huang B., Nat. Commun. **11**, 66 (2020).

[12] de Oliveira P. G. and Pires A. S. T., Physica B **654**, 414721(2023).

[13] Kambe S. and Ishii O., Physica C **341-348**, 555-556 (2000) .

[14] Ryu S., Schnyder A. P., Furusaki A., and Ludwig A. W. W., New J. Phys. **12**, 065010 (2010).

[15] Sun K., Gu Z., Katsura H. and Das Sarma S., Phys. Rev. Lett. **106**, 236803 (2011).

[16] Fukui T., Hatsugai Y. and Suzuki H., J. Phys. Soc. Jpn. **74**, 1674 (2005).

[17] Sticlet D., Piéchon F., Fuchs J. -N., Kalugin P. and Simon P., Phys. Rev. B. **85**, 165456 (2012).

[18] Mook A., Henk J. and Mertig I., Phys. Rev. B. **90**, 024412 (2014).

[19] Haldane F. D. M., Phys. Rev. Lett. **61**, 2015 (1988).

[20] Bose I. and Ghosh A., Phys. Rev. B **56**, 3149 (1997).

[21] Deb M. and Ghosh A. K., J. Magn. Magn. Mater. **533**, 167968 (2021)

[22] Deb M. and Ghosh A. K., Eur. Phys. J. B. **93**, 145 (2020).

[23] Kargarian M. and Fiete G. A., Phys. Rev. B. **82**, 085106 (2010).

[24] Liu X. P., Chen W. C., Wang Y. F. and Gong C. D., J. Phys.:Condens. Matter **25**, 305602 (2013).

[25] Sil A. and Ghosh A. K., J. Phys.: Condens. Matter **32**, 025601 (2019).

[26] Guo H. M. and Franz M., Phys. Rev. B **80**, 113102 (2009).

[27] Sil A. and Ghosh A. K., J. Phys.: Condens. Matter **32**, 205601 (2020).

[28] Chen W. C., Liu R., Wang Y. F. and Gong C. D., Phys. Rev. B. **86**, 085311 (2012).

[29] Chen M. and Wan S., J. Phys.: Condens. Matter **24**, 325502 (2012).

[30] Dey B. and Ghosh T. K., Phys. Rev. B **99** 205429 (2019).

[31] Mondal S. and Basu S., Phys. Rev. B **107** 035421 (2023).

Chapter 6

Conclusion

6.1 Cumulative Summary

Topological insulator brings the fundamental mathematical concept of topology in the realm of condensed matter physics and opens up a new avenue of theoretical research, ably supported by experimental manifestations and material realizations. The application of these materials in spintronics and quantum computation makes it even more attractive in the scientific community. In the vast dynamic field of TIs, this dissertation makes a small effort to find out novel topological phases within a few well-known and a few lesser-known systems.

In this dissertation, topological properties of six different systems have been described and evaluated. Simple Haldane-like model has been proposed on non-interacting fermionic systems formulated on the three-band stuffed honeycomb lattice and two-band depleted Lieb lattice as described in chapters 2 and 5, respectively. It has been concluded that addition or deletion of one or more sublattices from a simple lattice system can generate non-trivilaity in the presence of complex phase-coupled hoppings in tight-binding regime. Thoughtful interplay among the onsite energies, complex phases and hopping parameters

can generate interesting topological phase transitions. In chapter 3, a simple tight-binding model on a non-interacting fermionic system of square-octagon lattice has been considered, which has quadratic band-touching points. In this system, the emergence of multiple topological phase transitions and generation of phases with higher Chern numbers have been shown to be induced by periodic irradiation. Hence, application of light-wave has also been proved to be an useful tool in generation of nontrivial topological phases in an otherwise trivial gapless or gapped system. Furthermore, in chapter 4, a ferromagnetic Heisenberg Hamiltonian is considered on a non-interacting bosonic system formulated on a well-known breathing kagome lattice. Existence of first order and second order exotic topological phases has been identified and substantiated, respectively in the absence and presence of DMI. Moreover, anomalous BBC has also been reported in this study.

In the second chapter, stuffed honeycomb lattice has been investigated on being a possible host of nontrivial topological phase. This lattice interpolates between well-known honeycomb, triangular and dice lattices and preserves hexagonal symmetry. The spin-liquid properties of $LiZn_2Mo_3O_8$ can be well-described in terms of Heisenberg model formulated on this lattice. Since both the honeycomb and dice lattices, being non-Bravais, have been reported to host CI phases, our focus turned onto the stuffed honeycomb lattice in search of similar CI phases. Now, the prerequisite for obtaining such phase is to break the symmetries, namely TRS and PHS. Naturally, complex phase coupled with NNN hopping and asymmetric onsite energy are introduced in the tight-binding model. The resulting Hamiltonian breaks all the symmetries as well as produces the desired CI and CSM phases with non-zero Chern numbers characterizing the bands. The reduced dimensional system produces edge states on the boundaries according to BBC rule. The IQHE plateaus obtained from theoretical calcula-

tion can be verified experimentally for this model also. To prove that derived lattice systems can indeed be a possible host of novel CI phases, a stuffed square lattice is also considered. This three-band system results from incorporation of a single-orbital square lattice in a two-orbital square lattice. Spin-orbit coupling is introduced with NNN hopping so that the resulting Hamiltonian becomes time reversal invariant as a whole, but the up-spin and down-spin sector breaks TRS separately. Henceforth, each individual sector is shown to produce exotic CI phases with high Chern numbers, which is cross-verified with the number of in-gap edge modes between the bulk bands. The characterization of this system by another topological invariant spin Chern number has also been discussed.

In chapter three, attention is drawn towards the square-octagon lattice, which is the amalgamation of four inter-penetrating square sublattices. This lattice consisting of square and octagonal plaquettes forms one of the eleven possible Archimedean tessellations of the two-dimensional plane. The spin-1/2 V^{4+} ions of the antiferromagnetic spin-liquid CaV_4O_9 arrange themselves in square-octagon structure. This lattice model had already been reported to produce Dirac Cones at Γ and M points of the Brillouin zone in the absence of NNN hopping. It also produces topological phases and phase transitions in presence of SOC and complex phase. Hence, this system is investigated for topological phases in presence of polarized periodic irradiations also. In the absence of any external agent, the system exhibits trivial topology and the band structure consists of quadratic band touching points and a pair of flat bands. When the effect of circularly polarized light is taken into consideration in the effective Hamiltonian using Floquet-Bloch theory, the energy spectrum exhibits band gap. Simultaneously, the system becomes nontrivial as confirmed by the bands acquiring non-zero Chern numbers as well as the IQHE plateaus and in-gap edge modes in the open geometry. One of the main characteristics of this system is

that multiple TPTs occur when the amplitude of incident light and the hopping strengths are varied. No such transitions are observed with the variation of frequency of incident light. Of course, the frequency is to be kept at off-resonant regime so that the floquet-magnus expansion remains valid. Overall, the square-octagon lattice coupled with circularly polarized light offers intriguing topological phase with high Chern numbers and phase transitions and paves another way of inducing nontriviality in this particular lattice system.

In the following chapter, focus is shifted onto the breathing kagome lattice, which is distinguished from the kagome lattice in the sense that the Heisenberg interaction strength between the three sublattices is different in upward and downward triangles. This preserves the flat band but gaps out the Dirac cone since the inversion symmetry is broken. As the flat band touches the middle band in four corners of the Brillouin zone, conventional first order topological phase is not possible in this system since Chern numbers are undefined. But the pattern of the 1D edge modes in the gap between the other two bands shows typical signature of second order topological phase. The same result has been obtained by finding the energy spectrum in zero dimension. Considering a finite triangular replica of the system, three states at the three corners of the triangular shaped finite lattice have been found, correlating with the edge mode pattern. To characterize this novel topological phase, set of polarization vectors is defined and they successfully characterize the topological nontriviality of the system.

Moreover, DMI is added along NN bonds to open up the gap between flat band and middle band to check the possibility of first order topological phase also. This results in three different TMI phases in the relevant parameter space. Interestingly, in one of the region, both first order and second order TMI phases superpose as confirmed by calculating the respective topological invariants and edge/corner geometry. More interestingly, the behaviour of polarization vectors

and existence of corner states does not always correlate. This anomaly of BBC in second order TIs has been reported before and found in this system also. Finally, thermal hall conductivity is calculated for ease of experimental verification of TMI phases.

In the penultimate chapter, another derived lattice in the form of depleted Lieb lattice has been studied in order to find CI phases. This lattice is generated by depleting one of the sites of well-known Lieb lattice. In tight-binding formulation, three-band energy spectrum of Lieb lattice shows one flat band and two Dirac cones. The two-band spectrum of depleted Lieb lattice shows one Dirac cone but does not retain the flat band. Hence, to break the required symmetries, complex phase coupled with NNNN hopping and staggered onsite energy are incorporated in the Hamiltonian. Existence of topological phase is confirmed by the analytical and numerical calculation of Chern numbers, edge geometry and IQHE plateau. Additionally, bilayer version of this model was explored to find new topological phase in the extended parameter space. This four-band system was successfully able to produce CI phase with higher Chern numbers.

6.2 Scope for Future Work

In this journey of finding novel topological systems within known lattice systems, there are numerous scopes for extension of these works and further exploration.

1. New derived lattice systems can be created from known lattice systems by addition or deletion of sublattices. Also, multilayer or twisted bilayer of various known lattice systems can be investigated as a possible host for first and second order CI phase, Floquet CI phase and TMI phase.

2. Electron-electron interaction can be incorporated in those systems and may be investigated for possibility of fractional Chern insulators or topological

flat bands.

3. Spin-orbit coupling may be introduced in those systems in order to find the TRS invariant TI phases.